

A framework of Image Processing for Image-guided  
Procedures

by

**Anwar Abdalbari**

A Thesis Submitted in Partial Fulfillment  
of the Requirements for the Degree of

Doctor of Philosophy

in

Electrical and Computer Engineering

The Faculty of Engineering and Applied Science

University of Ontario Institute of Technology

July 2016

Copyright ©Anwar Abdalbari, 2016

# Acknowledgements

I would like to take this opportunity to express my sincere appreciation to everyone who generously supported me to achieve this success.

First and foremost, I thank God for giving me strength in my research. Secondly, I would like to express my thankful and appreciation to my thesis supervisor Dr. Jing Ren. It has been an honor to be her first Ph.D. student; I found her creativity and enthusiasm incredibly motivating to me during my study. I am also thankful for her time, ideas and funding to obtain my Ph.D.

I would like to express my sincerely thanks Dr. Edward Huang. I had the pleasure of working with him during my first 18 months in the program. The discussions with him have not only contributed significantly to this work but also have made lasting impacts on me.

I gratefully appreciate my exam committee members for their time of reading my thesis and their valuable comments.

And the final words in the end of this work belong to my family, I would like to express my thanks to my family for all their love and encouragement.

Anwar

# Contents

<b>Abstract</b>	<b>xii</b>
<b>1 Introduction</b>	<b>1</b>
1.1 The Research Problem . . . . .	2
1.2 Research Challenges . . . . .	2
<b>2 Background</b>	<b>6</b>
2.1 Magnetic Resonance Imaging . . . . .	6
2.2 Image Segmentation . . . . .	7
2.3 Image Registration . . . . .	9
2.4 Stereo Endoscopic . . . . .	10
2.5 Literature Review . . . . .	11
2.6 Thesis Outline . . . . .	16
<b>3 Segmentation of the Liver From Abdominal MR Images</b>	<b>19</b>
3.1 Introduction . . . . .	22
3.2 Level Set Approach . . . . .	23
3.3 The Proposed Speed Function . . . . .	25
3.4 Materials and Methods . . . . .	27
3.5 Filling the Surface Holes . . . . .	29
3.6 Data and Validation . . . . .	31
3.6.1 Segmentation Accuracy Measures . . . . .	33
3.7 Summary . . . . .	34

<b>4 Seeds Classification for Image Segmentation</b>	<b>35</b>
4.1 Introduction . . . . .	36
4.2 Material and Methods . . . . .	41
4.2.1 Moments Invariant . . . . .	41
4.2.2 Affine Transformation . . . . .	47
4.3 The Used Neural Network Architecture . . . . .	50
4.4 Level Set Segmentation . . . . .	53
4.5 Results . . . . .	54
4.6 Summary . . . . .	57
<b>5 Vessel-Based Fast Deformable Registration with Minimal Strain</b>	
<b>Energy</b>	<b>60</b>
5.1 Introduction . . . . .	61
5.2 Materials and Methods . . . . .	64
5.2.1 Physics-Based Registration Methodology . . . . .	64
5.2.2 Curve Energy . . . . .	67
5.2.3 Strain Energy . . . . .	69
5.2.4 Evaluation Methods . . . . .	71
5.3 Registration Accuracy Measures: TRE/ACD . . . . .	71
5.3.1 Landmark-Based Target Registration Errors (TRE) . . . . .	71
5.3.2 Average Vessel Centerline Distance (ACD) . . . . .	72
5.4 Image Processing for Evaluating Registration Accuracy . . . . .	73
5.4.1 Image Preprocessing . . . . .	73
5.4.2 Centerline Extraction . . . . .	73
5.4.3 Localization of Branch Points . . . . .	73
5.5 Results . . . . .	73
5.5.1 Quantitative Registration Accuracy . . . . .	75
5.5.2 Comparison with EBS . . . . .	76
5.6 Summary . . . . .	78

<b>6 Deformable Image Registration for Tissues with Large Displacement</b>	<b>81</b>
6.1 Introduction . . . . .	82
6.2 Analysis of Deformation Field of the Liver . . . . .	85
6.3 Observations and Analysis . . . . .	89
6.4 Deformable Image Registration For Large Rotation . . . . .	92
6.5 Region-based Neuro-fuzzy Transformation Model . . . . .	93
6.5.1 Computation of Local Rigid Transformation . . . . .	97
6.6 Analytical solution to registration energy function . . . . .	101
6.7 Registration Accuracy Measures . . . . .	104
6.7.1 Landmark-based Target Registration Errors (TRE) . . . . .	104
6.7.2 Average Vessel Centerline Distance (ACD) . . . . .	104
6.7.3 Average Vessel Centerline Distance of Independent Points (ACDIP) . . . . .	104
6.8 Experimental Results . . . . .	105
6.8.1 Visual Inspection: Overlay of Images/Vessels . . . . .	106
6.9 Registration Accuracy: TRE and ACD . . . . .	106
6.10 Comparison With the Conventional NFS Method Without Using Large Rotation Formulation . . . . .	107
6.11 Summary . . . . .	109
 <b>7 Automatic Surface Reconstruction for Endoscopy-MR Image Fusion</b>	 <b>110</b>
7.1 Experimental Setup and Camera Calibration . . . . .	111
7.2 Surface Reconstruction From Stereo Endoscopic Images . . . . .	112
7.2.1 Conversion of Input Images to Grayscale Images . . . . .	113
7.2.2 Intensity Correction . . . . .	114
7.2.3 Detection of Region of Interest . . . . .	117
7.2.4 Image Dilation and Erosion . . . . .	118
7.2.5 Thinning and Intersection Detection . . . . .	118

7.2.6	Matching Grid Points . . . . .	120
7.2.7	Surface Reconstruction . . . . .	122
7.3	Surface Based Registration . . . . .	125
7.3.1	ICP Registration . . . . .	125
7.3.2	Registration Accuracy . . . . .	126
7.4	Summary . . . . .	127
<b>8</b>	<b>Conclusion and Future Work</b>	<b>129</b>
8.1	Future Research . . . . .	134
	<b>Appendices</b>	<b>136</b>

# List of Figures

1.1	Flowchart of the proposed framework . . . . .	5
2.1	The effect of applied magnetic field on nuclear spins . . . . .	7
2.2	Axial, sagittal and coronal planes . . . . .	8
2.3	Stereo endoscope . . . . .	11
3.1	Challenges of liver segmentation . . . . .	21
3.2	The surrounding structures of the liver . . . . .	21
3.3	The contour of the level set function . . . . .	25
3.4	The proposed method flowchart . . . . .	26
3.5	The input level set image . . . . .	28
3.6	The input image of the segmentation process . . . . .	28
3.7	Smoothed image . . . . .	28
3.8	Gradient magnitude image of the smoothed image . . . . .	28
3.9	Sigmoid output of the gradient magnitude image . . . . .	28
3.10	The surface patch image proposed . . . . .	29
3.11	Least square fitting line . . . . .	30
3.12	Filling the liver surface holes . . . . .	32
3.13	The segmentation result before applying the proposed method . . . . .	32
3.14	The segmentation result after applying the proposed method . . . . .	33
4.1	MR images with different positions from the same subject . . . . .	38
4.2	A binary Image of MR image . . . . .	41
4.3	Applying a padding filter to MR image . . . . .	42
4.4	Schematic diagram for the proposed classification method . . . . .	43

4.5	The neighbourhood pixels of a seed point . . . . .	47
4.6	The used ANN model . . . . .	50
4.8	Seed points at different regions of the liver . . . . .	57
4.7	The proposed classification system pipeline . . . . .	58
5.1	Schematic of analytically computing curve energy and its derivative	66
5.2	Extracted vessel centerlines within the liver . . . . .	74
5.3	Overlay of images before and after registration . . . . .	77
5.4	Overlay of vessel centerlines before and after registration . . . . .	79
6.1	Schematic of deformable images . . . . .	87
6.2	The decomposition of a deformed ellipsoid object . . . . .	89
6.3	The deformation patterns within selected regions of the liver . . . . .	91
6.4	Displacement decomposition . . . . .	91
6.5	Schematic of the proposed registration method flowchart . . . . .	95
6.6	The configuration of local regions . . . . .	98
6.7	Generalized Gaussian function . . . . .	100
6.8	Centerlines before match . . . . .	106
6.9	Overlay of centerlines after match . . . . .	107
6.10	Overlay of images before and after registration . . . . .	108
7.1	Experimental setup for stereo endoscope . . . . .	112
7.2	Flowchart for automatic surface reconstruction procedure . . . . .	113
7.3	Input images of the stereo-endoscope . . . . .	114
7.4	Grayscale and negative images of the stereo-endoscope . . . . .	114
7.5	A center pixel within a neighbourhood . . . . .	115
7.6	Intensity correction image . . . . .	116
7.7	The effect of intensity correction on binary images . . . . .	116
7.8	Region of interest image . . . . .	117
7.9	Dilated image . . . . .	118
7.10	The effect of thinning technique on images . . . . .	120
7.11	The correspondence points between the left and right images . . . . .	121

7.12	Epipolar constraints . . . . .	121
7.13	Reconstructed surface results with intensity correction . . . . .	124
7.14	Reconstructed surface results without intensity correction . . . . .	124
7.15	The overlap of the surface and the phantom . . . . .	125
7.16	Surface registration accuracy using intensity correction . . . . .	126
7.17	Surface registration accuracy without using intensity correction . . . . .	127
7.18	Image fusion of patient models and reconstructed surface . . . . .	128
7.19	Image fusion of patient models and reconstructed surface/close-up view . . . . .	128

# List of Tables

4.1	Mean and standard deviation of the generated moments . . . . .	55
4.2	Overall accuracy of the synthesized images . . . . .	55
4.3	Overall accuracy of the unseen images . . . . .	55
4.4	The moment invariants ratio, mean, standard deviation of unseen images . . . . .	57
5.5	Registration accuracy of liver images . . . . .	75
5.6	Registration accuracy with EBS . . . . .	78
6.7	Deformation patterns of 10 different regions . . . . .	90
6.8	Comparison of registration accuracy . . . . .	108
7.9	The sensitivity of the points detection algorithm with intensity correction . . . . .	122
7.10	The sensitivity of the points detection algorithm without inten- sity correction . . . . .	123
7.11	Average surface distance error (ASD) achieved . . . . .	124

# Glossary

$\phi$  Level set function 24

$E_c$  The distance between pairs of 3D vessel centerlines 10

$E_e$  Stain Energy 10

$E_m$  The distance between correspondin bifurcation points 10

$T(x, p)$  Deformable transformation model 64

$p$  The transformation parameters 64

**2D** two dimensional 1

**3D** three dimensional 1, 3, 18

**ANN** Artificial Neural Network 12

**CCN** Cross-point Number 118

**CDE** Centerline Distance Error 60, 132

**CT** Computed Tomography 1

**EBS** Elastic Body Spline 73

**ICP** Iterative Closest Point 124

**MCN** Modified Cross-point Number (MCN) 118

**MR** Magnetic Resonance 3, 16

**MRI** Magnetic Resonance Image 1, 6, 16

**NFS** Neuro-fuzzy Strain 75

**ROI** region of interest 116

**RVD** Relative Volume Difference 34

**SCN** Simple Cross-point Number 118

**TPS** Thin-plate Spline 62

**TRE** Target Registration Error 60, 132

**VOE** Volumetric Overlap Error 34, 131

# Abstract

Contrary to the cases of open surgery, during minimally invasive procedures, surgeons have no direct access or very limited access to the operative site and can only visualize the site and the focal region with the aid of imaging tools. During patient follow-up and the surgical planning stage, multiple complementary images and patient-specific models need to be aligned with each other for better interpretability. Image segmentation and deformable image registration are often needed for this step since the tissues normally deform in different images. Traditionally, image segmentation and registration are separate research topics. However, they are closed related. Segmentation accuracy affects feature-based registration accuracy and a good registration is able to improve the speed and accuracy of image segmentation.

In this thesis, we present a coherent and consistent framework for image processing. The process of the proposed approach consists of two main modules. In the first module, we performed preprocessing tasks on raw MR images to extract the blood vessels centerlines from these images. Next, bifurcation points were calculated as the intersections of the extracted centerlines. Vessel structures and bifurcation points provide input information for further operations such as image segmentation and image registration. Then, we propose an innovative approach to automating the initialization process of the liver segmentation of magnetic resonance images. The seed points, which are needed to initialize the segmentation process, are extracted and classified by using affine invariant moments and artificial neural network. To complete this stage, we proposed robust and fast approaches for MR image registration for deformable tissues. The proposed registration methods work with soft homogenous tissue with small and large rotation shift.

In the second module, we performed surface to surface registration of MR

and endoscopic images, which will provide the surgeon with better 3D context of the surgical site in minimally invasive procedures. In this step, we project a gridline light pattern onto the surgical site and then use a stereo endoscope to acquire two stereo images. The major steps in the surface reconstruction process include 1) applying an automatic method of detecting region of interest, 2) applying an image intensity correction algorithm, and 3) applying a novel automatic method to match the intersection points of the gridline pattern.

We have validated our proposed framework technique by comparing the methods with existing techniques of similar scope. Our experiment results show that our methods outperform the existing methods regarding correctness and efficiency.

# Chapter 1

## Introduction

Currently, the advanced technology of digital imaging systems provides high-quality images that are used in varying types of applications starting from newspaper industry and surveillance scenes to medical procedures. Digital images represented as raw data sets that can be converted to relevant information by applying objective, quantitative, and qualitative analysis techniques to these images.

Biomedical image processing is a form of biomedical signal processing for which the input is a medical image acquired from different imaging modalities, i.e. Magnetic Resonance Image (MRI), Computed Tomography (CT) Scan, X-Ray and Nuclear Medicine [75]. Biomedical image processing techniques involve manipulating the biomedical image as a two dimensional (2D) signal or three dimensional (3D) signal and applying standard signal-processing techniques to it. In this thesis we will concentrate on both 2D and 3D image processing techniques such as image enhancement, image filtering, image registration, corresponding points matching, image segmentation, thresholding and morphological operation.

As far as biomedical image processing is concerned, scholars and scientists from different disciplines have been attracted to that area. They believe in the importance of the biomedical image processing role by providing and developing computer-aided tools for treatment guidance, diagnosis, and clinical research. Therefore, many of new development imaging modalities are developed. As a

result, researchers should develop new methods and new techniques to deal with the output of that new technology and various imaging scanners. For example, how to process MR images resulting in valuable information acquisition for treatment diagnosis. In consequence, new algorithms, new image modalities, and new applications in this field have been developed.

## 1.1 The Research Problem

Nowadays, there are lots of image processing techniques, among of these techniques are image segmentation, deformable registration, and surface to surface registration of MR and endoscopic images. These techniques are fundamental in many clinical applications. Soft organs such as the liver can undergo large organ shift and tissue deformation in many medical procedures due to patient repositioning, respiration, surgical manipulation, or other physiological reasons, e.g. differences in bowel and stomach filling and weight loss, etc.[21][33]

Accurate deformable image registration, segmentation, and surface to surface registration are needed in most of the clinical procedures. Despite the fact that much work has been done in the field of deformable image registration and segmentation, it is still very challenging to achieve accurate results efficiently due to large organ shift and tissue deformation. Also, accurate reconstruction of a 3D surface from stereo endoscopic images is still a challenging process especially for the surgical site with few landmarks. These techniques should be fast, accurate, physically consistent, and robust.

## 1.2 Research Challenges

In this thesis, we developed a framework to register, segment, and register a reconstructed surface of endoscopic images to a surface generated from MR images of the liver organ. Even though different methods have been published,

and significant work has been dedicated in the literature to the improvement of such algorithms, there are still challenging research area to develop a framework to combine these methods in one framework with more accurate and promising results. Therefore, there are many important issues that make framework of image-guided procedure a very challenging problem to solve.

- **Liver segmentation:** The need of correct liver information, shape, and volume is crucial in any treatment or diagnose procedure. The difficulties of the segmentation process are due to the location of the liver. Furthermore, liver is surrounded with organs such as the heart, stomach, and kidneys. These organs have the similar intensity as the liver; as a result, there is an overlap of intensity of the liver and these organs adding more challenges to the segmentation process [1].
- **Seed points detection using invariant moments:** Interest point descriptor for matching points in 3D images is very challenge task. The problem is due to the location of the points of concern since the detector should be able to locate the seed within multiple MR images from the same patient regardless the positioning and raspatory cycle of the patient during the scan acquiring. In this research, we will generate moments descriptor invariant to affine transformation for points in 3D liver Magnetic Resonance (MR) images. These points will be used as seed points to initialize the segmentation method we presented in this thesis.
- **Deformable registration:** Deformable image registration of the liver is considered hard task due to large organ shift and tissue deformation caused by patient respiration and re-positioning. In deformable registration, we try to align two images together to reduce the chance of getting trapped in overfitting issue.
- **Surface to surface registration of MR and endoscopic image:** Images being acquired using different modalities (i.e., MR and endoscopic

video) are captured using different imaging devices at different times. Therefore, these images often contain various geometric distortions that make it difficult to compare image content.

**The images used in this thesis are acquired at the Children for SickKids Hospital**

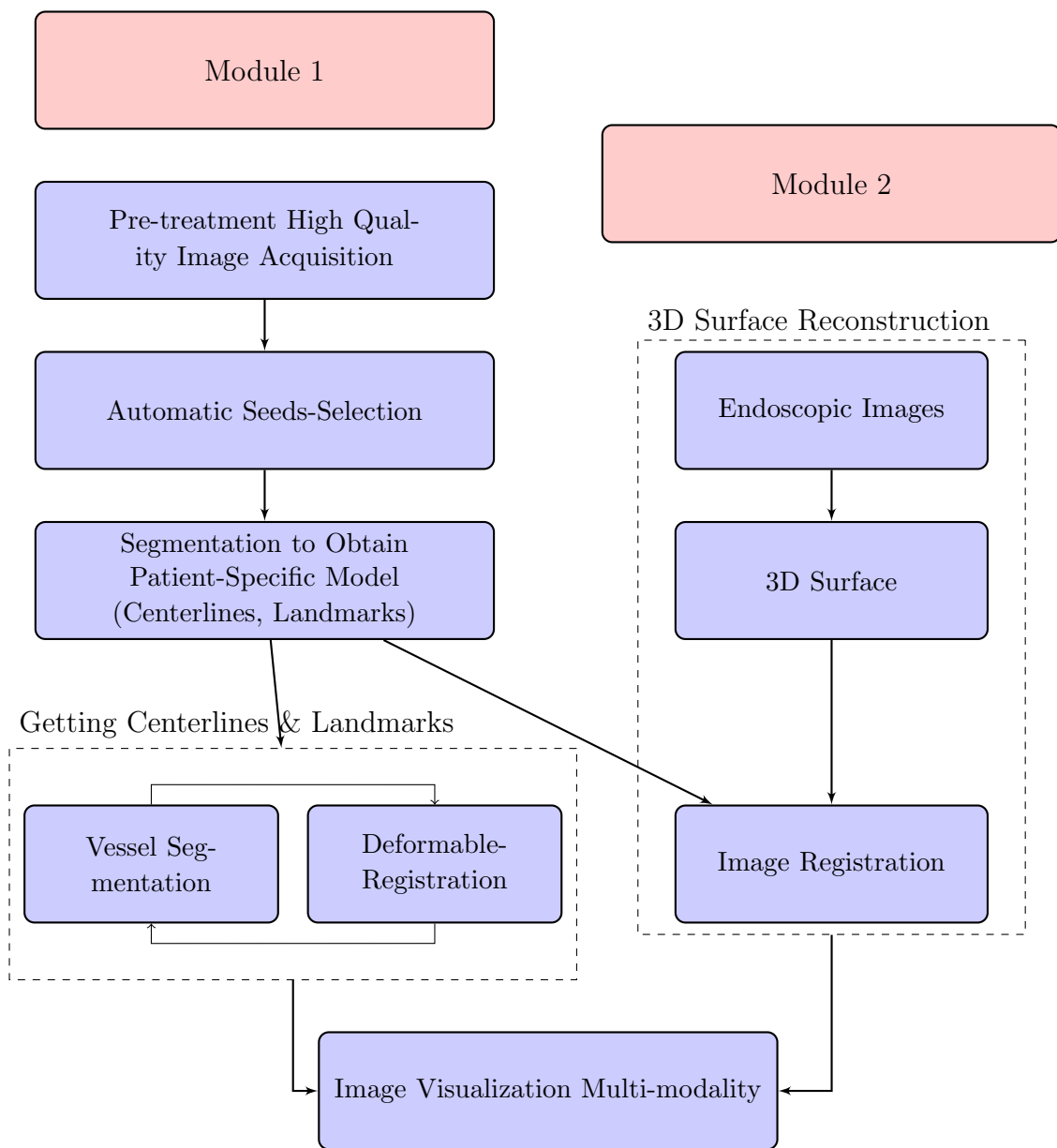


Figure 1.1: Flowchart of the proposed framework

# Chapter 2

## Background and Related Work

### 2.1 Magnetic Resonance Imaging

Magnetic Resonance Imaging (MRI) is one of the safest, most accurate, and painless procedures to acquire medical images. These images have an impact on medical treatment guidance, diagnosis, and clinical research. Magnetic Resonance Imaging was invented in 1977. MRI scanners consist of four essential modules to form images of the human body; these modules are the magnets, the antenna, a computer, and the software [32]. The first part is the magnets. The magnets arrange in such a way as to affect the direction of points if these points were inside the MRI machine. The human body consists of 70 percent water, and each water molecule has two hydrogen atoms. In other words, the hydrogen atom molecule (proton) is acting as a micro magnet. In fact, the human body is full of protons in every organ and tissue but with a different concentration and in a different structure. Since the human body is full of random micro magnets (proton), these magnets can line up in one direction if the body is affected by a strong external magnetic field.

The movement of the protons cannot be felt, and there is no effect of that movement to the patient. As a result of protons spinning, a slight amount of energy releases in the form of a radio wave. The manipulation of the magnets can manipulate the protons in a different direction. The antenna, which is the second part of the MRI scanner, is designed to detect different amounts of radio

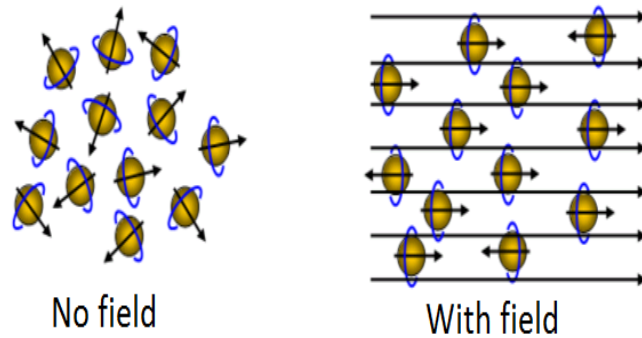


Figure 2.1: The effect of applied magnetic field on nuclear spins: Image downloaded from Google Images

signals released when the protons spin. The third major part of MRI machine is a very fast and powerful computer able to collect all the data which is picked up by the antenna and store this raw data in its storage devices. Lastly, the major component of the MRI machine is a computer software uses to create images based on the data generated by the radio signal. The software takes all the data collected by the antenna and forms the data in such a way to create images of the human body. The flat images created are formed in order by slices. The slices form in any of the three directions Axial, Sagittal, and Coronal [67], (see Figure 2.2).

## 2.2 Image Segmentation

Image segmentation is one of the fundamental processes in medical image processing. Many radiological evaluation and diagnosis medical applications are based on image segmentation. The aim of any segmentation process is to classify an image into different distinct clusters or regions, such as heart, brain, liver, lungs, scalp. The classification process is based on grouping together image pixels which have the same characteristics. Extracting the image objects from the image background is one of these classifications. Segmentation could be performed by edge based, pixel based, or region based methods. In edge based method, edge knowledge and information are used to recognize the

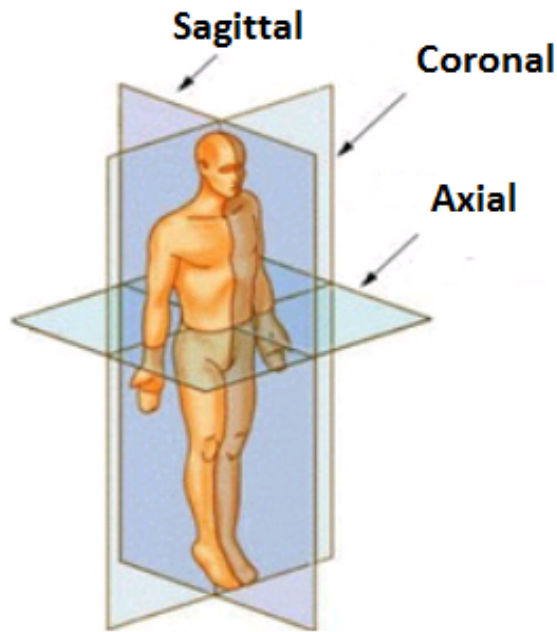


Figure 2.2: Axial, Sagittal, and Coronal planes

boundaries of the image objects [3] [15]. In some cases, the boundaries are analyzed and modified to get full closing regions of the object. While in pixel based methods, segmentation can be implemented by using image histogram to determine a typical grey level for each object. In the region based method, the segmentation process should detect homogeneous regions in such a way that regions should satisfy certain homogenous criterion. In general, segmentation in MR images is one of the hardest problems in image analysis, as it is extremely hard to get a perfect segmentation method for every image. The difficulties are due to over-segmentation and segmentation leakage. In over-segmentation, the boundaries of the liver and the surrounding organs have similar intensity distribution. Hence, it is hard for a segmentation process to distinguish between these boundaries. However, due to inhomogeneous intensity distributions at the liver boundary in the contrast enhanced images. Noisy regions could cause leakage to the background tissues. The successful segmentation process in most cases use different strategies and combination of the mentioned segmentation methods to get useful information from the image. Many algorithms and methods that are present in the literature focus on the liver image segmentation. These methods

attempt to get the best they can by applying various techniques to estimate the shape of the liver.

## 2.3 Image Registration

The revolution in medical imaging techniques facilitates the ability to obtain three-dimensional (3D) anatomical information about the human body. As a result, many medical image modalities exist. The diversity in these modalities is found to help by providing a specific information about human physiology.

Image registration is one of the most crucial image processing methods applied in many medical applications using image modalities, in which a point or a set of points is matched or aligned from one view to another. The mean of view is a two-dimensional space or three-dimensional space coordinates. There are many registration algorithms developed with different categories. Among of these categories are multi-modality and single-modality. In multi-modality, to better understand the organ physiology process, images obtained from different modalities need to be registered [9]. For example, liver images acquired from magnetic reasoning modality could be registered with images of the same organ obtained from computed tomography (CT) modality to analyze the change of a tumor shape or volume. In contrast, single modality images are registered for the same organ with the same modality acquired by the same machine but with different time.

Another registration category based on the transformation models is used to align a target image space to a reference image space. Among these transformation models; is elastic or nonrigid transform that used in deformable organ images registration. The registration of medical images poses some challenging barriers that need to be overcome. In most cases, the deformation is hard to determine because it differs mainly from a simple rigid-body or affine transforma-

tion. Instead, medical images usually require local and nonlinear deformations, which only an elastic deformation framework can handle properly. For elastic registration, one of the two volumes to be registered is deformable while the other volume is as a rigid reference. The aim of elastic registration is to map the deformable volume to the reference volume. In the human body, the liver is considered to be a deformable organ, while the brain (not during surgery) is rigid.

The registration technique used in this thesis is based on elastic solid mechanics and the minimum strain energy principle [87]. The aim is to get an optimum solution by minimize the following energy equation to get promising mapping result.

$$J = w_e E_e(x) + w_c E_c(x) + w_m E_m(x) \quad (2.1)$$

where  $E_e$  is strain energy produced by deformation of soft tissues,  $E_c$  is the distance between pairs of 3D vessel centerlines extracted from the fixed and moving images,  $E_m$  is the distance between corresponding point marks such as bifurcation points, and  $x_i$  is weight relative importance of each term. The aim of the above energy function is to measures the quality of mapping between two sets of blood vessels and the mapping between two sets of point marks, and the strain energy produced by soft tissue deformation.

## 2.4 Stereo Endoscopic

Scientists have long considered in what manner to use light source for seeing inside the human body, particularly where body organs are unreachable for medical investigation. The invention of the endoscope makes this possible by inserting light into the human body. The endoscope has two fiber bundles. The first bundle is used to illuminate the inner organs of the body. While the second

one is used to collect the reflected light from that area. [86],[51].

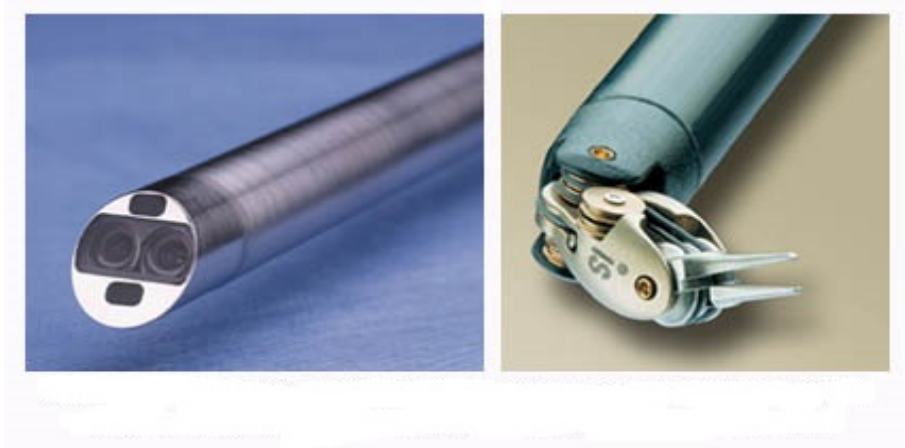


Figure 2.3: An stereo endoscope (left) peers inside the body to generate an image, while instruments like that at right perform surgical procedures

Hence, endoscopy plays a vital role in most of today's medical procedures. In addition, endoscope based minimal invasive abdominal procedures provide potential advantages over conventional open surgery such as reduced trauma, shorter hospital stay, and quick recovery [52]. One of the major drawbacks of the use of this technique is a small area that the endoscope covers resulting in the lack of proper 3D context of the surgical site. To solve this issue, real images should be captured during the surgery using endoscopes. The light source and the lens system fixed at the tip of the endoscope allow it to capture images of the area of interest and send these images to a computer for further processing. Reconstructing the surface of the organ is one of the best approaches to create a 3D virtual scene of the surgery in order to help surgeons make appropriate decisions during the surgery.

## 2.5 Literature Review

Developing a rapid and accurate framework for image processing of 3D MR liver images is a very challenging task. This literature review will discuss the related works to the methods proposed in this thesis.

Many features classification for liver segmentation methods of MR images are found in the literature. In [64] *Werghi et al.* use wavelet decomposition for feature extraction. In addition, Bayesian approach is used as a pattern classifier. *C. Juang and C. Chang* [13] used Fast Fourier Transform (FFT) to project histograms for human body features. Then they used Artificial Neural Network (ANN) for posture classification. The authors of [77] proposed a detection method of copy-move forgery. That method localizes duplicated regions within an image using Zernike moments. Since Zernike moments are algebraically invariant against rotation, their method able to detect a forged region even though in the case of image rotation, but cannot identify scaled regions as well as deformable regions. In addition, the authors in [58] proposed a method where they used the moment invariants to represent the shape of the brain structure in 8 scales. For each scale, an Artificial Neural Network (ANN) is designed to approximate the signed distance function of the desired structure. Also, they used the invariant to translation and rotation for their research problems; our method uses Geometric Moment for the affine transformation. The affine transformation is a more accurate representation of deformable liver patterns. Furthermore, we add extra parameters to the transformation matrix. Those parameters are scaling factors and rotation parameters.

*Ingela et al* [34] proposed a new method for segmentation and visualisation of three-dimension medical images. In that approach, they use haptic feedback and stereo graphics to obtain accurate 3D interaction. The haptic interaction is a force reflection device that allows a user to manipulate, feel, touch and alter simulated 3D objects. The basic idea of the haptic device is by using force display technology that senses the level of force applied to the users virtual world and responds accordingly. Therefore, the authors used a Phantom *Omni* device to perform different interactive segmentation algorithms, i.e. fast march-

ing, live-wire, and deformable models techniques. Also, the authors developed volume visualization and hardware acceleration. Using their method, Liver can be segmented by using the phantom pointer, which visually interacts with the object to perform the segmentation process. These interacts include specifying the seed points, detect the area of interest, and eliminates some areas from that process. The advantage of that method is the accuracy of the segmentation process. Hence, they obtained a mean precision of %96.9 of the fast marching algorithm, and they obtained a mean precision of %97.8 for simplex mesh segmentation. In contrast, the proposed method used very specific devices and list of parameters to run the pipeline. These parameters are related to the usage of advanced hardware as well as the haptic device.

The most relevant registration technique proposed in [74]. *Aylward et al.* described a ridge-based centerline tracking method. That method extracts centerlines for registration. However, the method had two main limitations. The seed points chosen to uniformly spanning the input image or by thresholding. That process leads to long processing time of the mentioned method. Secondly, the procedure generated a disconnected group of centerlines. They subsequently connected these centerlines by using straight cylinders between points. *Davis et al.* [53] proposed an elastic body spline (EBS) method based on elastic solid mechanics, which conforms to the physical model of the Navier-Cauchy equilibrium equation. Their method can reach an analytical solution. However, the EBS generally requires a specific polynomial i.e. radically symmetric force field, which does not necessarily reflect the real force field applied to the soft tissues in clinical practice. Moreover, their analytical solutions are only applicable to point-based registration procedures and cannot deal with the constraints associated with 3D curves such as blood vessel centerlines. In practice, reliably identifiable landmarks are often limited in soft tissues of real patients and are time-consuming to identify. On the other hand, blood vessels are often more

abundant and can be extracted more easily and reliably in many organs such as the liver, brain, lungs and kidneys. These vessels are good features and can provide reliable constraints to anchor deformable registration. Generally, EBS results in less accurate registration results due to the limited number of corresponding landmarks reliably identified in two images.

Deformation pattern is an important research problem since a good understanding of the pattern can help us to choose a suitable registration method for deformable tissue registration. However, there is few work in the literature to address and analyze the deformation pattern of the abdominal organs. In [33], the authors observed that, for 11 patients who underwent liver resection procedures, there is a significant shape discrepancy or deformation between the livers before the surgery and during the surgery, which is caused by natural mobility, flexibility, and surgical manipulation for resection. A solely rigid alignment of the preoperative and intraoperative images of the whole liver results in a large misalignment of anatomical positions by several centimeters due to varying tissue deformation patterns in different regions of the liver. However, the local deformation of the segmental structure of the liver can be depicted by smooth variation of the displacements, and after a local rigid alignment of the local anatomical structure, the residual discrepancy (i.e. pure deformation) is reduced to less than 5 mm. Therefore, based on the above results, the overall large displacement of the liver during liver resection can be modeled as different large rigid local motions plus relative small local deformations in different regions of the liver. In this research, we will analyze the deformation pattern of the liver and use the acquired knowledge of the pattern to formulate our registration method. We observed that surgeries often involve large displacements. However, in many scenarios, large rotation with small deformation is observed. For example, the displacement due to breathing or positioning can be modeled as large motion with small deformation. Moreover, in the non-surgical appli-

cations such as diagnosis or follow-up, minimal invasive (MIS) or noninvasive procedures such as radiotherapy, HIFU ablation [8], the assumption of large rotation with small deformation is often valid.

Developing a rapid and accurate approach to reconstruct the surface from stereo endoscopic images is a very challenging task especially for soft tissues with few features. Many techniques have been developed to acquire or reconstruct surgical surface such as using laser scanners and Time-Of-Flight (TOF) cameras [5] [50]. *Hayashibe et al.* used a laser-scan endoscope technique to reconstruct the shape and texture of the area of interest [55]. A laser scanner was proposed to acquire the liver surface for image-guided liver surgery, but it took about 5-20 seconds [49]. Therefore it is not suitable for free-breathing patients since average respiratory rates of children are 16-30 breaths per minute [31]. TOF cameras produce a depth map that can be immediately used to generate a 3D surface model in real time, but current devices are too large for endoscopic procedures [50] [5]. Furthermore, grid light pattern has been used for surface reconstruction in the previous researches. *Proesmans et al.* [70] presented an active 3D acquisition system that projects a simple pattern of squares on a scene and reconstructs the surface. They aimed automatically to detect the lines and intersection points (i.e. line crossings) of the projected pattern for surface reconstruction. *Hu et al.* [24] presented a method for 3-D surface measurement using a projected grid of light. The grid line identification problem is solved using very general constraints available in the physical world rather than resorting to some engineering approach. *Kawasaki et al.* proposed a technique to achieve dense shape reconstruction that requires only a single-frame image of a grid pattern [29]. The authors used coplanarity constraints for reconstruction by solving a set of linear equations. The major limitation of this technique is that it cannot be used when there exist nonlinear geometric distortions in projectors. In these studies, a single camera and a projector are used. To reconstruct the

surface of the scene, the relative spatial position of the camera and projector is fixed and calibrated. In a clinical environment, if either of them needs to be replaced, this configuration requires complicated calibration procedures to be performed that will interrupt the surgical procedures. In our study, this problem can be avoided since we do not need a fixed configuration between the projector and the stereo endoscope. Thus, our method allows easy change of projector or pre-calibrated stereo endoscopes without significant interruption of procedures.

In this thesis, we present a coherent and consistent framework for image processing. The aim of the proposed framework is to provide the physicians as well as the surgeons with an efficient and a robust tool for abdominal Magnetic Reasoning Imaging (MR) images visualization. The framework comprises of different processes (see Figure 1.1). These processes are: Pre-treatment high quality image acquisition, image segmentation, join deformable image registration/vessels segmentation, 3D surface reconstruction, and image visualization.

## **2.6 Thesis Outline**

This thesis focuses on particular types of image processing operations like: 3D surface construction, image registration, image segmentation, and points classification and detection. The thesis is arranged in 8 chapters of which Chapter 3 to Chapter 7 present the novel contributions of this research.

### **Chapter 2: Background and Related Work**

This Chapter provides a brief overview of the main topics and terms covered in this thesis. In particular, it gives a basic introduction of the principles of MRI modality and how MR images are obtained. Also, the chapter introduces the endoscopy device functionality, and its usage in the medical procedures. The

Chapter finishes by describing the image registration and image segmentation methods which will be used in this work.

### **Chapter 3: Segmentation of the liver from abdominal MR images**

The segmentation of the liver from abdominal MR images considers one of the hardest challenges in medical image processing. The difficulties are due to the enormous diversities of liver geometry between patients, or due to the large variations between images from the same patient. In this chapter, a new segmentation method is proposed that applied to MR images for the same patient.

My role in part of the research : I proposed and implemented the major part of this research.

### **Chapter 4: Seeds Classification for Image Segmentation**

In this chapter, we adopted the moment invariants used for shape detection to work for 3D seed points in MR abdominal images. The moments are invariant to affine transformation. we have demonstrated the effectiveness of the moments technique using the classified seed points to segment liver from abdominal MR images.

My role in part of the research : I proposed and implemented the major part of this research.

### **Chapter 5: Vessel-Based Fast Deformable Registration with Minimal Strain Energy**

In this chapter, we will present my participation in the development of a new approach to register deformable liver images. The approach uses 3D curves, point marks and minimum strain energy to obtain accurate registration results. Besides, it significantly reduces the number of transformation parameters in the

proposed neuro-fuzzy model.

My role in part of the research : I have helped to preprocess the MR images such as image preprocessing, centerlines extraction and bifurcation computation , and have implemented part of algorithm such as B-Spline curve fitting.

### **Chapter 6: Deformable Image Registration for Tissues with Large Displacement**

In this chapter, we will present my participation in the development of a new approach to register deformable liver images with large shift. In this research, we analyzed the deformation field of the liver by separating the deformation into rotation and pure deformation.

My role in part of the research : I preprocessed the images, centerlines, and bifurcation points, and I implemented part of the method.

### **Chapter 7: Automatic Surface Reconstruction for Endoscopy-MR Image Fusion**

Generally, developing a rapid and accurate approach to reconstruct the surface from stereo endoscopic images is a very challenging task especially for soft tissues with few features. In this chapter, we will demonstrate the effectiveness of the technique I developed by using dedicated gridline light patterns to create non-invasive artificial features on the tissue surface, which is then used to reconstruct a 3D surface robustly from stereo endoscopic images.

My role in part of the research : I proposed and implemented the major part of this research.

### **Chapter 8: Conclusion and Future Work**

The last Chapter of the thesis assesses the contribution of the research presented here and outlines some possible ideas for future work.

# Chapter 3

## Segmentation of the Liver From Abdominal MR Images

Segmentation is a key topic in computer vision and medical image processing. Furthermore, it is used in many registration methods. Hence, getting an accurate segmentation is a challenging task. The usage of prior knowledge in segmentation of abdominal MR images enables more accurate and comprehensive interpretation about the organ to be segmented. Great work has been done in segmentation algorithms for two dimensional images in the literature.

There are numerous challenges in liver segmentation in getting robust extraction of such organs. The difficulties of the segmentation process are due to the position and size of the liver. Moreover, the liver is surrounded with organs like the heart, the stomach, and the kidneys. When acquiring MR images of the abdominal, these organs have the same intensity as the liver. As a result, the boundary of the liver in some areas vanished and overlapped with these organs, which adding more challenges to the segmentation process (see Figure 3.1 and Figure 3.2). In addition, the quality of MR images acquired from different modalities is affected by terms like motion artifacts and signal to noise ratio.

There are many algorithms in the literature that present new methods and new techniques to improve the liver segmentation. These algorithms are divided into many categories [71]. Some of these categories base on training data set of liver shapes; other types base on statistical methods of detecting the liver shape. The common idea of the mentioned categories based on applying the method

on the whole shape of the liver. Since the liver is considered the biggest organ in the abdomen, the size and the shape of the organ changes within different slices. Hence, many algorithms get fair extraction results of the liver segmentation. The reason is the way they applied their algorithm or method. Some of the mentioned algorithms were able to segment part of the liver and failed to segment the other parts.

The usage of prior knowledge in segmentation of abdominal MR images enables more accurate and comprehensive interpretation about the organ to segment. Prior knowledge about abdominal organs like liver vessels can be employed to get an accurate segmentation of the liver that leads to accurate diagnostics or treatment plan [59],[56]. In this thesis, a new method for segmenting the liver from abdominal MR images using liver vessels as prior knowledge is proposed. The proposed method employs the technique of level set method to segment the liver from MR abdominal images. The speed image used in the level set method is responsible for propagating and stopping the region growing at the boundaries. As a result, the poor contrast of the MR images between the liver and the surrounding organs i.e. stomach, kidneys, and heart causes a leak of the segmented liver to those organs that lead to inaccurate or incorrect segmentation. For this reason, a second speed image is developed, as an extra term to the level set, to control the front propagation at the weak edges(i.e. edges overlies with edges from the enclosing organs) with the help of the original speed image. The basic idea of the proposed approach is to use the second speed image as a boundary surface which is parallel to the area of the leak. The aim of the new speed image is to slow down the level set propagation and prevent the leak before it occurs. The new speed image is a surface image created by using the end points of the prior knowledge vessels of the liver. The result of the proposed method shows superior outcome than other methods in the literature.

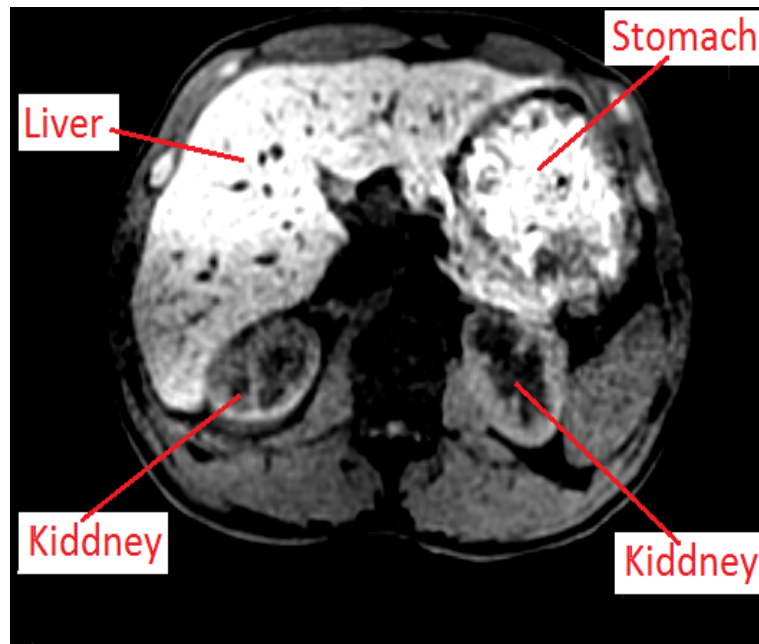


Figure 3.1: Example why liver segmentation is a challenging task. liver tissue has to be separated from adjacent organs

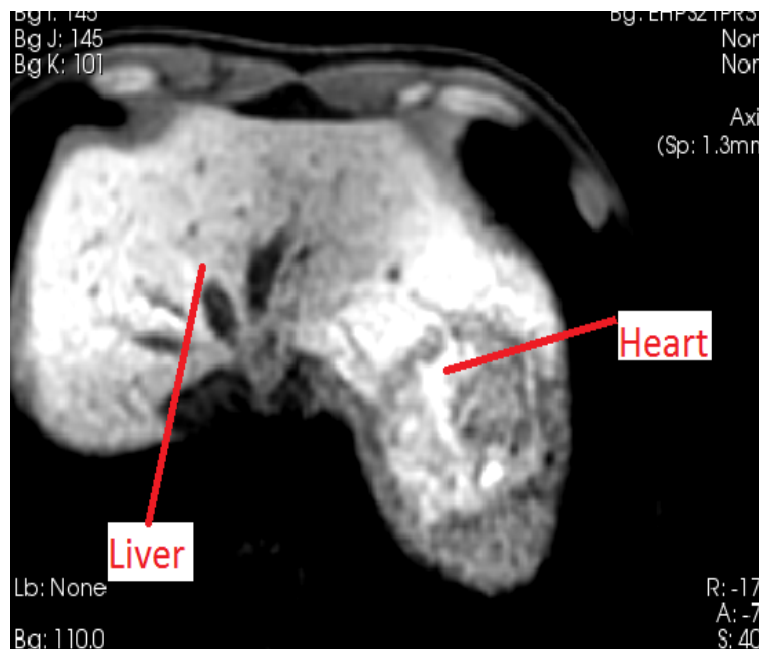


Figure 3.2: The gray-values in all structures are highly similar, which makes boundary detection difficult without a-priori information about the expected shape in these regions

### 3.1 Introduction

Magnetic resonance imaging (MRI) and computed tomography (CT) are used in diagnosis during surgeries, and in treatment procedures of tumors and malignancies throughout the world. The need for correct liver information, shape, and volume is crucial in any treatment or diagnose procedure. The difficulties of the segmentation process are due to the location and texture of the liver. Furthermore, liver is surrounded with organs such as the heart, stomach, and kidneys. These organs have a similar intensity as the liver [2]; as a result, there is an overlap of intensity of the liver and these organs, adding more challenges to the segmentation process. In addition, the quality of MR images acquired from different modalities is affected by terms like motion artifacts, signal to noise ratio, low contrast and blurred edges [84].

The over-segmentation problem in image segmentation is considered a critical issue and attracts many researchers. For instance, Heimann *et al* [79] solved the leakage problem by selecting a point in the erroneous area (where the leak is). Then they calculate a path to the seed point. Any point within that path has a shortest distance to the contour marks as thinnest connected regions to the chosen region and is thus considered the origin of the leak. To get the path they use a skeleton algorithm by thresholding the gradient magnitudes of the distance image. The part of the area where the user clicked is then removed from the segmentation. The advantage of the mentioned algorithm is simple and works in many cases while the drawback is if the bottleneck is not present or the deviation is too small the method will not work. In [76], a modified speed function is developed to prevent the leak before it happens. The method successfully prevented the bottom leak, but it could not prevent the top leak in a few middle slices of the volume. Lastly, they constrain the propagation of the liver contour using the distance computed in the speed function. The advantage is, the histogram shows that the majority of the slices are very well segmented.

Results indicate that the 2D version of the algorithm leads to better results than the 3D version.

In this thesis, a new method for segmenting the liver from abdominal MR images using liver vessels as prior knowledge is proposed. The proposed technique employs the level vessels to solve the over-segmentation problem by modifying the speed image used to evolve the level set function. The main idea is to modify the speed function by adding an extra term to block the leak before it happens. The new term is represented by a surface that is perpendicular to the segmented liver to stop the level set propagation from leaking.

## 3.2 Level Set Approach

Shape optimization plays an important role not only in image segmentation, but also in computational physics, fluid mechanics, optimal design and computer graphics. The aim of segmentation is to represent a curve of the object and evolve that curve. One straightforward method to describe a curve is by the points of the boundary using a simple polygon method or more sophisticated one using spline technique. That curve representation is called explicit parametric representation of the boundary. In that technique, a particular number of control points is used to evolve the curve. The advantages of explicit curve evaluation are the speed of implementation and memory efficient. The numerical prorogation of explicit method is prone to instabilities, as self-intersection of the curve have to be avoided, and regrading of the control points may be necessary. Alternatively to an explicit boundary representation, one can represent boundaries  $C$  implicitly. The central feature of the implicit method is that curves are represented using only geometric computation, independent of any parameterizations.

The curve evaluation denotes the movement of a curve over time. For ex-

ample, as the zero level set of an embedding function  $\phi : \Omega \rightarrow \mathfrak{R}$  :

$$C = \{(x, y) \in \Omega | \phi(x, y) = 0\} \quad (3.1)$$

where  $C$  denotes the curve or the boundary of an object,  $(x, y)$  represents the points in the image domain  $\Omega$  , and  $\phi(x, y)$  is a function with zero value at the boundary. The advantage of the method is that, the boundary representation does not required a choice of parameterizations. Meaning that, the points of the boundary are not explicitly encoded. One way to define  $\phi$  to have positive values outside the object's boundary and negative values inside the object's boundary is a distance function.

$$\phi(x, y, t = 0) = \pm d \quad (3.2)$$

where  $d$  is the distance from the point  $(x, y)$  to the boundary  $C$ . The distance function assigned to each point in the image to specify how far is that point from the boundary.  $C$  with negative values means the point of the image is inside the contour, and if  $C$  has a positive value means that, the point is outside the contour. Hence, complex boundary objects can be detected, and objects shape can be modeled using the level set method. Furthermore, merging and splitting of the boundaries are handled implicitly. Figure 3.3 shows the level set function, where the red circle represents the contour at  $C = 0$ , i.e.,  $((x, y) | \phi(x, y, t) = 0)$

The evolution equation of the level set function  $\phi(x, y, t)$  takes the following formula:

$$\phi_t + F|\nabla\phi| = 0 \quad (3.3)$$

where  $F$  is a speed function assigned to each point in the image domain and it used to stop or slow down the propagation of the curve in the vicinity of the boundaries.  $|\nabla|$  represents the normalized gradient of the level set function  $\phi$ . At any time  $t$ , the level set  $\phi(x, y, t) = 0$  always represents the propagation

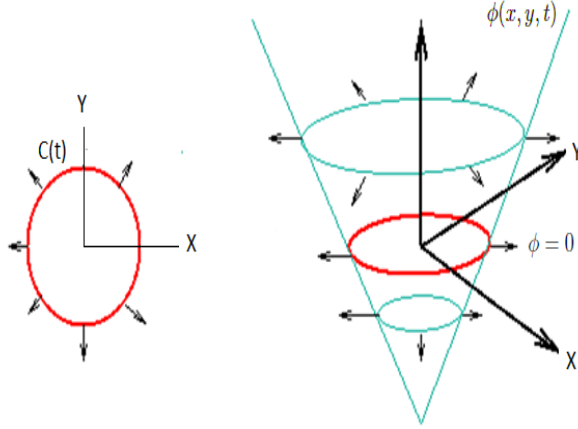


Figure 3.3: Level set: The contour of the level set function

front.

Generally, the speed function  $F$  can be represented as an explicit level set scheme :

$$F = F_{prop} + F_{curv} + F_{adv} \quad (3.4)$$

Where  $F_{prop}$  represents a term used to stop the curve propagation near a region with high gradient points,  $F_{curv}$  is the curvature term which depends on the geometry of the front. The term  $F_{adv}$  referred to the advection term, which is independent of the geometry of the moving front. The front shaped uniformly by expanding or shrinking with speed  $F_{adv}$  [85]

### 3.3 The Proposed Speed Function

In the proposed thesis, we modified the speed function in Equation 3.4 by adding another term. The new term is used in some regions of the image which cause the leak. The new term plays as a surface closed to the boundary of the liver to stop the speed function from leaking. We can rewrite the speed function in Equation 3.4 as follows:

$$F = F_{prop} + F_{curv} + F_{adv} + F_{sur} \quad (3.5)$$

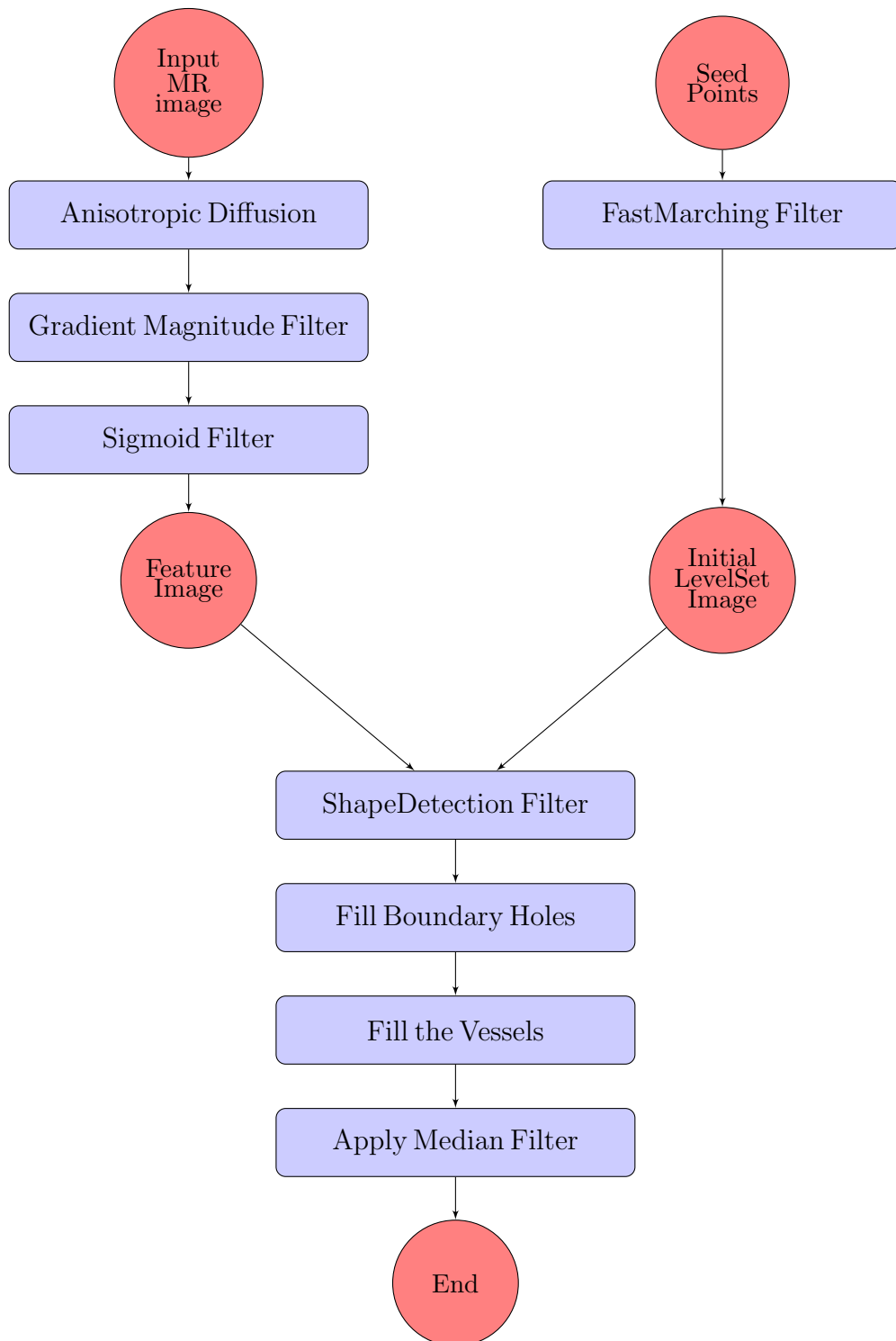


Figure 3.4: The proposed method flowchart

$F_{sur}$  refers to the surface speed term added to the original speed function. As a benefit of adding the new term, we can modify the front propagation value of each pixel in the image domain. To detect the boundary points, the front propagation is calculated at any pixel in the image a time  $t$ . Furthermore, time  $t + 1$  can be calculated to decide if the next level pixel is a boundary pixel or not by using the following:

$$\phi_{i,j,k}^{t+1} = \phi_{i,j,k}^t - \Delta t \cdot F |\nabla_{i,j,k} \phi_{i,j,k}^t| \quad (3.6)$$

By using the new added term we use Partial Differential Equation (*PDE*) to compare the front propagation value of any pixel and any time  $t$  and the value of the surface term  $F_{sur}$  at that pixel.

### 3.4 Materials and Methods

In this thesis, we propose a new method based on the shape detection method [72] proposed by Malladi *et al.* to segment the liver from MR images. Four seeds were selected to generate the initial level set input (see Figure 3.4). We use fast marching method [7] to generate the first input of the application (see Figure 3.5). The first input used to initialize the level set in form of image format where  $\phi(x, y, t) = 0$ . The four seeds represented with dark spots in the image, where the center of the spot has a distance value = 0.0 (marked with circle). The value of the distance increased when the points were far away from the center of the spot based on Equation 3.2. The second input is the feature image. Anisotropic diffusion filter is used to smooth the input image, the smoothed image passed to gradient magnitude filter, and then to sigmoid filter to generate the speed image Figures 3.6, 3.7, 3.8, and 3.9. while the third input to the application is the surface patch image, which is generated to be a leakage blocker.

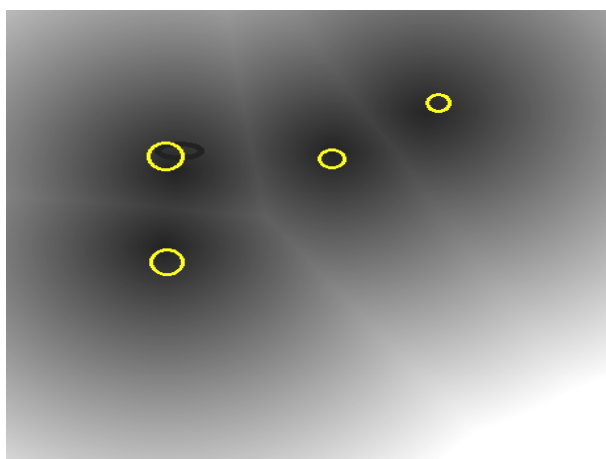


Figure 3.5: The input level set used in the proposed method

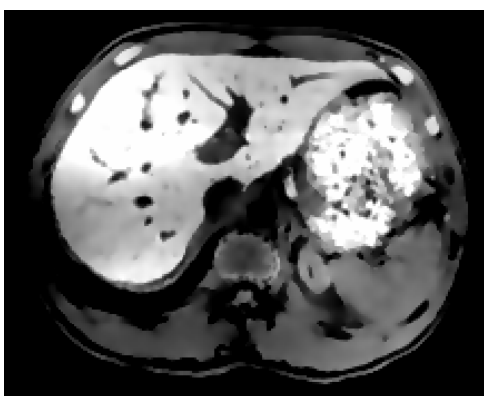


Figure 3.6: The input image of the segmentation process

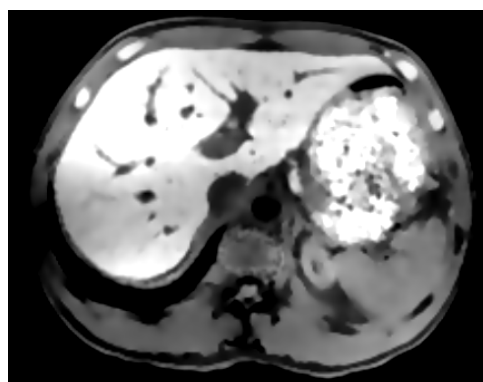


Figure 3.7: Image smoothed with an edge-preserving smoothing filter

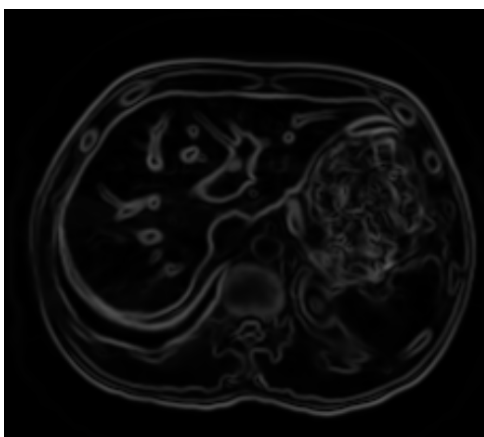


Figure 3.8: Gradient magnitude image of the smoothed image

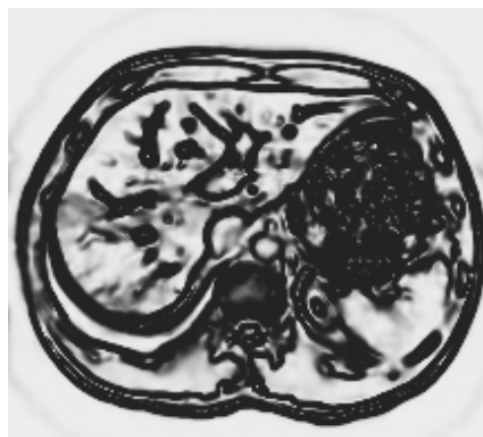


Figure 3.9: Sigmoid output of the gradient magnitude image

The surface is generated by using the prior knowledge to generate surface patches in regions within the image. These regions represent the veins exit of the liver, where the chance of a leak is high. The end points of the vessel structure are used to detect these regions. Furthermore, these end points used to generate a surface patch for each region. The next step is to fill the holes within the generated surface. For that purpose, we used the method in Section 3.5. Finally, the segmented model has a vessels structure. To fill the inside vessels of the generated model, we use the simple region growing algorithm with radius = 4. Input seeds are used from the vessels centerlines to guide the region growing process. Some tiny gaps are noticed between the inside structure of the segmented model and the filled vessels. As a post process, we use the median filter to fill any lifted gaps or spaces between the filled vessels using region growing and the segmented structure.

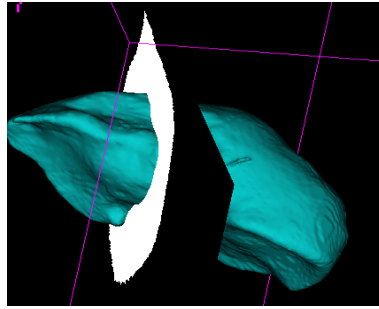


Figure 3.10: The surface patch image proposed

### 3.5 Filling the Surface Holes

As a result of segmentation, the surface of the segmented model contains some holes. These holes are located at the exit of the hepatic veins of the liver. To fill these holes, we generated a surface patch which is perpendicular to the model to fill the gap within the holes boundary. For that purpose, we consider a surface patch as a bunch of points. These points can be represented by a quadratic equation as follows:

$$f(x) = c_2x^2 + c_1x + c_0 \quad (3.7)$$

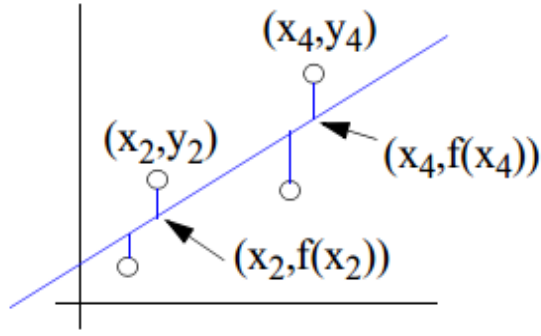


Figure 3.11: Least square fitting line

where  $c$  denotes the coefficients of the equation. Then we can use the following fitting function to minimize the error using square fitting technique.

The square fitting technique uses the following formula to calculate the minimum distance between the data values and the points on the fitted surface, (see Figure 3.11).

$$err = \sum (dist_i)^2 = (y_1 - f(x_1))^2 \cdots (y_i - f(x_i))^2 \quad (3.8)$$

where  $f(x_i)$  denotes the data values to be fitted,  $y_i$  denotes points in the fitted surface. Now substitute the form of equation 3.7 into the general least squares error equation 3.8

$$err = \sum_{i=1}^n (y_i - (c_2x^2 + c_1x + c_0))^2 \quad (3.9)$$

$n$  is the number of data points,  $i$  is the current data point being summed of the quadratic polynomial order. To minimize the error of Equation 3.9, we take the derivative with respect to each coefficient  $c_0$ ,  $c_1$  and  $c_2$ .

$$\frac{\partial err}{\partial c_0} = 2 \sum_{i=1}^n (y_i - (c_2x^2 + c_1x + c_0)) = 0 \quad (3.10)$$

$$\frac{\partial err}{\partial c_1} = 2 \sum_{i=1}^n (y_i - (c_2 x^2 + c_1 x + c_0)) x = 0 \quad (3.11)$$

$$\frac{\partial err}{\partial c_2} = 2 \sum_{i=1}^n (y_i - (c_2 x^2 + c_1 x + c_0)) x^2 = 0 \quad (3.12)$$

These lead to the following equations:

$$\begin{aligned} c_0 n + c_1 \sum_{i=1}^n x_i + c_2 \sum_{i=1}^n x_i^2 &= \sum y_i \\ c_0 \sum_{i=1}^n x_i + c_1 \sum_{i=1}^n x_i^2 + c_2 \sum_{i=1}^n x_i^3 &= \sum x_i y_i \\ c_0 \sum_{i=1}^n x_i^2 + c_1 \sum_{i=1}^n x_i^3 + c_2 \sum_{i=1}^n x_i^4 &= \sum x_i^2 y_i \end{aligned}$$

Next, we rewrite these equations and put them into a matrix form:

$$\begin{pmatrix} n & \sum x_i & \sum x_i^2 \\ \sum x_i & \sum x_i^2 & \sum x_i^3 \\ \sum x_i^2 & \sum x_i^3 & \sum x_i^4 \end{pmatrix} \begin{pmatrix} c_0 \\ c_1 \\ c_2 \end{pmatrix} = \begin{pmatrix} \sum(y_i) \\ \sum(x_i y_i) \\ \sum(x_i^2 y_i) \end{pmatrix}$$

The above equation is in the form of  $AX = B$ , where  $A$  and  $B$  are known, while  $X$  is unknown. The coefficients can be obtained by solving:

$$X = A^{-1} * B$$

To generate a surface patch to fill a hole, one point is selected within the hole (inside the surface) and another point outside the hole where these points should be orthogonal. The inside point can be selected by using the end point of vessels structure as shown in Figure 3.12 .

## 3.6 Data and Validation

In this section, the segmentation result of liver MR image using the proposed segmentation method is presented. The testing image used in this thesis was obtained from human volunteer. High-quality dynamic MR image was acquired

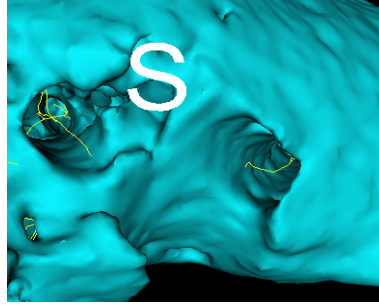


Figure 3.12: Filling the liver surface holes using surface fitting technique

in the axial plane using a 1.5T GE scanner (GE Medical Systems, Milwaukee, WI). Image acquisition was performed using the LAVA gradient echo sequence with TR=3.79 ms, TE=1.72 ms, a flip angle of 12 degrees, the image matrix size of 256 x 256, in-plane pixel size of 1.3 mm x 1.3 mm and slice thickness of 1.5 mm. Note that, in image acquisition, TR (Repetition Time) represents the amount of time that exists between successive pulse sequences applied to the same slice. See also Repetition Time. While, TE (Echo Time) - represents the time in milliseconds between the application of the 90 ° pulse and the peak of the echo signal in Spin Echo and Inversion Recovery pulse sequences [73].

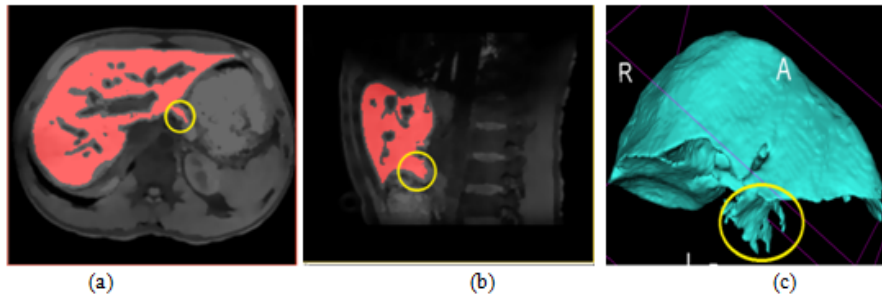


Figure 3.13: The segmentation result before applying the proposed method, the leaking region is highlighted with circle

Before implementing the proposed method, Figure 3.13 shows the leak region (with yellow circle) in the axial and sagittal views. It is clear that the boundary at the region has poor contrast; hence the leak took place to the surrounding organ. Furthermore, Figure 3.13(c) shows the surface model generated of the segmented volume before applying the proposed method. Figure

3.14 shows the results after applying the proposed method for the same region as images in Figure 3.13. It is obvious that the leak vanishes with keeping the same structure as the input mode. Figure 3.14 c, and d represent the result of the filling holes algorithm implemented in this thesis. Although most of the holes relatively large in diameter, the hole filling algorithm is able to fill these holes with the help of the prior knowledge of liver vessels.

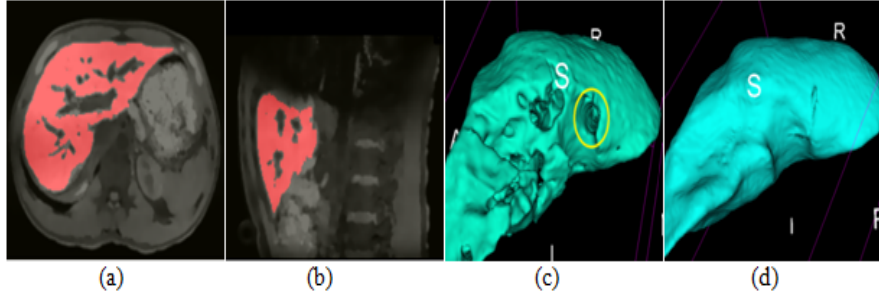


Figure 3.14: The segmentation result after applying the proposed method

### 3.6.1 Segmentation Accuracy Measures

In order to evaluate the quality of our proposed registration approach, we adopt the following two accuracy measures to assess the registration accuracy. The obtained segmentations have been evaluated by two metrics based on the ones described on [78]. These two metrics are as follows:

- Volumetric Overlap Error (VOE): In Volumetric overlap error we use  $G$  and  $S$  to denote the set of points of the ground truth segment and the computed segment respectively. The value is 1 for a perfect segmentation, and a value of 0 denotes to a completely failed one.

$$E_D = 2|S \cap G|/(|S|+|G|)$$

- Relative Volume Difference (RVD):

$$RVD = ((V_s - V_g)/V_g) * 100$$

where  $V_g$  is the volume of the golden set and  $V_s$  is the volume of the segmentation. The best value is 0 (for perfect volumes) and the worst one is 100.

### 3.7 Summary

In this thesis, a new solution is proposed to solve the leak problem in segmentation using the level set method of MR images for the same patient. The proposed method uses a second speed image acting as a surface blocker to prevent and pull back the propagation front when crossing the liver boundary. A prior knowledge about the liver has been used to generate the second speed image as well as to generate the surface patches to fill the segmented surface holes. The Volumetric Overlap Error (VOE) of the proposed method with a golden set model is 0.84, while the Relative Volume Difference (RVD) is 6.14% which is an excellent result comparing with algorithm mentioned in [79]. In the future, we will perform more validation experiments using clinical data. Moreover, we will investigate the effects of different MR contrasts in the proposed segmentation. We also plan to extend our techniques to multimodality image registration such as CT images.

# Chapter 4

## Seeds Classification for Image Segmentation

Image segmentation is a crucial topic in computer vision and medical image processing. However, accurate image segmentation is still a challenging task for many medical applications. The region growing based image segmentation process starts by selecting seed points within the region of interest. Hence, the segmentation algorithm is sensitive to the initial seeds and the result can be influenced greatly by the accuracy of seed selection process. Manual seed selection can be time-consuming and requires an expert to complete the selection. In this thesis, we propose an innovative approach to automating the initialization process of the liver segmentation of magnetic resonance images. The seed points, which are needed to initialize the segmentation process we proposed in [1], are extracted and classified by using affine invariant moments and artificial neural network.

We calculated eleven invariant moments for 56 different points within the region of interest. These points represent the bifurcation points of the vessels centerlines of the liver. In this thesis, we divide the shape of the liver into four regions; left hepatic vein, center hepatic vein, hepatic portal vein, and right hepatic vein. Then, the moments are classified by an artificial neural network to decide to which part of the liver each point belongs.

We have validated our proposed technique by comparing the method with manual seed selection. The experimental results show that our method outper-

forms the manual method in terms of the accuracy of seed point selection and the speed of the process. The proposed technique is used for automatic seed point selection and classification. The selected seed points are used to initialize the segmentation process. The aim of this method is to automatically detect and identify the seed points in MR images.

## 4.1 Introduction

Image segmentation is one of the most fundamental processes in medical image processing. Many radiological evaluations and diagnoses are based on image segmentation. The aim of any segmentation process is to classify an image into different distinction clusters or regions. For example, in magnetic resonance imaging (MR) abdominal images, segmentation is used to identify organs such as; the heart, brain, liver, lungs, and stomach. The clarification process is based on grouping together image pixels that have the same characteristics. Segmentation could be performed by edge-based, pixel-based, or region-based methods. In the edge-based method, edge knowledge is used to recognize the boundaries of the image objects. In some cases, the boundaries are analyzed and modified to get the closed boundary of the object. While in the pixel-based method, segmentation can be implemented by using image histogram to determine a typical gray level for each object. Lastly, in the region-based approach, the segmentation process should detect homogeneous regions in such a way that these regions satisfy certain homogenous criterion [27]. In general, segmentation of MR images is a challenging task in image analysis, as it is extremely challenging to obtain a perfect segmentation method that fits all images. The challenge of the segmentation process is due to the position of the liver in the abdominal. Since, the liver is surrounded by organs such as the heart, the stomach, and the kidneys. These organs have a similar intensity pattern as the liver that adds more challenges to the segmentation process. Also, the quality of MR images acquired from different modalities affects by terms like motion artifacts, signal

to noise ratio, low contrast and blurred edges.

The level set method is a region-based technique that is considered to be one of the superior segmentation methods. The level set methodology represents the boundary of an object implicitly by implementing an only geometric computation, independent of any parameterizations [60]. Segmentation methods based on the level set approach are initialized by some seed points to start the process. Those seed points are considered as feature points in the objects to be segmented. Also, the feature points of an object should be not changed if the object has been transformed or has been changed geometrically. We proposed a segmentation method to extract the liver from an abdominal MR images using the level set technique [1]. In the proposed method, the segmentation process is initialized by selecting some seed points in the area of interest. The selection of those seed points is performed manually each time until the segmentation is established. The selection of seed points is time-consuming and requires an expert to perform such selection. The accuracy of the proposed segmentation is based on many factors; one of these factors is the distribution and the location of the seed points. Hence, the seed points should be selected from different areas of the liver. To obtain that, we divide the model of the liver into four lobes.

Feature extraction is the process of reducing of resources required to describe an object or a large set of data [27]. Also, it is an essential process in most image analysis applications, such as image registration, image segmentation, object recognition and classification [25],[82],[10],[94]. Therefore, the overall performance of the application depends on the accuracy of the extracted features [14]. Numerous techniques have been developed to extract the representations of object features. Feature extraction methods that exist in the literature all have their advantages and disadvantages. Therefore, it is important to recognize the best feature extraction methods for a particular application. The authors

in [42] developed a four steps method to select a seed. First, they select random seed points from a map image. The map image is generated by smoothing the image by Gaussian convolution to reduce the noise. Next, the seed points are selected from the distance map image by using high and low thresholds. The thresholds value is automatically selected using the histogram of the initial image. Finally, pixels with the maximum distance to the nearest edge is chosen as seed points. The major drawback of this technique is that it cannot be used by MR images with largely deformable tissue.

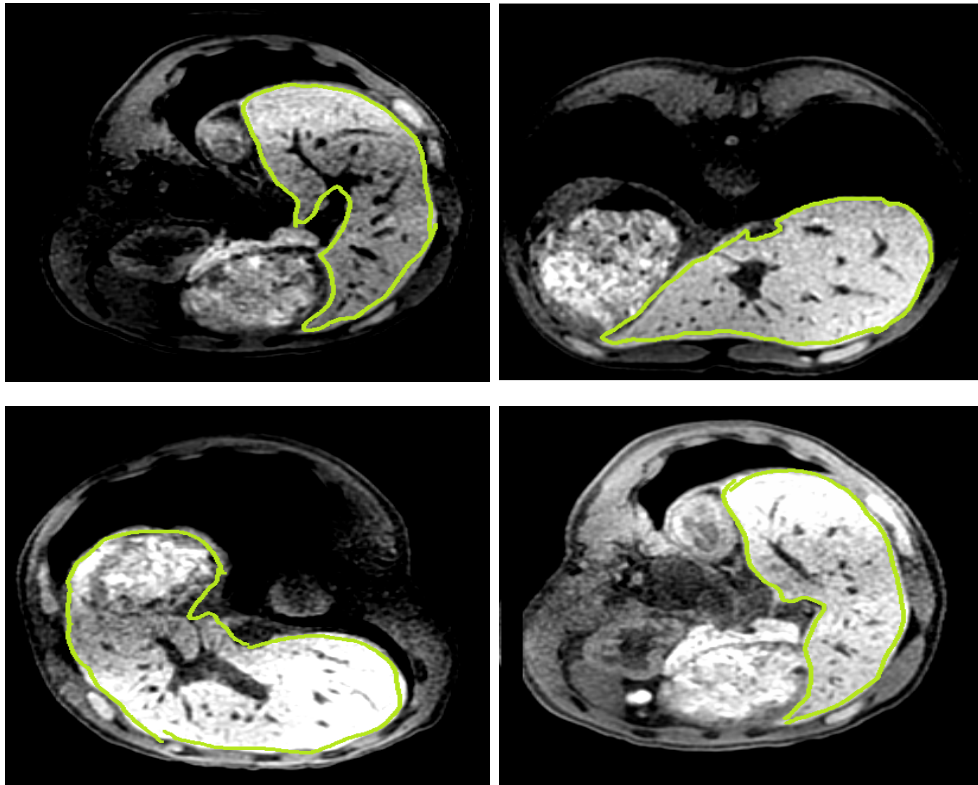


Figure 4.1: MR images with different positions from the same subject

Moments is considered to be one of the reliable and most robust feature extractors. Furthermore, moments are a set of nonlinear functions that build a quantitative measure of an object or set of points of that object. These moments are invariant to translation, scale, and orientation. Also, these moments are calculated based on a density function (e.g. image intensity). The moment invariants technique is widely used for region description in image processing,

pattern recognition, remote sensing, and classification [40]. Moment invariants are extensively used in literature for two-dimensional image analysis [46], and have been extended to three-dimensional pattern only much later [38], [6]. They have not been applied to problems in image segmentation techniques yet. Furthermore, moment invariants are suitable to some of the most useful statistical classifiers such as an artificial neural network (ANN). These networks are broadly used in image enhancement, segmentation, and registration. Multi-Layer Perceptron (MLP) is one type of feedforward ANN, in which an input data set is mapped onto a set of appropriate outputs. The authors in [58] proposed a method where they used the moment invariants to represent the shape of the brain structure in 8 scales. For each scale, an Artificial Neural Network (ANN) is designed to approximate the signed distance function of the desired structure. Also, they used the invariant to translation and rotation for their research problems; our method uses Geometric Moment for the affine transformation. The affine transformation is a more accurate representation of deformable liver patterns. Furthermore, we add extra parameters to the transformation matrix. Those parameters are scaling factors and rotation parameters.

The proposed method efficiently calculates the moments of a given seed point. The moments are invariant to rotation, scaling, and transformation, hence, they are suitable for affine transformation and deformable objects. In this study, the extracted features are fed into statistical classifiers via a supervised training scheme. The result of the classifying process determines the area of the liver each point belongs to. Then the classified seed points are used to initialize the level set segmentation method we proposed in [1]. The overall framework is evaluated by using synthetic images as well as novel MR images.

The novelty and contribution of the proposed work lie in the classification and automatic characterization of 3D points using 3D moment invariants and

neural network. In this research, 56 feature points were selected in abdominal MR images from the same subject to get the moments under affine transform. These points represent the vessels bifurcation in the liver. The approach is based on a descriptor, capturing the essentials of the seed points in the image to be segmented to form a vector of 3D moment invariants. The neural network is trained on the first MR image and after that, the method eliminates the need for manual selection of seed points in any future image segmentation for the same subject. Furthermore, the proposed method can handle affine transformation, and is very runtime efficient. In the rest of this chapter, we will briefly introduce the 3D moment invariants used in this research. Next, we will describe the representation of the seed points such that moment invariants can be computed to start the level set segmentation process. Lastly, in order to demonstrate the power of the proposed descriptor, we will present the extraction and the classification experiment results of a set of 56 seed points as well as the segmentation result.

In this thesis, the extracted features are fed into statistical classifiers via a supervised training scheme. The result of the classifying process determines the area of the liver each point belongs to. Then the classified seed points are used to initialize the level set segmentation method. The overall framework is evaluated by using synthetic images as well as novel MR images. In the rest of this chapter, we will briefly introduce the 3D moment invariants used in this thesis. Next, we will describe the representation of the seed points such that moment invariants can be computed to start the level set segmentation process. Lastly, in order to demonstrate the power of the proposed descriptor, we will present the extraction and the classification experiment results of a set of 56 seed points as well as the segmentation result.

## 4.2 Material and Methods

The first step is to convert the image to a binary image (see Figure 4.2). In Figure 4.3, the binary image is further manipulated by a padding filter to expand the boundary by padding each dimension with a predefined value. The reason for the padding process is to keep the pixels of the image within its space after the applying affine transformation to that image. Next we calculate the moments of the landmarks of the image. In this research, landmarks were defined as bifurcation points of blood vessels and were located in the MR image spaces. Figure 4.4 shows a schematic diagram of the proposed method.

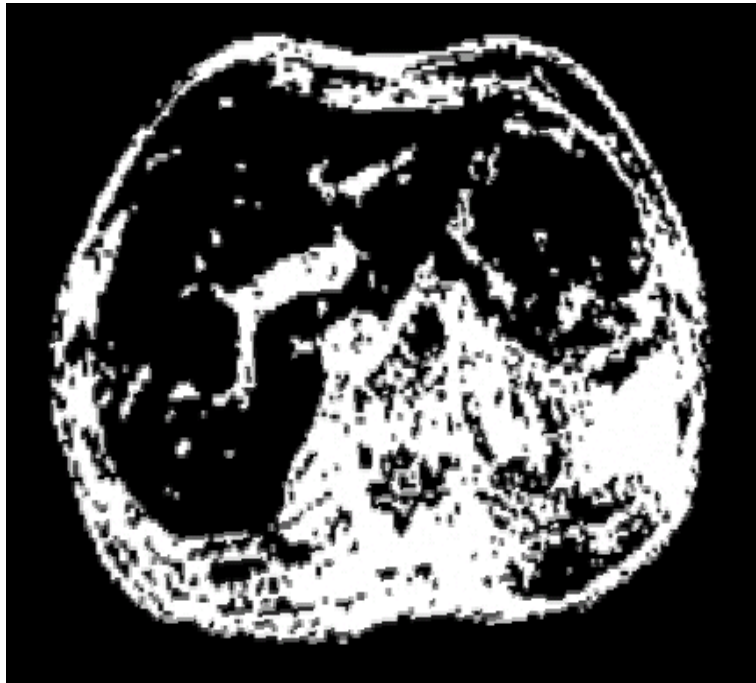


Figure 4.2: A binary Image of the input image

### 4.2.1 Moments Invariant

In this step, the features of the input image are extracted. A feature can be an intensity value, edge, corner, texture, shape, etc. In this thesis, the classification of the seed points considers features of an input image. The seed points are the bifurcation points of the vessel centerlines of the liver to be segmented. Moments as an invariant feature vector have been used in this project to rec-

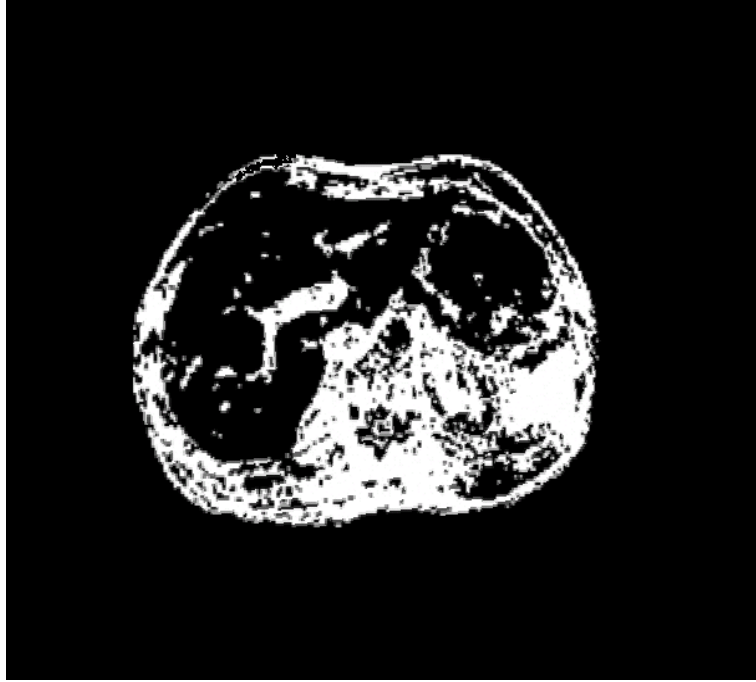


Figure 4.3: The image after applying a padding filter

ognize the test object from a dataset. The use of moment invariant provides a unique identification for each object irrespective of its affine transformations.

Random variables can be discrete or continuous. A discrete random variable can only hold a particular value while continuous random variables can take any values within range. Associated with a random variable  $Y$  is a Probability Density Function  $f(y)$ , such that the probability of the random variable  $Y$  is to be between two particular numbers  $m$  and  $n$  with  $m \leq n$  is given by Equation 4.1

$$P(m \leq Y \leq n) = \int_m^n f(y)dy \quad (4.1)$$

where  $P$  represents the value of the probability in the interval  $[m; n]$ , which calculated by the area between the interval  $[m; n]$  and under the curve of the density function. The curve of the density function is represented by the graph of  $f(y)$ . Therefore, the probability of a density function of three variables

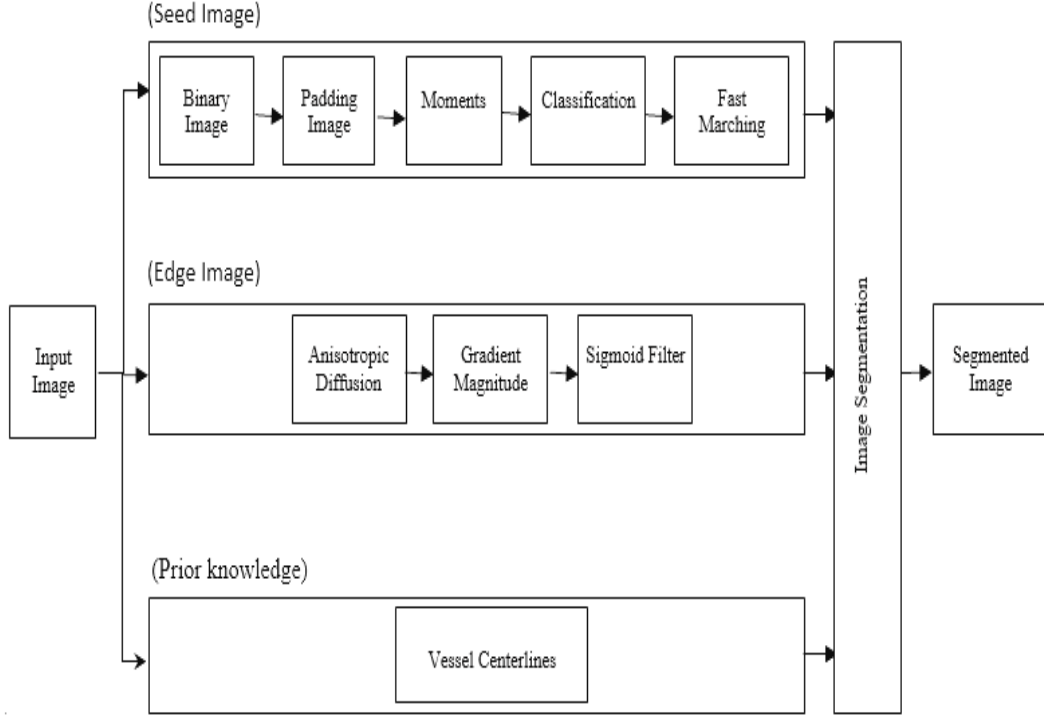


Figure 4.4: Schematic diagram for the proposed classification method

$(x, y, z)$  if defined by :

$$p(x, y, z) = \int \int \int f(x, y, z) dx dy dz$$

The moment of a random variable or the moment of its distribution is just the expected value of a power of that random variable. While the expectation of a random variable is a sum or integral of all possible values of the random variable weighted by their associated probability [28].

The 3-D moments of order  $n = (p + q + r)$  of a 3-D density function  $p(x, y, z)$  is defined by the following:

$$M_{pqr} = \int_{-\infty}^{\infty} \int_{-\infty}^{\infty} \int_{-\infty}^{\infty} x^p y^q z^r p(x, y, z) dx dy dz \quad (4.2)$$

where  $M_{pqr}$  is a moment of order  $(p + q + r)$ . We rewrite Equation 4.2 to be

suitable for image digitized as follows:

$$M_{pqr} = \sum_{x=-\infty}^{\infty} \sum_{y=-\infty}^{\infty} \sum_{z=-\infty}^{\infty} x^p y^q z^r f(x, y, z) \quad (4.3)$$

where  $x, y$  and  $z$  are the pixel coordinates of the seed points. Using the central moment, we can achieve the translation invariance of the moment. The following is how we can get the central moment:

$$\mu_{pqr} = \int_{-\infty}^{\infty} \int_{-\infty}^{\infty} \int_{-\infty}^{\infty} (x - x_c)^p (y - y_c)^q (z - z_c)^r f(x, y, z) dx dy dz \quad (4.4)$$

or in digitized images over a discrete function  $f(x, y, z)$ , we can define the moments over a domain of  $M \times N \times O$  discrete points, as follows:

$$M_{pqr} = \sum_{x=0}^{M-1} \sum_{y=0}^{N-1} \sum_{z=0}^{O-1} (x - \bar{x})^p (y - \bar{y})^q (z - \bar{z})^r f(i, j, k) \quad (4.5)$$

where  $\bar{x}, \bar{y}$ , and  $\bar{z}$  are the central moments that denote the coordinates region center of gravity. Central moments calculated by:

$$\bar{x} = \frac{M_{100}}{M_{000}}, \quad \bar{y} = \frac{M_{010}}{M_{000}}, \quad \bar{z} = \frac{M_{001}}{M_{000}}, \quad (4.6)$$

In this research, the value of the probability density function  $p(x, y, z)$  is equal to 1, because we deal with binary images. For the sake of simplicity, we moments of order higher than three will not be considered in this research. The complex moments presented in this research are constructed using complex polynomials which form an entire orthogonal model defined on the unit disc  $(x^2 + y^2 + z^2) \leq 1$ . The coefficients and the variables of complex polynomials are complex numbers in the form  $a + jb$ , where  $j = \sqrt{-1}$ . The homogeneous polynomial space  $P_n$  represents complex moments. The space of homogeneous polynomial of order  $n$  decomposed itself into subsequences. Hence, the moments are transformed into complex moments  $v_l^m$ .

Rotation invariant is derived from  $v_i^m$  using the tensor product to  $v_0^m, v_1^m, v_2^m$  and  $v_3^m$ . These invariants turn out to be homogeneous polynomials of central moments. Because of numerous symmetries, the tensor products results only in twelve invariants [30].

In this thesis, 11 invariants have been generated for four seed points of an MRI image. These points are located in different regions in the liver, i.e. left hepatic vein, center hepatic vein, hepatic portal vein, and right hepatic vein. The MR images acquired for the same subject, but in different positions.

The invariants are used in this thesis are listed below:

1.

$$I_{22}^2 = \frac{v(2, 2)_0^0}{(v_0^0)^2} \quad (4.7)$$

2.

$$I_{222}^2 = \frac{\eta v}{(v_0^0)^3} \quad (4.8)$$

3.

$$I_{33}^3 = \frac{v(3, 3)_0^0}{(v_0^0)^{12/5}} \quad (4.9)$$

4.

$$I_{11}^3 = \frac{v(1, 1)_0^0}{(v_0^0)^{12/5}} \quad (4.10)$$

5.

$$I_{233}^{2.3} = \frac{v(3, 3)_2 V_2}{(v_0^0)^{17/5}} \quad (4.11)$$

6.

$$I_{123}^{2.3} = \frac{v(3, 1)_2 V_2}{(v_0^0)^{17/5}} \quad (4.12)$$

7.

$$I_{112}^{2,3} = \frac{v(1,1)_2 V_2}{(v_0^0)^{17/5}} \quad (4.13)$$

8.

$$I_{3333}^3 = \frac{v^2(3,3)_2}{(v_0^0)^{24/5}} \quad (4.14)$$

9.

$$I_{1333}^3 = \frac{v(3,3)_2 v(3,1)_2}{(v_0^0)^{24/5}} \quad (4.15)$$

10.

$$I_{1133}^3 = \frac{v^2(3,1)_2}{(v_0^0)^{24/5}} \quad (4.16)$$

11.

$$I_{1113}^3 = \frac{v(3,1)_2 v(1,1)_2}{(v_0^0)^{24/5}} \quad (4.17)$$

For the sake of simplicity, I will present how we can get the value of the Invariant

4.7. The value of  $v(2,2)_0^0$  term can be obtained by :

$$v(2,2)_0^0 = \frac{2\pi}{15\sqrt{35}} \left( \frac{8}{3} J_1^2 - 8J_2 \right) \quad (4.18)$$

and

$$v_0^0 = \frac{2\sqrt{\pi}}{3} J_1 \quad (4.19)$$

where

$$J_1 = M_{200} + M_{020} + M_{002} \quad (4.20)$$

and

$$J_2 = M_{200}M_{020} + M_{200}M_{002} + M_{020}M_{002} - M_{101}^2 - M_{110}^2 - M_{011}^2 \quad (4.21)$$

To clarify the concept of moments invariant, the following is an example of getting the first invariant listed in Equation 4.7 of a seed point. First, the neighbourhood of the input seed point is located. The size of the neighbourhood

is  $5 \times 5 \times 5$  pixels as shows in Figure 4.5, while the seed point is located at the center of the cube.

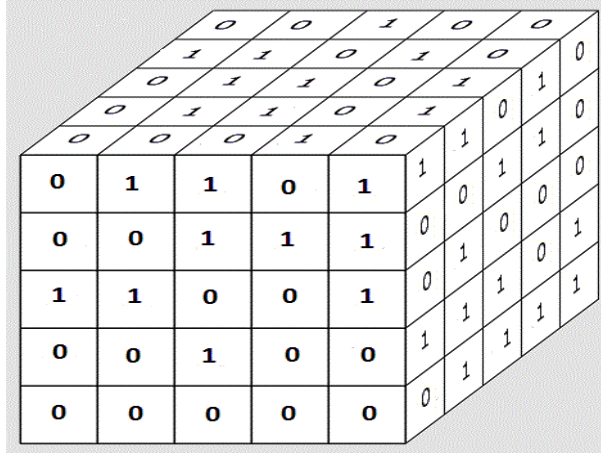


Figure 4.5: The neighbourhood pixels of a seed point

The following step is iterate the vicinity of the seed point to get the moments based on Equation 4.5. First the central moments  $\bar{x}$ ,  $\bar{y}$ , and  $\bar{z}$  are calculated based on Equation 4.6. The algorithm applied to generate these central moments is shown in the following pseudo-code. The central moments are used to get the rest of moments invariants based on Equation 4.5. The following pseudo-code shows the algorithm used to calculate the rest of the moments.

The value of the first moment invariant shown in Equation 4.7 is based on solving Equation 4.18 and Equation 4.19 respectively.

### 4.2.2 Affine Transformation

The seed points used in this experiment are located in the liver of abdominal MR images. We use affine transformation to handle the deformable issue of the training images. A 3D affine transform of a point  $p$  with coordinates  $(x, y, z)$  to another point  $p'$  with coordinates  $(x', y', z')$  in matrix form as:

$$x' = AX + b \tag{4.22}$$

```

Data: Binary image
Result: The generation of central moments
initialization;
while not at end of the seed neighbour do
    Get the current pixel value (pixelVal);
    if pixelValue > 0 then
        get the physical space coordinate of the current index (pixelPoint[]);
         $M_{000} += \text{pixelVal};$ 
         $M_{100} += \text{pixelPoint}[0] * \text{pixelVal};$ 
         $M_{101} += \text{pixelPoint}[0] * \text{pixelPoint}[2] * \text{pixelVal};$ 
         $M_{001} += \text{pixelPoint}[2] * \text{pixelVal};$ 
    else
        Get the next pixel;
    end
end
 $\bar{x} = \frac{M_{100}}{M_{000}};$ 
 $\bar{y} = \frac{M_{010}}{M_{000}};$ 
 $\bar{z} = \frac{M_{001}}{M_{000}};$ 

```

**Algorithm 1:** The generation of central moments

where

$$x' = \begin{bmatrix} x' \\ y' \\ z' \end{bmatrix}, A = \begin{bmatrix} i_1 & i_2 & i_3 \\ j_1 & j_2 & j_3 \\ k_1 & k_2 & k_3 \end{bmatrix}, X = \begin{bmatrix} x \\ y \\ z \end{bmatrix}, b = \begin{bmatrix} i_0 \\ j_0 \\ k_0 \end{bmatrix}$$

The transformation matrix  $A$  can be decomposed into two rotation matrix and one non-uniform scaling matrix as follows [38].

$$A = R_1 S R_2 \quad (4.23)$$

$$= \begin{pmatrix} \cos \alpha_{xx} & \cos \alpha_{xy} & \cos \alpha_{xz} \\ \cos \alpha_{yx} & \cos \alpha_{yy} & \cos \alpha_{yz} \\ \cos \alpha_{zx} & \cos \alpha_{zy} & \cos \alpha_{zz} \end{pmatrix} \times \begin{pmatrix} \delta_x & 0 & 0 \\ 0 & \delta_y & 0 \\ 0 & 0 & \delta_z \end{pmatrix} \times \begin{pmatrix} \cos \beta_{xx} & \cos \beta_{xy} & \cos \beta_{xz} \\ \cos \beta_{yx} & \cos \beta_{yy} & \cos \beta_{yz} \\ \cos \beta_{zx} & \cos \beta_{zy} & \cos \beta_{zz} \end{pmatrix}$$

where  $R_1$  and  $R_2$  are rotation matrices,  $S$  is the scale matrix.  $\alpha$  and  $\beta$  are the rotation angles of the first and third transforms, and  $\delta$  is the scale value of the second transform.

**Data:** Binary image

**Result:** Different moments generation

initialization;

**while** *not at end of the seed neighbour* **do**

    Get the current pixel value (*pixelVal*);

**if** *pixelValue* > 0 **then**

        get the physical space coordinate of the current index  
        (*pixelPoint*);

*pixelPoint*[0] = *pixelPoint*[0] -  $\bar{x}$ ;

*pixelPoint*[1] = *pixelPoint*[1] -  $\bar{y}$ ;

*pixelPoint*[2] = *pixelPoint*[2] -  $\bar{z}$ ;

$M_{000} + = \textit{pixelVal}$ ;

$M_{100} + = \textit{pixelPoint}[0] * \textit{pixelVal}$  ;

$M_{101} + = \textit{pixelPoint}[0] * \textit{pixelPoint}[2] * \textit{pixelVal}$ ;

$M_{010} + = \textit{pixelPoint}[1] * \textit{pixelVal}$ ;

$M_{001} + = \textit{pixelPoint}[2] * \textit{pixelVal}$ ;

$M_{111} + = \textit{pixelPoint}[0] * \textit{pixelPoint}[1] *$

$\textit{pixelPoint}[2] * \textit{pixelVal}$ ;

        :

$M_{301} + = \textit{pixelPoint}[0]^3 * \textit{pixelPoint}[2] * \textit{pixelVal}$ ;

$M_{310} + = \textit{pixelPoint}[0]^3 * \textit{pixelPoint}[1] * \textit{pixelVal}$ ;

$M_{130} + = \textit{pixelPoint}[0] * \textit{pixelPoint}[1]^3 * \textit{pixelVal}$ ;

$M_{031} + = \textit{pixelPoint}[1]^3 * \textit{pixelPoint}[2] * \textit{pixelVal}$ ;

        :

**else**

        Get the next pixel;

**end**

**end**

**Algorithm 2:** Moments algorithm

### 4.3 The Used Neural Network Architecture

Classification is a crucial step for many image-processing application where each unknown pattern is assigned to a category. Hence, after the feature extraction of the seed points is completed, we use an appropriate classifier to categorize the extracted features into one of the four classes. In the proposed thesis, we use an ANN classifier. Hence, the diagram of identification application is shown in Figure 4.6.

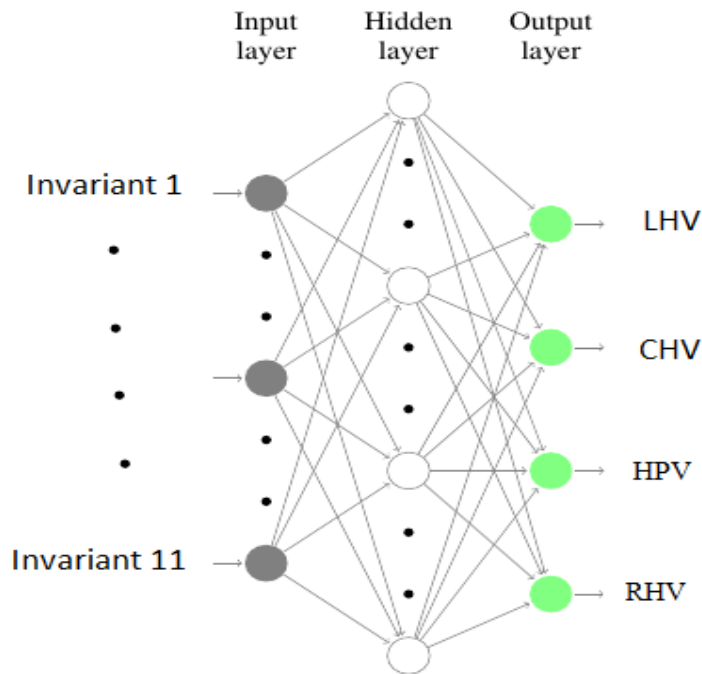


Figure 4.6: The used ANN model

Multi-layer Perceptron network is one of the neural classifiers that widely used today. MLP adjusts and optimizes the internal nodes with back propagation (BP) learning algorithm. Also, MLP classifier is a supervised neural network that contains various inputs, hidden layers, and multiple outputs [62]. In the proposed thesis, a single node is used for each feature in the input layer of the ANN model. Each feature represents the feature descriptor of the individual input seed point. The output layer has four neurons, which gives the patterns

of the four desired classes. Also, the proposed MLP model, the output pattern should reflect the corresponding pattern for the input data. For example, a high output value should be presented in the correct pattern node and a low output value for the other outputs. The MLP model starts with a random connection weights value for each node. Using these weights, the network calculates the outputs. The next step is to compare the outputs of the network with the desired output. The difference between the current output and the desired output is the error of the MLP network. Whenever that error is high, it can be reduced by using a back propagation technique. In back-propagation, the output nodes send feedback to the hidden layers about the network error. As a result, the hidden layers modify the connections weight to reduce the network error and produce new outputs to the output layer. The whole process is repeated until the desired output generates an acceptable network error.

MLP neuron node represented as:

$$y_i = f_i \left( \sum W_{ij} x_j \right) \quad (4.24)$$

where  $x_j$  represents the input data to the neural network,  $W_{ij}$  is the weights connection between the  $i^{th}$  neuron of the previous layer and  $j^{th}$  neuron of the current layer, and  $f_i$  is the activation function. We use the sigmoid function as an activation function.

We started by fifty-six seed points to test the system (fourteen points from each region). The neural network structure consists of 11 neurons (input features) at the input layer, 100 neurons in the hidden layer, and four neurons at the output layer. The output layer format is as follows: [1 0 0 0; 0 1 0 0; 0 0 1 0; 0 0 0 1]. Whereas, the output pattern [1 0 0 0] represents the occurrence of a point in the first region (the right hepatic vein). While the pattern [0 1 0 0] represents the occurrence of a point belonging to the second region (central

hepatic vein), the pattern [0 0 1 0] represents the occurrence of a point belonging to the third region (hepatic portal vein), and [0 0 0 1] pattern represents the occurrence a point belonging to the left hepatic vein.

To enhance the quality of the used neural network, we applied k-fold cross-validation technique. The benefits of using cross-validation are to choose the best set of the network parameters, such as the number of hidden layer, and to prevent the data over-fitting. The main concept of k-fold cross-validation is to split the input data into equal-sized sets ( $k$ ). Then,  $k - 1$  sets will be used for training and the remaining as the testing set. Also, each fold  $K$  contains an equal number of items from each of the input classes.

In the proposed thesis, we redesign the neural network by implementing the k-fold cross-validation. We choose  $k = 10$ , and we used the invariants data from 10 synthetic images to train the network, and each image has 56 feature points. Furthermore, we use 90% of the input data set for training and 10% for testing. The neural network is initially trained on the training set, and its weights are correctly updated. The validation test is used to compute the classification error using the weights resulting from the training. If the error is higher than a specific threshold, then the whole training-validation is repeated. Hence, in this research, we use 480 points for training the neural network, while 80 points are used for the testing purpose. Then, we used the pruning technique by reducing the number of hidden layer units, while keeping track of cross-validation performance. The new hidden layer units reduced to 18, while we have the same desire classifications. An appropriate scale has been selected to classify the sample input to ANN. The aim of the scale is to represent the input data to be in the range of 0 and 1. Hence, the following scale is used.

$$Scale = \sqrt{mean^2 + SD^2} \quad (4.25)$$

For each point, we get the moments invariants and calculate the mean and the standard deviation for each invariant of that point. Then, the input feature vector of each point of the training and the testing samples is divided by the scale in 4.25.

## 4.4 Level Set Segmentation

In this thesis, we propose a new method based on the shape detection method presented by Malladi [72] to segment the liver from MR images. Malladi method implemented the partial differential equations (PDE) to evaluate the boundary of the object. In PDE, progressive evaluation of the differences between neighboring pixels to find object boundaries is performed. The boundary of the object is detected when the algorithm of the PDE is converged where the differences of the neighboring pixels are the highest. The proposed method required three images as input to start the segmentation, an initial level set model, a feature image, and the surface patch image.

The classified seed points are used to create a level set seed image. To obtain that, we used fast marching technique [7] (see Figure 4.4). The first input used to initialize the level set in a form of image format where  $\phi(x, y, z, t) = 0$ . Where  $\phi$  is a level set function, and used to represent the distance of a point  $(x, y, z)$  to the boundary of an object. The distance has a positive if the point is inside the object boundary. Otherwise, it has a positive value. The second input is the feature image. Anisotropic diffusion filter is used to smooth the input image, the smoothed image passed to gradient magnitude filter, and then to sigmoid filter to generate the speed image. Lastly, the third input is the second-speed image that is generated to be as a surface that used as leakage blocker. The surface patch is formed by filling the exit vein of the liver where the leak is expected. The prior knowledge of the liver vessels is used to get the endpoint of these vessels. These points are used to build the required surface

patch. The next step is to fill the holes in the generated surface. Finally, the segmented model has a vessels structure. To fill the inside vessels of the generated model, we use the simple region growing algorithm with radius of 4 to fill these vessels. Input seeds from the vessels centerlines are used to guide the region growing process. Some tiny gaps are noticed between the inside structure of the segmented model and the filled vessels. As a post process, we use the median filter to fill any lifted gaps or spaces between the filled vessels using region growing and the segmented structure.

## 4.5 Results

The test images used in this thesis was obtained from human volunteer. High-quality dynamic MR image was acquired in the axial plane using a 1.5T GE scanner (GE Medical Systems, Milwaukee, WI). Image acquisition was performed using the LAVA gradient echo sequence with TR=3.79ms, TE=1.72ms, a flip angle of 12 degrees, the image matrix size of  $256 \times 256$ , in-plane pixel size of  $1.3 \text{ mm} \times 1.3 \text{ mm}$  and slice thickness of  $1.5 \text{ mm}$ . Note that, in image acquisition, TR (Repetition Time) represents the amount of time that exists between successive pulse sequences applied to the same slice. See also Repetition Time. While, TE (Echo Time) - represents the time in milliseconds between the application of the  $90^\circ$  pulse and the peak of the echo signal in Spin Echo and Inversion Recovery pulse sequences [73].

The invariant moments has been implemented using C++ code with ITK library. Table 4.1 shows the mean and standard deviation of invariant moments between synthetic images and their corresponded images that have been transformed by random rotation angles and scale values. In this thesis, we have generated 10 different images based on the affine transformation in Equation 4.22 and Equation 4.23. We selected 56 points in each image for training and testing the network. These points represent the bifurcation points of the vessels

centerlines of the liver. These points are distributed in the four regions of the liver. We tested the ANN with k-fold cross validation by using 18 neurons in the hidden layer with maximum error = 0.001. Table 4.2 shows the overall percentages of correct classification. As noted from the table, we have obtained an overall accuracy equals to 98%. For unseen images, the overall testing accuracy equals 95.05%, (see Table 4.3).

Table 4.1: Mean and standard deviation of the generated moments

Invariant#	Region1		Region2		Region3		Region4	
	$m$	$\sigma$	$m$	$\sigma$	$m$	$\sigma$	$m$	$\sigma$
$I_{22}^2$	0.3220	0.0030	0.0254	0.0090	0.6097	0.1057	0.8197	0.0087
$I_{222}^2$	-0.014	0.0185	-0.0171	0.0198	-0.0121	0.0070	-0.713	0.0029
$I_{33}^3$	98629	0.0060	74183	0.0059	62835	0.0012	44235	0.0038
$I_{11}^3$	0.0152	0.0002	0.0472	0.0006	0.0128	0.0085	0.0928	0.0086
$I_{233}^{23}$	0.0159	0.0098	0.0108	0.0005	0.0564	0.0094	0.0464	0.0009
$I_{123}^{23}$	0.0244	0.0002	0.0131	0.0003	0.0223	0.0039	0.0223	0.0027
$I_{112}^{23}$	0.0019	0.0083	0.0005	0.0009	0.0019	0.0018	0.0027	0.0036
$I_{3333}^3$	0.025	0.0004	0.0372	0.0008	0.0728	0.0095	0.0428	0.0592
$I_{1333}^3$	0.0159	0.0039	0.0408	0.0009	0.0764	0.0029	0.0864	0.0037
$I_{1133}^3$	-0.014	0.0025	-0.0131	0.0076	-0.0021	0.0009	-0.213	0.0035
$I_{1113}^3$	0.005	0.0060	0.0472	0.0025	0.0028	0.0385	0.0727	0.0035

Description	Results
Overall testing accuracy	98%

Table 4.2: Overall accuracy of the synthesized images

Description	Results
Overall testing accuracy	95.6%

Table 4.3: Overall accuracy of the unseen images

To illustrate the robustness of the proposed method, we evaluated the algorithm using noval images. These images are from the same subject but acquired

in a different positions. We calculate the moments by using 56 points from the first image, and we calculate the matched points from the other image. The points are distributed on the four regions of the liver image. Then, we calculate the ratio by dividing each invariant obtained from an image by the corresponding invariant of a transformed image from the same volunteer. Next, we obtained the mean, and the variance of the four regions; left hepatic vein, center hepatic vein, hepatic portal vein, and right hepatic vein as shown in Table 4.4. Lastly, we test the classified seed points by using them to initialize the segmentation method we proposed earlier.

Figure 4.7 represents the complete pipeline of the proposed method with an MR abdominal image as the input and a segmented liver image as the output. While Figure 4.8 shows the liver after segmentation with the seed point used to initialize the segmentation in that region. To evaluate the quality of our proposed segmentation approach, we use a robust accuracy technique to estimate the segmentation accuracy relative to the ground truth [36]. In Volumetric overlap error we use  $G$  and  $S$  to denote the set of points of the ground truth segment and the computed segment respectively. The value is 1 for a perfect segmentation, and a value of 0 denotes to a completely failed one.

$$E_D = 2|S \cap G|/(|S|+|G|) \quad (4.26)$$

The ground truth model is obtained by segmenting the liver slice by slice manually using 3DSlicer [4]. The Volumetric Overlap Error (VOE) of the proposed method compared with a ground truth model is 84.37%. While the VOE of a manual seed selection method [1] was 80%.

Table 4.4: The moment invariants ratio, mean, standard deviation of unseen images

Invariant#	Region1		Region2		Region3		Region4	
	$m$	$\sigma$	$m$	$\sigma$	$m$	$\sigma$	$m$	$\sigma$
1	0.3897	0.0041	0.0298	0.0309	0.6285	0.3095	0.8364	0.3587
2	-0.1656	0.0265	-0.0183	0.0508	-0.0301	0.0017	-0.625	0.0037
3	68629	0.0080	74137	0.0080	62950	0.0030	44481	0.0068
4	0.0252	0.0005	0.0428	0.0009	0.0301	0.0095	0.1028	0.0109
5	0.0120	0.0548	0.0142	0.0008	0.0480	0.0089	0.0554	0.0029
6	0.1090	0.0004	0.0159	0.0005	0.0309	0.0080	0.0257	0.0050
7	0.0108	0.0263	0.0048	0.0010	0.0025	0.0038	0.0040	0.0067
8	0.0451	0.0005	0.0338	0.0098	0.0798	0.0302	0.0492	0.0802
9	0.0284	0.0064	0.0413	0.0018	0.0781	0.0037	0.0887	0.0058
1	0-0.0284	0.0039	-0.0138	0.0986	-0.0038	0.0090	-0.251	0.0045
11	0.0149	0.0078	0.0425	0.0039	0.0048	0.0619	0.0809	0.0098

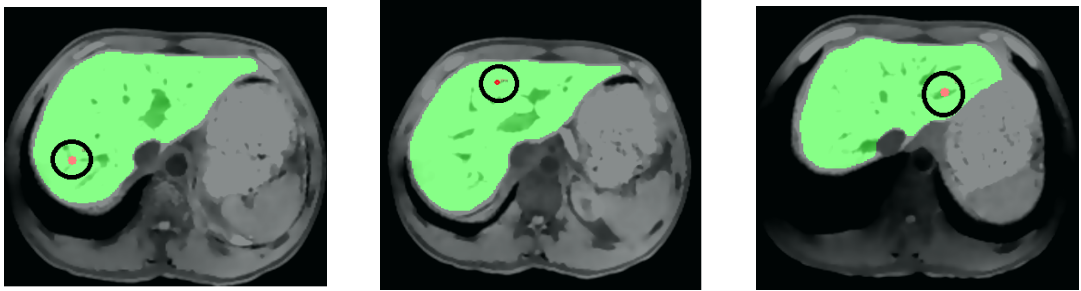


Figure 4.8: (a) A seed point (Red) in the center region, (b): a seed point (Red) in the right region, (c): a seed point (Red) in the left region

## 4.6 Summary

Magnetic resonance imaging and computed tomography are used in diagnosis, surgeries, and treatment procedures of tumors and malignancies throughout the world. Accurate image segmentation of MR/CT images is a crucial step in many treatment and diagnosis procedures. The difficulties of the segmentation process for the liver are due to the location and texture of the liver. Furthermore, liver is surrounded by organs such as the heart, stomach, and kidneys. These organs have the similar intensity as the liver; as a result, there is an overlap of intensity of the liver and these organs adding more challenges to the segmenta-

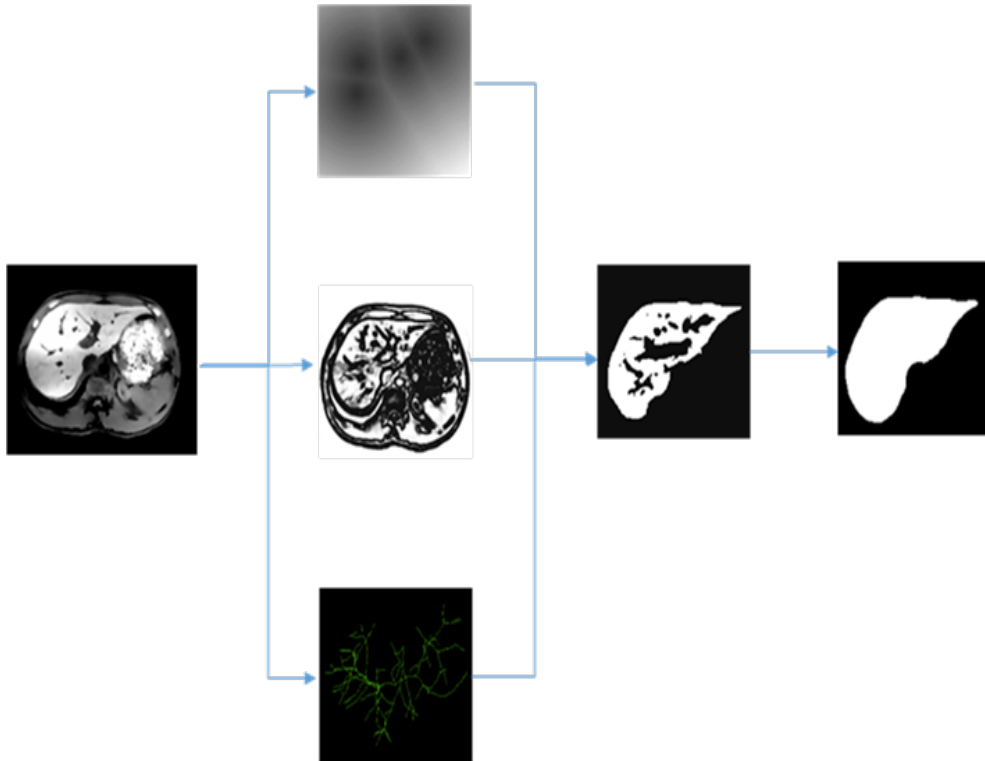


Figure 4.7: The proposed classification system pipeline with input and output images

tion process. Region based segmentation is initialized by selecting seed points in the region of interest. The resulting segmentation accuracy depends on the location of these points. In addition, the manual selection of those points for the same subject is considered time consuming and tedious work. Furthermore, it could lead to inaccuracies due to the differences between the MR images acquired from the same subject, i.e. different in the subject positioning or at different respiratory instance.

In this thesis, we adopt the moment invariants used for shape detection to work for 3D seed points in MR abdominal images. The moments are invariant to affine transformation. We have demonstrated the effectiveness of our technique using the classified seed points to segment liver from abdominal MR images. The proposed technique has an accuracy of 84.37% compared to manual seed point selection which has an accuracy of 80%. The results show that our method outperforms the manual method in terms of correct segmenta-

tion. Further work will segment more MR images using the proposed technique.

In this thesis, the data from a single subject was used to train the ANN, and we have not tested it on other patients. Training the ANN on the data from multiple patients would extend the range of this technique if it does not impact the recognition rate significantly. This is an important area for future work.

# Chapter 5

## Vessel-Based Fast Deformable Registration with Minimal Strain Energy

Image registration for internal organs and soft tissues is considered extremely challenging due to organ shifts and tissue deformation caused by patients movements such as respiration and repositioning. In this research, we propose a fast deformable image registration method. The purpose of our work is to greatly improve the registration time while maintaining the registration accuracy.

In this research, we formulate the deformable image registration problem as a quadratic optimization problem that minimizes strain energy subject to the constraints of 3D curves of blood vessel centerlines and point marks. The proposed method does not require iteration and is local minimum free. By using 2nd order B-splines to model the blood vessels in the moving image and a new transformation model, our method provides a closed-form solution that imitates the manner in which physical soft tissues deform, thus guarantees a physically consistent match. We have demonstrated the effectiveness of our deformable technique in registering MR images of the liver. Validation results show that we can achieve a Target Registration Error (TRE) of 1.29 *mm* and an average Centerline Distance Error (CDE) of  $0.84 \pm 0.55$  *mm*.

This technique has the potential to significantly improve registration capabilities and the quality of intra-operative image guidance. To the best of our knowledge, this is the first time that a global analytical solution has been

determined for the registration energy function with 3D curve constraints.

## 5.1 Introduction

In order to guide therapeutic procedures and achieve more accurate diagnosis of diseases, it is often helpful to fuse together multiple images of soft tissues from different sources. To this end, the fast deformable registration of soft tissues finds many applications. Deformable registration techniques can be used to register the original images with follow-up images therefore providing more accurate information for diagnosis [8], [68], [91]. It can also be employed during therapeutic procedures in order to align the proper treatment plan to the patient [35], [45]. Although image registration for mostly rigid structures such as the bone and brain is normally a manageable task, it is much more challenging to align images of soft tissues when we need to deal with organ shifts and the deformation of soft tissues caused by respiration, heartbeats, patient repositioning, and/or surgical treatment. Currently, deformable registration is still a time-consuming process, for example, deformable registration of liver images takes 38 minutes on average [19]. In the case of liver surgery, Lange *et al.* reported that registration accuracy in the range of 3 *mm* with a manual interaction time of about 10 minutes is reasonable for clinical application [80]. During radiotherapy treatment, it is highly desirable to achieve an image registration accuracy of better than 3 *mm* at the treatment target [63]. Based on these studies, we conclude that in order for the image guidance to be effective, the registration error between MR images of the liver should be controlled to be less than 3.0 *mm* and the registration time to be less than 10 minutes.

Most feature-based registration or intensity-based registration techniques [8], [68], [11] [17] [39] utilize iterative methods to achieve the optimal alignment of two images. The limitations associated with iterative methods generally include a slow convergence speed and possible local minima. When the starting

point is close to a local minimum, the iterative method may be trapped in the local minimum and cannot guarantee a correct registration result. Compared with the iterative methods, analytical solutions are generally much faster and can achieve optimal solutions.

Davis *et al.* [53] proposed an elastic body spline (EBS) method based on elastic solid mechanics, which conforms to the physical model of the Navier-Cauchy equilibrium equation. Their method can reach an analytical solution. However, the EBS generally requires a specific polynomial i.e. radically symmetric force field, which does not necessarily reflect the real force field applied to the soft tissues in clinical practice. Moreover, their analytical solutions are only applicable to point-based registration procedures and cannot deal with the constraints associated with 3D curves such as blood vessel centerlines. In practice, reliably identifiable landmarks are often limited in soft tissues of real patients and are time-consuming to identify. On the other hand, blood vessels are often more abundant and can be extracted more easily and reliably in many organs such as the liver, brain, lungs and kidneys. These vessels are good features and can provide reliable constraints to anchor deformable registration. Generally, EBS results in less accurate registration results due to the limited number of corresponding landmarks reliably identified in two images.

Another popular deformable registration approach is the Thin-plate Spline (TPS) which has originally been developed for surface interpolation [41], [22], [18]. The TPS method is based on a physical model of a thin metal plate. The 3D version of the TPS is a mathematical extension of the 2D TPS, which does not correspond to any physical model [53]. In other words, the results of the 3D TPS would be different from those obtained via a physics-based EBS. The 3D TPS has been employed to register ultrasound and MR images of the brain using landmarks [23] or blood vessels [35]. In the work of Reinertsen *et al.* [35], the

3D TPS is employed as only one step within the iterative close point method. Although they used blood vessels for image registration, the blood vessels were subsampled and corresponding points for registration were obtained by a point matching step. In essence, they still used point based registration instead of direct vessel based registration. The registration needs nearly a minute to finish.

In this research, we present a new deformable registration method to align liver images by using the constraints of 3D curves of blood vessels. We formulate the deformable registration problem as an optimization problem. The registration energy function is constructed to be a quadratic form of the deformable transformation parameters. The analytical solution to the optimization problem guarantees a global, local-minimum-free optimal solution. Besides, our method not only minimizes the distance errors of vessel curves, but also simultaneously minimizes the strain energy associated with the deformation, which thus leads to optimal physically consistent deformation. Physical consistency can prevent the occurrence of non-smoothness, singularity and folding phenomena, and ensure a correct registration solution. To the best of our knowledge, our method is the first time to derive an analytical solution to the deformable registration problem with 3D curve constraints. Sample sets of MR images of the liver were used to evaluate the performance of the proposed registration approach. In this study, we will focus on registration of liver images, however, there are similar challenges with other abdominal organs [17], [47], [52], and the proposed methods can be applied to those cases as well. A preliminary version of part of this work has been reported in [88].

## 5.2 Materials and Methods

### 5.2.1 Physics-Based Registration Methodology

In this research, we apply multiple techniques to address the challenges in the deformable registration of two images. Our registration methodology is based on linear elastic solid mechanics and the minimum strain energy principle. We aim to minimize the following registration energy function:

$$J(p) = w_e E_e(T(x, p)) + w_c E_c(T(x, p)) \quad (5.1)$$

where  $T(x, p)$  is a deformable transformation model and  $p$  the corresponding transformation parameters. This energy function measures the quality of alignment between the fixed image and the moving image, and consists of two terms.  $E_e(T)$  is the strain energy produced by the deformation of soft tissues. Minimization of strain energy yields physically consistent deformation. Besides, the inclusion of the strain energy provides good generalization properties. We choose to use the strain energy because the strain energy can capture the locally linear deformation which dominates the deformation of the soft tissues in our study. The curve energy term  $E_c(T)$  penalizes the distance error between pairs of corresponding 3D curves (i.e. blood vessel centerlines) extracted from the fixed and moving images, which ensures that the resulting optimal deformation should align internal vessel structures. Weights  $w_i$  are used to adjust the relative effects of each term. Therefore, combinations of the above energy terms provides different mechanisms to constrain the final registration solution to a physically consistent deformable match. In this research, we derive a novel fast analytical global solution to Problem 5.1 through specific design of different registration components.

The rationale of our proposed method is to formulate the deformable registration problem 5.1 as a quadratic optimization problem, that is, to transfer

the registration energy function 5.1 to a quadratic function of transformation parameters  $p$  by the design of different components as follows:

$$J(p) = C_0 + C_1^T p + \frac{1}{2} p^T C_2 p \quad (5.2)$$

where  $C_1$  is a  $N_p$  vector,  $C_2$  a  $N_p \times N_p$  matrix, and  $N_p$  the number of transformation parameters ( $p$ ). Constants  $C_1$  and  $C_2$  are calculated based on the constraints of the 3D curves and strain energy (see Sections 5.2.2 and 5.2.3 for details). Thus we are able to find a closed-form optimal registration. The optimal solution can be analytically obtained by solving the following system of linear equations,

$$\frac{\partial J(p)}{\partial p} = C_1 + C_2 p = 0. \quad (5.3)$$

The global optimal solution is calculated by  $p = -C_2^{-1} C_1$ . Furthermore, as it is well known, there is no local minimum in the quadratic optimization problem.

In order to achieve a quadratic form of the registration energy function, we propose the following novel techniques to deal with the energy terms and the transformation model. First, we employ a local affine transformation model [65] This model is nonlinear with respect to spatial point  $x$ , but is linear with respect to transformation parameters  $p$ , which leads to the quadratic form of strain energy. Second, we devise a new method to analytically calculate the shortest distance between 3D curves and its derivative with respect to transformation parameters  $p$  by employing the 2nd-order B-Spline to represent 3D curves (i.e. vessel centerlines). Therefore, we convert the curve distance energy term into a quadratic form of transformation parameters as well.

In the following sections, we discuss the different components in detail on how to derive the quadratic formula for each energy term.

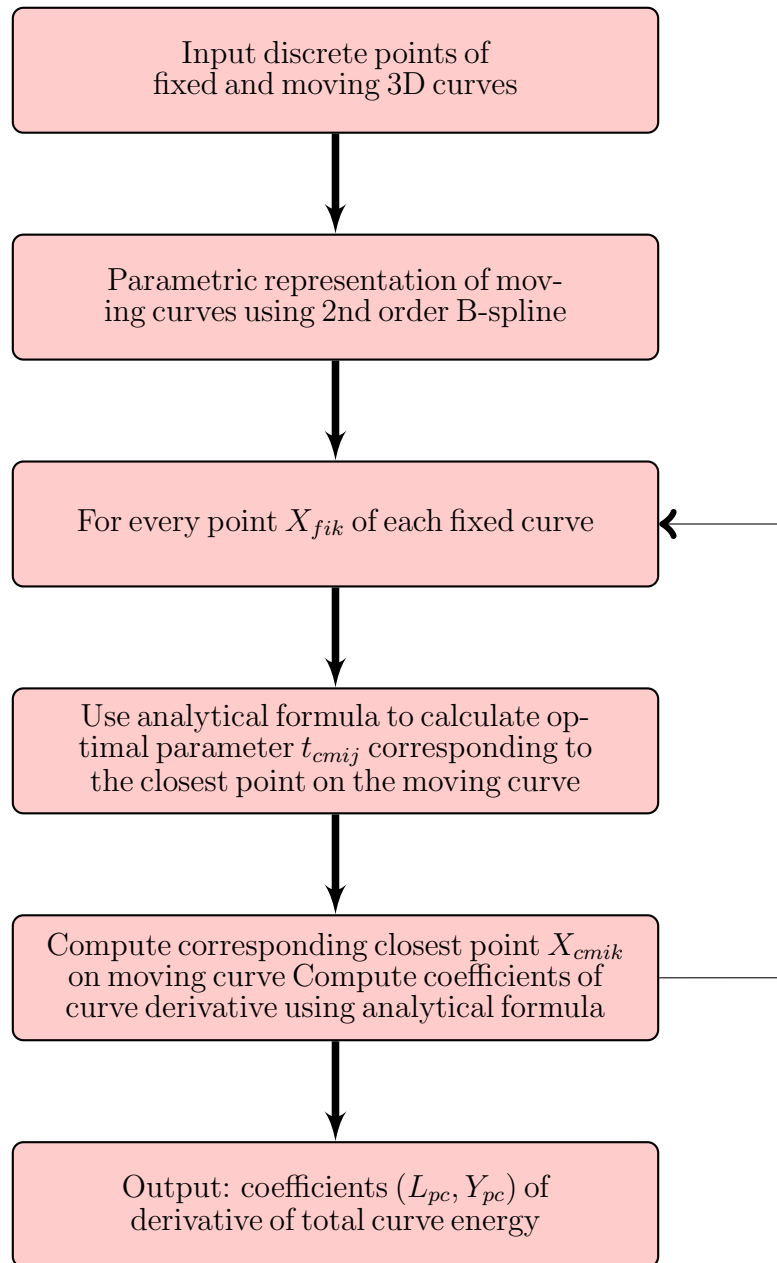


Figure 5.1: Schematic of analytically computing curve energy and its derivative

### 5.2.2 Curve Energy

In this section, we propose a novel technique to analytically calculate the curve energy, i.e. the shortest distance between pairs of 3D curves, and its derivative with respect to transformation parameter  $p$ . Specifically, this is achieved by analytically computing the shortest distance from a given point of the curve in the fixed image to the corresponding 3D curve in the moving image and its derivative with respect to transformation parameters through a parametric representation of 3D curves. Fig. 5.1 shows the schematic of computing curve energy and its derivative.

#### 3D Curve Representation Using B-Spline

The centerlines of blood vessels are extracted from MR liver images in the form of discrete points. In order to effectively employ these 3D curves as constraints in image registration, we need a continuous and smooth representation of vessel curves in the moving image space. In this research, we express vessel centerlines as parametric 3D curves using the 2nd-order B-Spline. This representation leads to an analytical solution to the closest point on the curve given a transformed point of fixed curves. Note that we only need a continuous representation for centerlines in the moving image, but not for those in the fixed image.

The  $i^{th}$  vessel centerline in the moving image  $C_{mi}(t)$  is represented as three 1D parametric B-Spline curves.

$$\begin{aligned}
 C_{mi}(t) &= \left[ C_{mix}(t) \ C_{miy}(t) \ C_{miz}(t) \right]^T, t \in \left[ t_k, t_{k+1} \right], \\
 C_{mix}(t) &= C_{mixk_2}t^2 + C_{mixk_1}t + C_{mixk_0} \\
 C_{miy}(t) &= C_{miyk_2}t^2 + C_{miyk_1}t + C_{miyk_0} \\
 C_{miz}(t) &= C_{mizk_2}t^2 + C_{mizk_1}t + C_{mizk_0} \\
 k &= 0, 1, \dots, N_{mi} - 1
 \end{aligned} \tag{5.4}$$

where  $t$  is the parameter, which can be selected to represent the curve length between current coordinates  $C_{mi}(t)$  and the starting point of the vessel,  $N_{mi}$  is the number of discrete points on the  $i^{th}$  vessel centerline extracted from MR images,  $C_{mi*k_2}, C_{mi*k_1}, C_{mi*k_0}$  are constants for the  $i^{th}$  curve.

### Curve Energy and its Derivative

Vessel centerlines are able to provide reliable constraints for internal structures of soft organs during the image matching process. In this research, we aim to minimize the distance between pairs of corresponding vessel centerlines, which is formulated as the following minimization problem:

$$E_c(p) = \sum_{i=1}^{N_c} \sum_{k=1}^{N_{ci}} \frac{1}{2} \left\| T(X_{fik}) - C_{mi}(t) \right\|^2 \quad (5.5)$$

where  $N_C$  is the total number of vessel centerlines,  $N_{C_i}$  the number of discrete points on the  $i^{th}$  centerline from the fixed image,  $X_{fik}$ ,  $i = 1, 2, \dots, N_{C_i}$ , is the  $k - th$  discrete point on the  $i^{th}$  centerline from the fixed image,  $C_{mi}(t)$  the continuous parametric B-Spline representation of the  $i^{th}$  vessel centerline from the moving image. For simplicity we limit our discussion to finding the closest point on a 3D curve in the moving image for a transformed point of the fixed image.

Based on calculus, the derivative of  $E_c$  can be calculated by the following analytical formula (see Appendix A for the detailed derivation),

$$\frac{\partial E_c(p)}{\partial p} = L_{pc}p - Y_{pc} \quad (5.6)$$

where

$$\begin{aligned}
L_{pc} &= \sum_{i=1}^{N_c} \sum_{k=1}^{N_{ci}} \left\{ A_p(X_{fik}) D_{cmik}^T A_p^T(X_{fik}) \right\} \\
Y_{pc} &= \sum_{i=1}^{N_c} \sum_{k=1}^{N_{ci}} \left\{ A_p(X_{fik}) D_{cmik}^T (X_{cmik} - B_p(X_{fik})) \right\}
\end{aligned} \tag{5.7}$$

From 5.6, we note that  $(\frac{\partial E_c(p)}{\partial p})$  is a linear function of transformation parameters  $p$ . This implies that the shortest distance between curves  $E_c(p)$  is a quadratic function of transformation parameters  $p$ .

### 5.2.3 Strain Energy

Minimization of strain energy tries to imitate the manner in which physical soft tissues naturally deform, and leads to physically consistent deformable registration results. Strain energy is generated by the deformation of soft tissues based on elastic solid mechanics, and can be calculated as follows according to the Saint-Venant model [69], [20]:

$$E_e = \int \int \int \left\{ \frac{\lambda}{2} [tr(E)]^2 + \mu \cdot tr(E^2) \right\} dx dy dz \tag{5.8}$$

$$E = \begin{bmatrix} e_{11} & e_{12} & e_{13} \\ e_{21} & e_{22} & e_{23} \\ e_{31} & e_{32} & e_{33} \end{bmatrix}$$

$$e_{ij} \approx \frac{1}{2} \left[ \frac{\partial T_i}{\partial x_j} + \frac{\partial T_j}{\partial x_i} - 2\delta_{ij} \right], \tag{5.9}$$

$$\delta_{ij} = \begin{cases} 1, & \text{if } i=j; \\ 0, & \text{otherwise.} \end{cases}$$

where  $\lambda$  and  $\mu$  are elastic parameters of soft tissues,  $E$  is a strain tensor represented as a 3x3 symmetric matrix,  $tr(E) = e_{11} + e_{22} + e_{33}$  the trace of matrix  $E$ , and  $T_{NF_i}$  the  $i^{th}$  component of  $T_{NF}(x)$ .

Using a locally affine transformation model [65], we write the strain energy as a quadratic function of the transformation parameters  $p$  in the following formula:

$$E_e(p) = C_{e0} + C_{e1}^T p + \frac{1}{2} p^T C_{e2} p \quad (5.10)$$

where  $p$  is the transformation parameters, and constants can be calculated offline in advance based on the pre-treatment fixed image and region parameters.

The explicit derivative of strain energy with respect to the transformation parameters is calculated analytically as follows:

$$\frac{\partial E_e(p)}{\partial p} = C_{e1} + 2C_{e2}p. \quad (5.11)$$

In summary, based on equations 5.3, 5.6 and 5.11, we compute the derivative of the registration energy function 5.1 with respect to transformation parameters  $p$  as follows:

$$\frac{\partial J(p)}{\partial p} = w_e \frac{\partial E_e}{\partial p} + w_c \frac{\partial E_c}{\partial p}. \quad (5.12)$$

We note that each term in the above equation is linear with respect to transformation parameters  $p$ , thus we are able to compute the coefficients and in equation 5.3 and the global optimal transformation parameters  $p$  can be calculated in a closed-form.

## 5.2.4 Evaluation Methods

Ideally, non-rigid registration accuracy is evaluated by comparing the deformation obtained from the registration with the ground truth deformation of soft tissues in the region of interest (ROI). However, in clinical practice, a ground truth or gold standard is not readily available especially for in vivo human subjects. As a result, many papers evaluate the registration accuracy by calculating the mismatch of natural landmarks in the two images after registration [17], [37]. Since the number of reliably identified natural anatomical landmarks such as branch points of vessels in the liver images is limited, this evaluation can only render an accurate assessment in the neighborhood of the landmarks. We have noticed that blood vessels are abundant in many organs such the liver and cover a much larger region than the natural landmarks. Therefore, the residual average centerline distance (ACD) of corresponding vessel centerlines after registration can provide complementary information to assess the accuracy of non-rigid registration [92].

Based on the above analysis, we utilize two accuracy measures in this study, i.e. TRE and ACD, to evaluate the performance of the proposed registration method. TRE calculates the mismatch of natural landmarks in the two images after registration. Once natural landmarks are reliably identified in two images, TRE is an accurate measure for the neighborhood of the landmarks. ACD calculates the average centerline distance error. TRE and ACD are conventionally adopted to measure the registration performance [37], [92].

## 5.3 Registration Accuracy Measures: TRE/ACD

### 5.3.1 Landmark-Based Target Registration Errors (TRE)

In this landmark-based validation, landmarks (targets) were defined as the branch points of blood vessels and were identified in both MR images. The

resulting registration transformations were applied to these landmarks in one image; TREs were then calculated in the same coordinate system. Specifically, the TRE is expressed as the root mean square (rms) of the distances between the landmarks in the fixed MR image after registration and the corresponding homologous landmarks in the moving MR image as follows [37].

$$TRE = \frac{1}{N} \sum_{i=1}^N \left\| T(x_{Fi}) - x_{Mi} \right\| \quad (5.13)$$

where  $(x_{Fi}, x_{Mi})$  are the corresponding landmarks in the fixed and moving images, respectively,  $N$  the number of landmarks, and  $T(x)$  the resulting registration transformation.

### 5.3.2 Average Vessel Centerline Distance (ACD)

Blood vessel centerlines were extracted from both fixed and moving images. We employed the resulting transformation to transform the centerlines from the fixed image into the moving image space, and then calculated the average centerline distance between the pairs of corresponding centerlines as follows [92].

$$ACD = \frac{1}{N} \sum_{i=1}^N \sum_{k=1}^{N_{ci}} \left\| T(x_{Fik}) - C_{Mi}(t_{cik}) \right\| \quad (5.14)$$

where  $x_{Fik}$ 's are discrete points on the  $i^{th}$  centerline in the fixed image,  $C_{Mi}(t_{cik})$  the closest point on the  $i^{th}$  centerline in the moving image from the transformed point  $T(x_{Fik})$ , and  $T(x)$  the resulting registration transformation.

## 5.4 Image Processing for Evaluating Registration Accuracy

### 5.4.1 Image Preprocessing

In the original raw MR images, blood vessels are portrayed as black. First, we negated images by inverting the image intensity in order to obtain bright blood vessels for further image processing. Then, a vessel enhancement filter from the 3D Slicer module VMTKVesselEnhancement [4], [48] was employed to enhance vessel structures, which was followed by a threshold filter to remove background noise and small vessels. These preprocessed images were then used for the extraction of the centerlines of blood vessels.

### 5.4.2 Centerline Extraction

First, a level set based segmentation method was used to segment blood vessels using Slicer Module VMTKEasyLevelSetSegmentation [48]. Then after source seed points and target points were manually specified, centerlines were extracted by using the Slicer VMTK centerline extraction module [48], as shown in Fig. 5.2.

### 5.4.3 Localization of Branch Points

Based on the extracted vessel centerlines, branch points were automatically calculated using the in-house custom software. Then the correspondences of the branch points were manually established by visually inspecting vessel centerlines and branch points using 3D Slicer [4].

## 5.5 Results

In this section, we present the registration results of the proposed method, and conduct a comparative study with rigid and Elastic Body Spline (EBS) reg-



Figure 5.2: Extracted vessel centerlines within the liver surface

istrations of the liver MR images. We have applied the proposed deformable registration method to the MR images of the liver of human subjects.

**Liver image acquisition:** Liver images used in this research were acquired from human volunteers. High-quality MR images were acquired in the axial plane using a 1.5T GE scanner (GE Medical Systems, Milwaukee, WI). Image acquisition was performed using the LAVA gradient echo sequence with  $TR=3.79\text{ ms}$ ,  $TE=1.72\text{ms}$ , a flip angle of 12 degrees, an image matrix size of  $256 \times 256$ , in-plane pixel size of  $1.3\text{ mm} \times 1.3\text{ mm}$  and slice thickness of  $1.5\text{ mm}$ . Image sets were acquired with a breath-hold at different positions. Note that, in image acquisition, TR (Repetition Time) represents the amount of time that exists between successive pulse sequences applied to the same slice. See also Repetition Time. While, TE (Echo Time) - represents the time in milliseconds between the application of the  $90^\circ$  pulse and the peak of the echo signal in Spin Echo and Inversion Recovery pulse sequences [73].

In this research, we have extracted blood vessels (i.e. portal veins and hepatic veins) and branch points from both MR images of the liver. After the proposed method was employed to register the two MR images of the liver, Fig.

5.3 shows the image overlay before and after image registration, and Fig. 5.4 shows the overlay of the matched vessel centerlines of the liver.

These results demonstrate that the centerlines and images are matched correctly using the proposed deformable registration method. The algorithm was written in *C++* and ran on a computer running Microsoft Windows 7 with a Core 2 Quad 2.6 GHz Intel processor and 4 GB of memory. The average registration run-time was less than one second.

### 5.5.1 Quantitative Registration Accuracy

To quantitatively evaluate the performance of the proposed registration method, we calculate two accuracy metrics: TRE and ACD for the registered MR images of the liver as shown in 5.5. The proposed method Neuro-fuzzy Strain (NFS) is employed to register the MR images of the liver. Rigid registration is also performed for the purpose of comparison. Before registration, the overall average displacement between two images is 8.84 *mm* in terms of the distance between the corresponding branch points,  $6.63 \pm 3.15$  *mm* in terms of average vessels distances. Rigid registration reduces the residual alignment errors to a TRE of 6.24 *mm*, and an ACD of  $4.65 \pm 2.61$  *mm*. However, there is still significant deformation left after rigid registration and it fails to achieve acceptable accuracy. Our proposed deformable registration method can achieve a TRE of 1.29 *mm* and an ACD of  $0.84 \pm 0.55$  *mm*, which is significantly better than rigid registration.

Table 5.5: Registration accuracy of liver images (UNIT: MM)

Method	TRE	ACD(mean $\pm$ SD)
Before Registration	8.84	$6.63 \pm 3.15$
Rigid Registration	6.24	$4.65 \pm 2.61$
NFS Registration	1.29	$0.84 \pm 0.55$

### 5.5.2 Comparison with EBS

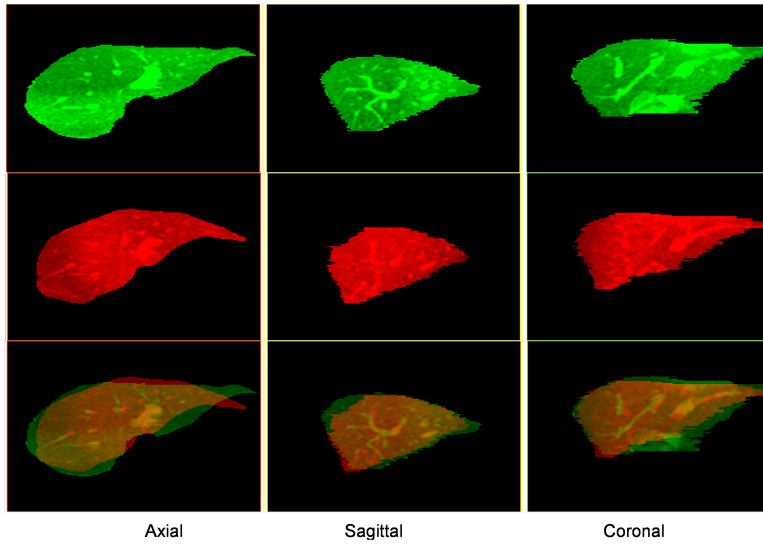
Based on a physical model of 3D elastic body deformation, the elastic body spline (EBS) was introduced to register two corresponding sets of homologous points [53]. The EBS is a linear combination of translated versions of the analytic solutions of the Navier equation (for further details see [53]):

$$d(x) = \sum_{i=1}^N G(x - p_i)c_i + Ax + b$$

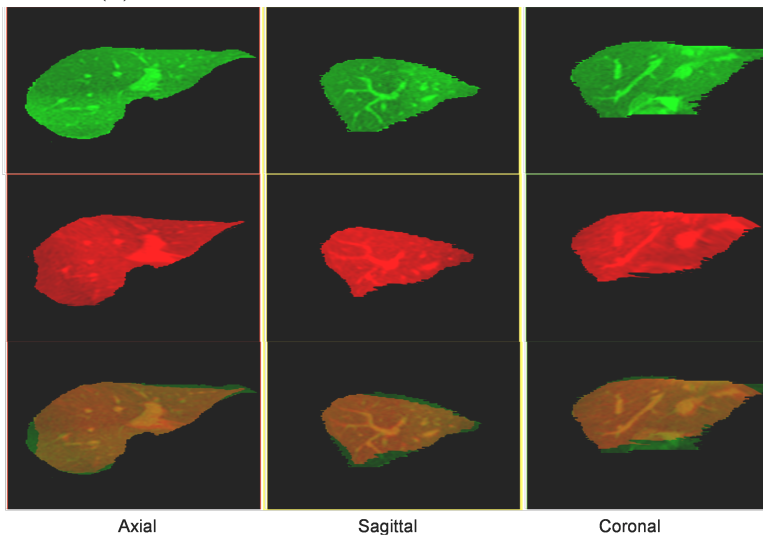
$$G(x) = (12(v - 1) - 1)r^3I - 3rxx^T, \quad r(x) = \sqrt{x_1^2 + x_2^2 + x_3^2}$$

where  $d(x)$  is the displacement at 3D point  $x$ ,  $G(x)$  is a 3x3 matrix - the basis function of EBS,  $v$  denotes Poissons ratio,  $I$  is a 3x3 identity matrix,  $c_i$  is the 3x1 force vector that determines the force direction and magnitude at point  $p_i$  (corresponding to the force field  $f_i(x) = c_i||x - p_i||$  centered at  $p_i$ ),  $N$  is the total number of force fields  $f_i(x)$  that are applied to the elastic body,  $Ax + b$  is the affine portion of the EBS. The coefficients  $A, b, c_i$  are determined by solving a linear system of equations resulting from the interpolation conditions:  $d(p_i) = d_i$ , displacement at  $p_i$ . This EBS is employed to register corresponding two point sets.

In this experiment, fifty-one marks were employed for the EBS registration. The resulting registration accuracy is shown in Table 5.6. All landmarks are matched well since the EBS should exactly match at marks and performs the interpolation at other points as expected. In terms of the ACD, the proposed method outperforms the EBS.



(a) Before registration, vessels are not aligned



(b) After registration, vessels are matched well

Figure 5.3: Overlay of images before and after registration. In each plot, first row: three orthogonal slices of 3D MR fixed image, 2nd row: three orthogonal slices of 3D MR moving image before or after registration, 3rd row: overlay of two images; left column: axial view, middle column: sagittal view, and right column: coronal view. Note that the overlay of bright green and bright red vessels is yellow, internal vessels are correctly matched after registration

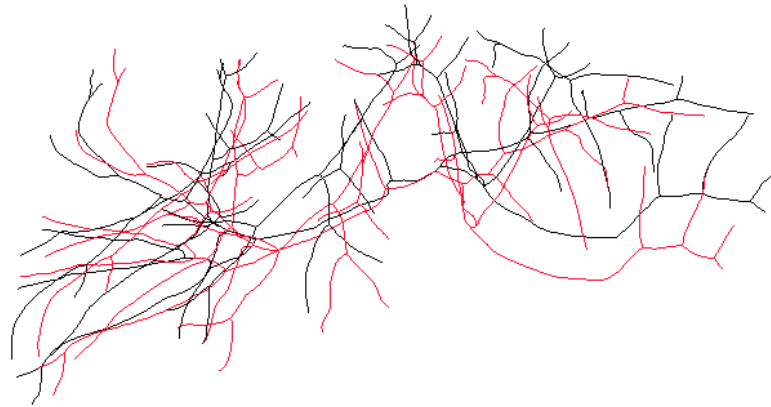
Table 5.6: Registration accuracy with EBS (UNIT: MM)

Method	TRE	ACD(mean $\pm$ SD)
NFS Registration	1.29	0.84 $\pm$ 0.55
EBS Registration	0.0075	1.02 $\pm$ 1.07

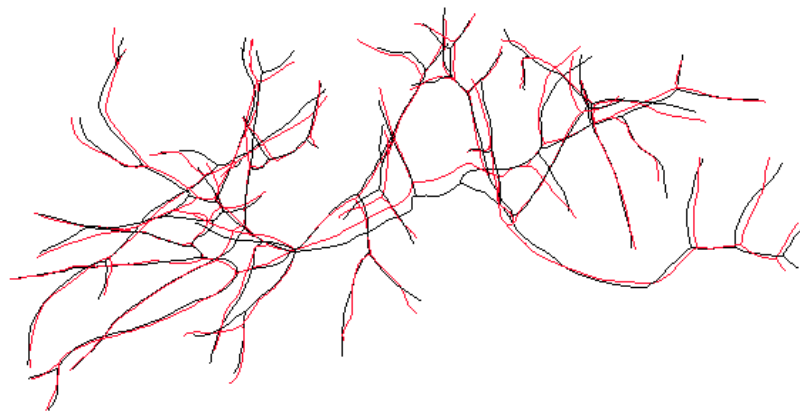
## 5.6 Summary

In this research, we assume that the vessels in the liver images have already been extracted and the correspondences between the two sets of vessels are known. This can be achieved by using a joint segmentation and registration framework proposed in our previous work [88]. In that research, we proposed a method to automatically segment the vessels and provided the correspondences between two vessel trees. In this research, we only concentrate on developing and validating the new fast registration algorithm. In the future, we will investigate and thoroughly evaluate the overall accuracy for the whole joint segmentation and registration framework

Since 3D curves or blood vessels represent dominant features in many internal organs, our approach allows for the accurate matching of images rapidly. Based on the linear elastic solid theory, the strain energy, instead of the bending energy, is included as part of our energy function so that our optimization problem takes on a clear physical meaning. As a result, our closed-form solution is a global optimal transformation that imitates the manner in which physical soft tissues naturally deform. The proposed method can be applied in numerous clinical practices ranging from peri-operative image registration processes to proper diagnosis in follow-up medical visits. Although MR images of the liver are used in our validation process, our method can be effectively applied when registering any type of 3D images with blood vessels which depict physical soft



(a) Before registration



(b) After registration

Figure 5.4: Overlay of vessel centerlines (a) before registration and (b) after registration, black lines from the fixed image, and red lines from the moving image

tissues in different imaging modalities.

# Chapter 6

## Deformable Image Registration for Tissues with Large Displacement

Image registration for internal organs and soft tissues is considered extremely challenging due to organ shifts and tissue deformation caused by patients movements such as respiration and repositioning. In our previous work [88], we proposed a fast registration method for deformable tissues with small rotation. In this study, we extend our method to deformable registration of soft tissues with large displacement. In this study, we analyzed the deformation field of the liver by decomposing the deformation into shift, rotation and pure deformation components, and concluded that in many clinical cases, the liver deformation contains large rotation and small deformation. This analysis justified the use of linear elastic theory in our image registration method. We also proposed a novel region-based neuro-fuzzy transformation model to seamlessly stitch together local affine models in different regions. We have performed the experiments on liver MRI image set and showed the effectiveness of the proposed registration method. We have also compared the performance of the proposed method with the previous method on tissues with large rotation and showed that the proposed method outperformed the previous method when dealing with the combination of pure deformation and large rotation. Validation results show that we can achieve a target registration error (TRE) of  $1.87 \pm 0.87$  mm, and an average centerline distance error (ACD) of  $1.28 \pm 0.78$  mm. The proposed technique has the potential to significantly improve registration capabilities and the quality of intra-operative image guidance. To the best of our knowledge, this is the first time that the complex displacement of the liver is explicitly separated into

local pure deformation and rigid motion.

## 6.1 Introduction

Soft organs such as the liver and the lungs can undergo large organ shift and tissue deformation in many medical procedures due to patient re-positioning, respiration, surgical manipulation, or other physiological reasons, for example, differences in bowel and stomach filling and weight loss. [21] [33] [61] [57]. Accurate deformable image registration is needed to compensate the displacements of these soft tissues [61] [8]. Although much work has been done in the field of deformable registration, it is still very challenging to efficiently achieve accurate deformable image registration of abdominal organs due to large organ shift and tissue deformation. Effective deformable registration techniques should be fast, accurate, physically consistent, topology preservation, and robust. Until recently, the majority of research on deformable registration of soft tissues requires a long time-consuming process [47] [57]. For example, the finite element method (FEM) provides a plausible image registration based on the bi-mechanical models [69]. However, in addition to the challenge of accurately determining the boundary conditions of complex shape of the organs and/or complex interaction forces between the ROI and surrounding tissues which is required by FEM, FEM suffers the problem of slow converge. On average, deformable registration of liver images takes 38 minutes [57]. Both accuracy and the speed are important factors that need to be considered. In the case of liver surgery, Lange et al. reported that registration accuracy in the range of 3 mm with a manual interaction time of about 10 minutes is reasonable for clinical application [81]. During radiotherapy treatment, it is highly desirable to achieve an image registration accuracy of better than 3 mm at the treatment target [88]. Based on these studies, in order to effectively make full use of the complementary images, the registration error between images of the liver should be controlled to be less than 3.0 mm and the registration time to be less than

10 minutes.

In order to satisfy and improve on these requirements, avoid local minima and guarantee physical consistency, in our previous work [89], we proposed a fast analytical solution to the deformable registration problem of the liver constrained by 3D curves. The advantages of our method include physically consistent alignment, analytical solution or topology preservation. This technique is based on minimal strain energy principle in linear elastic theory, and is valid for deformation with only small rotation. While small deformation with small rotation can be approximated by a linear elastic model, images of soft organs with large motion pose a challenge to this approximation, since the traditional linear elastic theory cannot effectively deal with the deformation involving large rotation as evidenced in liver resection procedures [33]. This is because in strain calculation, the high-order derivatives of displacement field cannot be ignored in the cases of the large motion. On the other hand, deformation with large rotation is a problem that is often encountered in the clinical setting. For example, in order to accurately localize the tumor for liver stereotactic body radiation therapy (SBRT) [8], a deformable image registration method was proposed to align the abdominal-compressed planning CT image to diagnostic MR images. The authors noticed that there is a large difference in liver shape between the CT image taken at the planning stage and the diagnostic MR images, which are mainly caused by abdominal compression, a procedure performed in order to reduce tumor motion induced by breathing.

Deformation pattern is an important research problem since a good understanding of the pattern can help us to choose a suitable registration method for deformable tissue registration. However there is few work in the literature to address and analyze the deformation pattern of the abdominal organs. In [33], the authors observed that, for 11 patients who underwent liver resection proce-

dures, there is a significant shape discrepancy or deformation between the livers before the surgery and during the surgery, which is caused by natural mobility, flexibility, and surgical manipulation for resection. A solely rigid alignment of the preoperative and intraoperative images of the whole liver results in a large misalignment of anatomical positions by several centimeters due to varying tissue deformation patterns in different regions of the liver. However, the local deformation of the segmental structure of the liver can be described/depicted by smooth variation of the displacements, and after a local rigid alignment of the local anatomical structure, the residual discrepancy (i.e. pure deformation) is reduced to less than 5 mm. Therefore, based on the above results, the overall large displacement of the liver during liver resection can be modeled as different large local rigid motions plus relative small deformations in different regions of the liver. In this study, we will analyze the deformation pattern of the liver and use the acquired knowledge of the pattern to formulate our registration method. We observed that surgeries often involve large deformation. However, in many scenarios, large rotation with small deformation is observed. For example, the displacement due to breathing or positioning can be modeled as large motion with small deformation. Moreover, in the non-surgical applications such as diagnosis or follow-up, MIS/Noninvasive procedures such as radiotherapy, High Intensity Focuses Ultrasound (HIFU) ablation or to avoid unnatural transformations [8], the assumption of large rotation with small deformation is often valid.

In this research, we extend our previous fast registration technique [90] to align deformable images involving large motion of soft tissues using a region-based neuro-fuzzy transformation model. In each region, a rigid transformation represents the local rigid motion while an affine transformation models the local deformation of soft tissues with separate rigid transformation. As a result, we provide an analytical global optimal solution to the deformable registration

problem by minimizing tissue strain energy constrained by 3D curves and point marks. The proposed method is fast and can overcome the local minima problem. Minimization of strain energy provides the resulting smooth deformation field and good generalization properties, prevents the issue of unnatural deformation, and leads to physically consistent deformable match of the images. We have validated our proposed technique with MR image data of human subjects. We have demonstrated the effectiveness of our deformable technique in registering MR liver images. Validation shows a target registration error of 1.87 mm and an average centerline distance error of 1.28 mm. This technique has the potential to significantly improve the registration capability and the outcomes of clinical procedures. The contributions of this research are three folds. First we analyzed the deformation field of the liver and proposed to separate the total displacement into large rotation and relatively small deformation, so the assumption of linear elastic model is proved to be valid. Secondly, region-based neural-fuzzy transformation models for large rotation are proposed to seamlessly piece together the local transformation models and guarantee the analytic solution. Finally, we extended our method to deformable registration with large rotation for the liver.

## 6.2 Analysis of Deformation Field of the Liver

Linear elastic theory is the best known and most widely used branch of solid mechanics due to its simplicity [69], and linear elastic theory based image registration can achieve a physically consistent solution that leads to fast analytical solution to deformable registration. The use of linear elastic theory requires that the deformable material is subject to small deformation and small rotation. However, in many clinical applications, the overall displacement of soft tissues, which may be caused by the breathing motion or patient positioning, is large. In this research, we will analyze the deformation patterns of different regions of the liver and investigate whether the linear elastic theory can be

employed for the rapid deformable registration of the liver. The comprehensive analysis of deformation patterns will also provide guidelines for proper selection of regions and their parameters in region-based deformable registration. In particular, first, we will analyze the deformation patterns of the liver of the human subjects, and use polar decomposition to separate the displacement of the liver into pure deformation and rigid motion. As a result, we justify that the real large displacement of the liver can be locally decomposed into relatively small pure deformation and large rigid motion.

In this research, we partition the liver into logical finite regions. The main advantage of this division is to create a multiple region-based sub models to represent the local motion and the local deformation for each region individually. Then we combine the transformations of the sub-models to form a unified transformation model such as the liver/organ.

In order to effectively analyze deformation patterns of soft tissues, in this section, we propose a novel technique to decompose overall displacements of soft tissues into rigid motion (rotation and translation) and pure deformation (scaling and shearing) region-by-region. To the best of our knowledge, this is the first time that the complex displacement of the liver is explicitly separated into local pure deformation and rigid motion. This separation also provides more understanding on the characteristics of the complex motion and deformation of the liver. Figure 6.1 shows the schematic of the decomposition of the deformation transformation to a rotation and a scaling transformation. The procedure to analyze the deformation patterns of the liver is as follows:

**Step 1:** For each region, we employ an affine transformation  $T(x) = Ax + t$  to approximate displacement vector  $u(x)$  in the neighborhood of a selected point. The approximation can be considered accurate since it is within a very

small radius equals to 3x3x3 voxels of the selected point.

**Step 2:** We employ a polar decomposition to decompose the affine matrix  $A$  into two components: a rotation matrix  $R$  and a stretching matrix  $P$  [26], i.e.

$$A = RP \quad (6.1)$$

Notice that the rotation transformation  $R$  does not produce any deformation. However, the component  $P$  represents the stretches of the soft tissues along a set of orthogonal axes. Therefore the stretching matrix  $P$  represents the pure deformation of soft tissues in the ROI, which contributes to the elastic potential energy stored in the soft tissues.

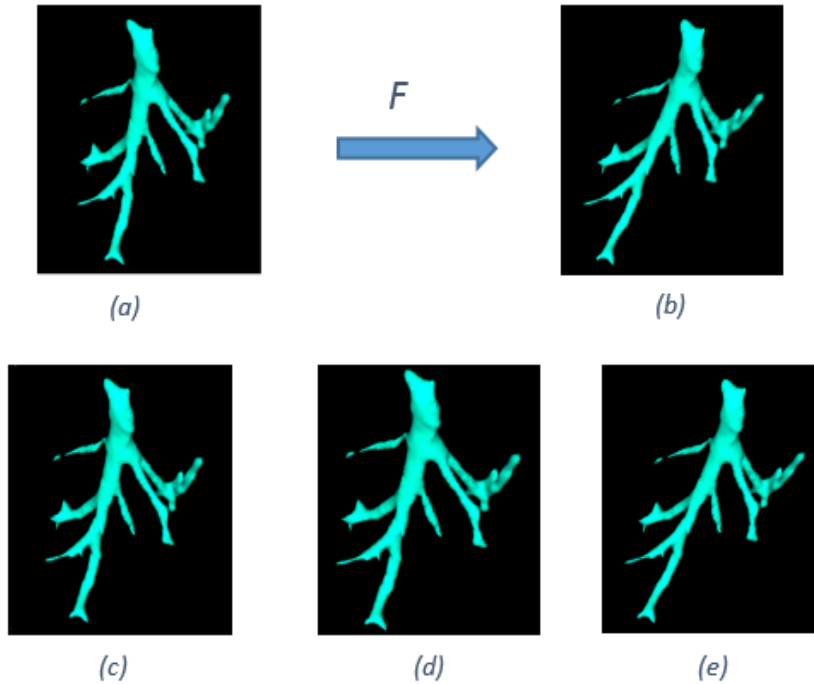


Figure 6.1: Schematic of how to decompose the deformable image: (a) Original sample vessel centerline (left) and (b) deformable image (right). (c) Rigid registration-rotation, (d) scale image, and (e) represent the deformable transformation by applying scaling and shearing

**Polar decomposition:** We employ the singular value decomposition of  $A$  [26] to perform the polar decomposition  $A = RP$  as follows.

$$A = USV^T \quad (6.2)$$

$$R = UV^T, P = VSV^T \quad (6.3)$$

where  $S$  is a diagonal matrix with positive diagonal elements for realistic deformation,  $U$  and  $V$  are orthogonal matrices. Furthermore, this computation also gives the principal scaling magnitudes represented by the diagonal elements of  $S$  in the three orthogonal directions, which are defined by the three columns of  $V$ .

Figure 6.2 shows the typical decomposition of a deformed ellipsoid object into pure stretching deformation and pure rotation. The green ellipsoid represents a part of soft tissues in the region of interest under deformation, the purple ellipsoid stands for the deformed one after pure deformation (stretching) consisting of scaling and shearing, its long axis represents the principal stretching direction, its short axes stand for the directions which are compressed. The red ellipsoid is obtained by applying pure rotation from deformed purple one. Figure 6.3 shows the deformation patterns within selected regions of the liver. We observe that the principal stretching orientations in different regions are different, and most regions deform in similar orientations.

Now, we present the decomposition of total displacements of the liver due to patient repositioning and/or respiratory motion. As shown in Figure 6.4, the total displacement  $u(x)$  of soft tissues at point  $x$  within a region is decomposed into three parts: pure deformation (i.e. stretching), rotation and translation/shift. In the centered affine transformation of a region  $T(x) = A(x - C) + C + t$ , where  $t$  is the translation,  $C$  is the center of rotation,  $A$  stands for the linear transformation, which can be further decomposed into two parts: pure defor-

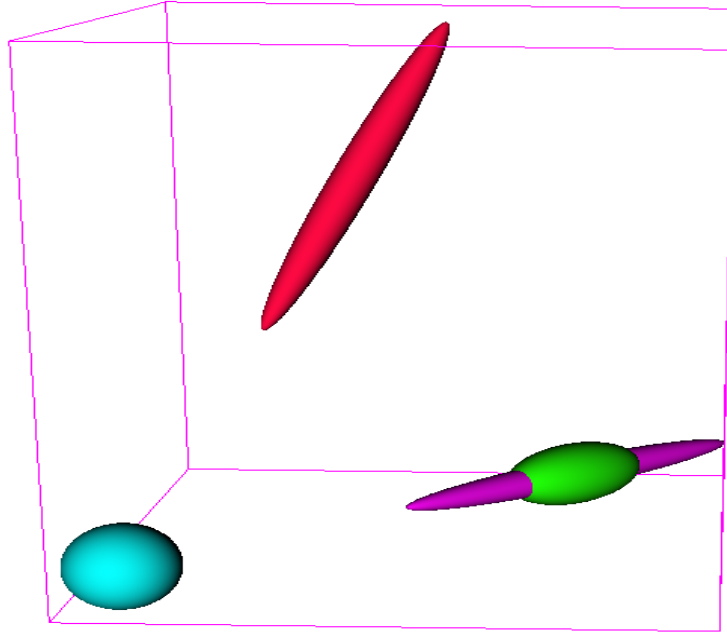


Figure 6.2: (a): This figure shows the typical decomposition of a deformed ellipsoid object into pure stretching deformation and pure rotation. The green ellipsoid represents a part of soft tissues in the region of interest under deformation, the purple ellipsoid stands for the deformed one after pure deformation/stretching consisting of scaling and shearing, its long axis represents the principal stretching direction, its short axes stand for the directions which are compressed. The red ellipsoid is obtained by pure rotation from deformed purple one

mation (stretching) and pure rotation by using polar decomposition. Figure 6.4 shows a schematic diagram for calculation of different components of the overall displacement vector at a point. Table 6.7 shows the quantitative results of displacement components in selected regions.

### 6.3 Observations and Analysis

Based on the decomposition of displacements between two images of the liver acquired at different positioning with breath-hold in Table 6.7, we have the following observations. First, the average displacement caused by pure deformation is approximately 5.27 mm, and the average of maximal scaling is 9.3%. Next, the average displacement caused by pure rotation is approximately 60.15 mm,

Table 6.7: Deformation patterns of 10 different regions

Region	Displacement (mm)			Rotation (Angle + axis)			Stretching				
	uM	uS	uR	ut	Angle	ax	ay	az	s1	s2	s2
1	70.028	5.087	37.357	65.539	102.565	0.017	-0.059	0.998	1.118	1.040	0.894
2	67.610	4.725	35.400	62.144	103.029	0.012	-0.058	0.998	1.106	1.055	0.891
3	93.125	3.679	58.987	59.903	110.242	0.003	-0.097	0.995	1.083	0.993	0.870
4	43.700	1.443	52.406	69.845	101.134	0.017	-0.085	0.996	1.060	0.990	0.947
5	112.627	8.380	74.751	99.430	99.635	0.048	-0.025	0.999	1.151	0.960	0.893
6	56.363	3.983	41.268	65.935	100.369	0.021	-0.068	0.997	1.071	1.024	0.933
7	102.542	4.255	92.288	97.234	102.355	0.064	-0.073	0.995	1.048	0.984	0.961
8	91.430	6.751	49.296	75.698	102.633	0.035	-0.072	0.997	1.137	1.008	0.882
9	106.470	7.107	84.817	103.25	98.738	0.004	-0.047	0.999	1.056	1.006	0.926
10	98.355	7.331	74.891	97.573	97.762	0.081	-0.030	0.996	1.097	1.019	0.917
Mean	84.225	5.274	60.146	79.655	101.846				1.093	1.008	0.911
STD	23.247	2.099	20.384	17.556	3.451				0.035	0.028	0.030

Note: uM - total displacement, uS from pure deformation, uR from rotation, ut from shift; (ax,ay,az) is the rotation axis, s1,s2,s3 stand for the scaling along principal axes respectively

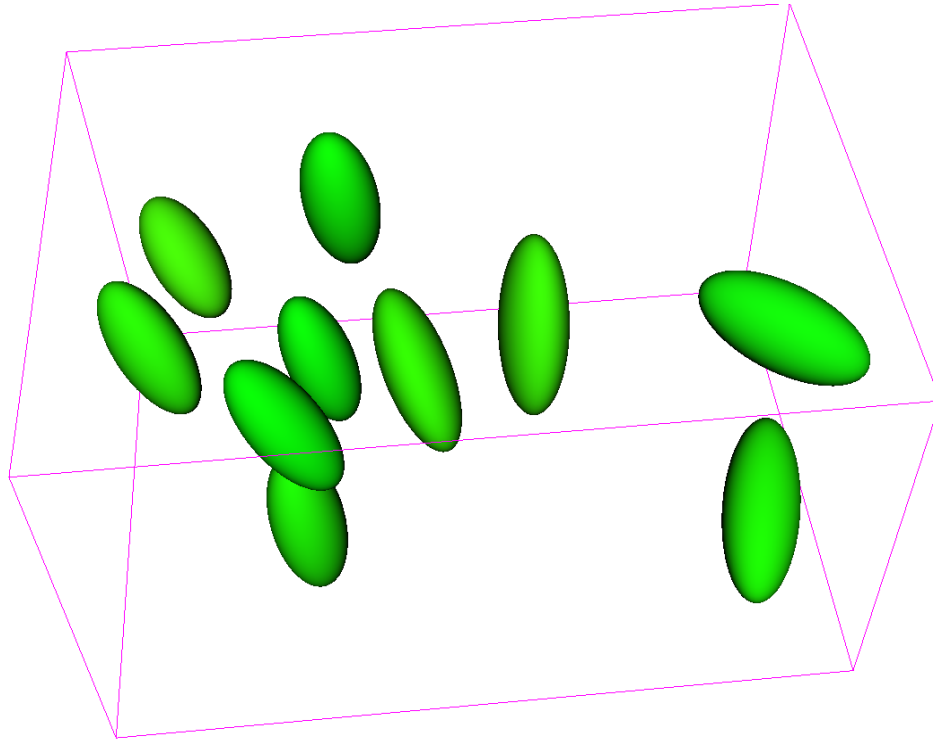


Figure 6.3: (b): This figure shows the deformation patterns within selected regions of the liver. We observe that the principal stretching orientations in different regions are different, and most regions deform in similar orientations

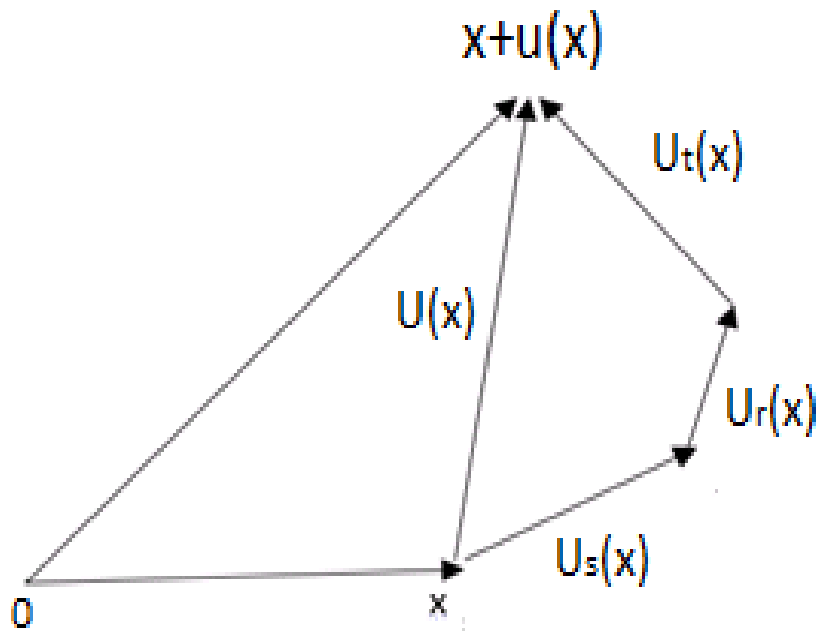


Figure 6.4: Displacement decomposition  $u(x) = U_s(x) + U_r(x) + U_t(x)$

and average rotation angle is 101.85 degrees. Finally, the average displacement caused by shift is approximately 79.66 mm. Therefore tissue shift dominates the overall displacements in each region. In summary, the pure deformations are small, therefore the assumptions of linear elastic theory are satisfied in each region. This justifies that we can apply the linear elastic theory to develop our new deformable registration algorithms.

## 6.4 Deformable Image Registration For Large Rotation

In deformable image registration, in general, no closed-form solutions exist to find the optimal registration parameters due to nonlinear and non-convex registration energy functions. Furthermore, the optimization methods often get trapped in a local minimum if the starting point is not close to the correct registration. In order to address the challenge of deformable image registration for soft tissue deformation involving large motion/rotation, we propose to use a multiple region based model to separately represent the local motion and local deformation. Specifically, a region-based neuro-fuzzy transformation model is used to depict the displacement field in the region of interest that is partitioned into  $N$  regions. For each region, a local transformation is proposed to model the corresponding two components: pure deformation is modeled by an affine transformation, and large rigid motion is represented by a local rigid transformation. This local model is a global function, which has good generalization within the region, and its effect range can be effectively localized by selecting the appropriate membership functions of the fuzzy set associated with the region, and the neuro-fuzzy inference system ensures the smooth transition across the regions. By proper design of registration components, we provide an analytical solution to the deformable registration involving large motion. The combination of the region based neuro-fuzzy transformation model and minimizing strain energy

leads to physically consistent and analytical solution to deformable registration.

In this research, we optimize a physics-based composite energy function. Our registration technique is based on elastic solid mechanics and the minimum strain energy principle. We aim to minimize the following energy function:

$$J = w_e E_e(x) + w_c E_c(x) + w_m E_m(x) \quad (6.4)$$

where  $E_e(x)$  is strain energy produced by deformation of soft tissues,  $E_c(x)$  the distance energy between pairs of 3D vessel centerlines extracted from the fixed and moving images,  $E_m(x)$  the distance energy between corresponding point marks such as bifurcation points, and  $w_i$ s weight relative importance of each term. This energy function measures the quality of alignment between two sets of blood vessels, and alignment between two sets of point marks, and the strain energy produced by soft tissue deformation. We discuss different registration components in detail in the following sections

## 6.5 Region-based Neuro-fuzzy Transformation Model

The non-rigid transformation model is a key component in deformable image registration, which determines computational complexity of image registration process and capability to depict the real deformation of soft tissues. In this research, we extend a region-based neuro-fuzzy transformation model proposed in our previous work [87] to model the deformation of soft tissues involving large motion and rotation. This model consists of two parts: multiple different local models for different regions, and a neuro-fuzzy system that is used to seamlessly and smoothly integrate multiple local models into a unified deformable transformation model [89]. Based on the characteristics of deformation in each region, we can select a different local model that best depicts the local deformation of

that region.

In this research, for each region  $i$ , the following transformation is employed to depict the local deformation with large motion i.e.(rotation and translation).

$$T_i(x) = T_{iR}(x) + T_{iA}(x) \quad (6.5)$$

$$T_{iR}(x) = A_{iR}(x - C_i) + b_{iR} + C_i \quad (6.6)$$

$$T_{iA}(x) = A_{iA}(x - C_i) + b_{iA} + C_i$$

where

$$A_{iR} = \begin{pmatrix} A_{iR11} & A_{iR12} & A_{iR13} \\ A_{iR21} & A_{iR22} & A_{iR23} \\ A_{iR31} & A_{iR32} & A_{iR33} \end{pmatrix}, A_{iA} = \begin{pmatrix} A_{iA11} & A_{iA12} & A_{iA13} \\ A_{iA21} & A_{iA22} & A_{iA23} \\ A_{iA31} & A_{iA32} & A_{iA33} \end{pmatrix}$$

and

$$b_{iR} = \begin{bmatrix} b_{iR1} \\ b_{iR2} \\ b_{iR3} \end{bmatrix}, b_{iA} = \begin{bmatrix} b_{iA1} \\ b_{iA2} \\ b_{iA3} \end{bmatrix}, C_i = \begin{bmatrix} C_{i1} \\ C_{i2} \\ C_{i3} \end{bmatrix}$$

where  $C_i$  is the rotation center for both the rigid and affine transformations in region  $i$ .  $T_{iR}(x)$  is a fixed rigid transformation for the local rigid motion part, and  $T_{iA}(x)$  is the centered affine transformation that mainly depicts deformation part caused by scaling and shearing and possibly including residual small motion that is not modeled by  $T_{iR}(x)$  in Region  $i$ . Since rigid motion does not cause any deformation of soft tissues, it will not produce any strain energy. Therefore, only affine part is taken into account when the strain energy term in the registration energy function is calculated. This local transformation model is mathematically equivalent to the small deformation represented by  $T_{iA}(x)$  followed by a large motion of  $T_{iR}(x)$ . In this research, we can still

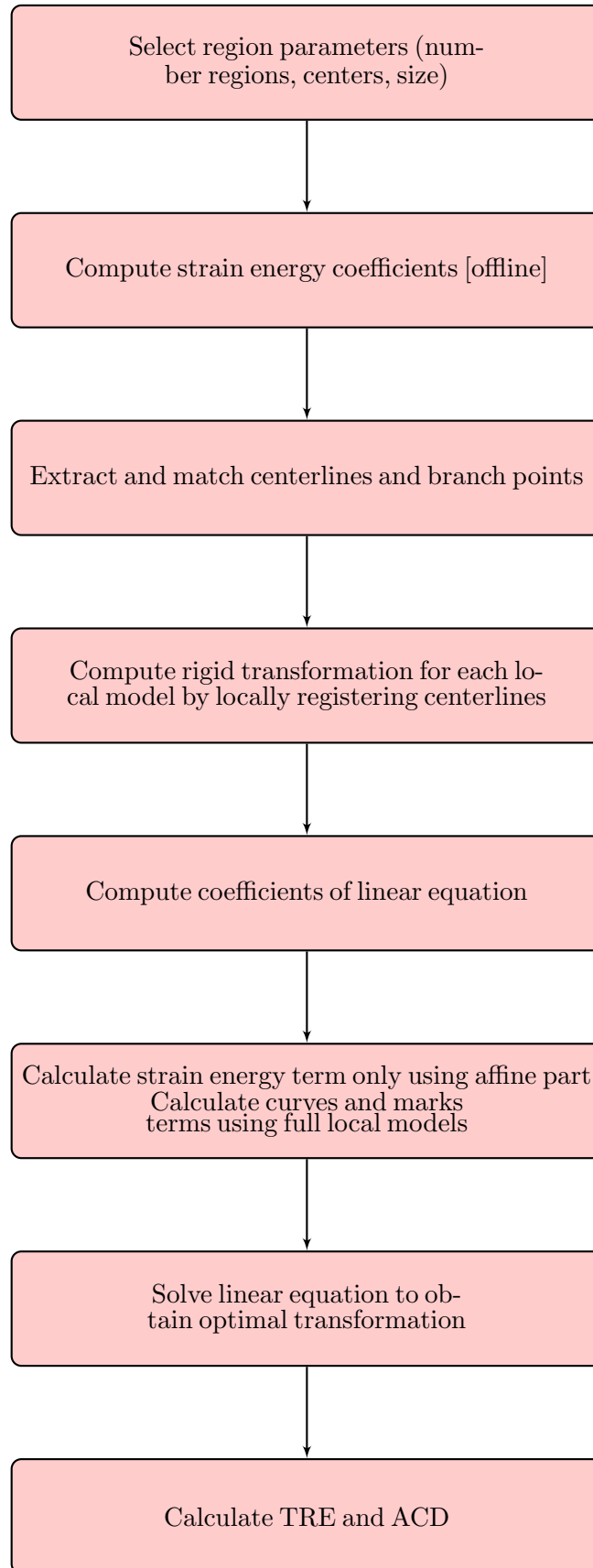


Figure 6.5: Schematic of the proposed method flowchart

use linear elastic solid theory [20] to locally calculate the strain energy in each region without local rigid motion, which avoids the inaccuracy caused by large rotation in strain calculation.

In order to facilitate the derivation of analytical solution to our deformable registration problem 6.1, we need to rewrite the local transformation  $T_i(x)$  as an explicit linear function of transformation parameters.

$$P_{TiA} = [A_{iA11}, A_{iA12}, A_{iA13}, A_{iA21}, A_{iA22}, A_{iA23}, \\ A_{iA13}, A_{iA23}, A_{iA33}, b_{iA1}, b_{iA2}, b_{iA3}] \quad (6.7)$$

$$P_{TiR} = [A_{iR11}, A_{iR12}, A_{iR13}, A_{iR21}, A_{iR22}, A_{iR23}, \\ A_{iR13}, A_{iR23}, A_{iR33}, b_{iR1}, b_{iR2}, b_{iR3}]^T \quad (6.8)$$

where  $P_{TiA}$  is the corresponding 12 parameters  $(A_{iA}, b_{iA})$  of  $T_i(x)$  and  $T_{iA}(x)$  i.e. variables to be optimized during image registration, and  $P_{TiR}$  is the corresponding 12 parameters  $(A_{iR}, b_{iR})$  of the local rigid transformation  $T_{iR}(x)$ , which are determined locally before deformable registration.

Therefore, we rewrite Eq.6.5 as follows:

$$T_i(x) = A_{pTiA}^T(x)p_{TiA} + B_{pi}(x) \quad (6.9)$$

where

$$\begin{aligned} B_{pi}(x) &= A_{pT_iR}^T(x)p_{T_iR} + 2C_i, \\ A_{pT_iA}^T(x) &= A_{pT_iR}^T(x) \end{aligned}$$

$$= \begin{pmatrix} x_1 - C_{i1} & x_2 - C_{i2} & x_3 - C_{i3} & 0 & 0 & 0 & 0 & 0 & 0 & 0 & 1 & 0 & 0 \\ 0 & 0 & 0 & x_1 - C_{i1} & x_2 - C_{i2} & x_3 - C_{i3} & 0 & 0 & 0 & 0 & 0 & 1 & 0 \\ 0 & 0 & 0 & 0 & 0 & 0 & x_1 - C_{i1} & x_2 - C_{i2} & x_3 - C_{i3} & 0 & 0 & 0 & 1 \end{pmatrix}$$

From Equation 6.9, we clearly see that  $T_i(x)$  is a linear function of local transformation parameters  $p_{T_iA}$ .

### 6.5.1 Computation of Local Rigid Transformation

In order to obtain the local rigid transformation  $T_{iR}(x)$  of each region  $i$ , we minimize a weighted square error distance between corresponding centerlines within the neighborhood of each region center as follows.

$$E_c(p) = \sum_{i=1}^{N_c} \sum_{k=1}^{N_{ci}} \frac{1}{2} w(X_{fik}) \left\| T_{iR}(X_{fik}) - X_{mik} \right\|^2 \quad (6.10)$$

where

$$w(x) = \exp \left\{ - \left[ \frac{(x - c_{ix})^2}{2\sigma_x^2} + \frac{(y - c_{iy})^2}{2\sigma_y^2} + \frac{(z - c_{iz})^2}{2\sigma_z^2} \right] \right\}$$

where  $\{X_{fik}, X_{mik}\}$  are resampled equidistant points on the  $i$ -th centerline, that is, for each matched pair of fixed and moving centerlines, the same number of points are resampled with equidistance. In this case, when the points of centerlines are far away from the region center, the corresponding weights  $w(x)$  will decrease, that is, the distant centerline points have much less effect on the resulting rigid transformation. Therefore, the resulting rigid transformation reflects the dominant local rotation and translation of the soft tissues. Note that we do not need a very accurate local rigid transformation because the residual

rigid transformation errors that include small rotation and translation can be further addressed by the affine term. According to the linear elastic theory, the affine term is employed to achieve an accurate registration under the condition of small rotation by minimizing the strain energy.

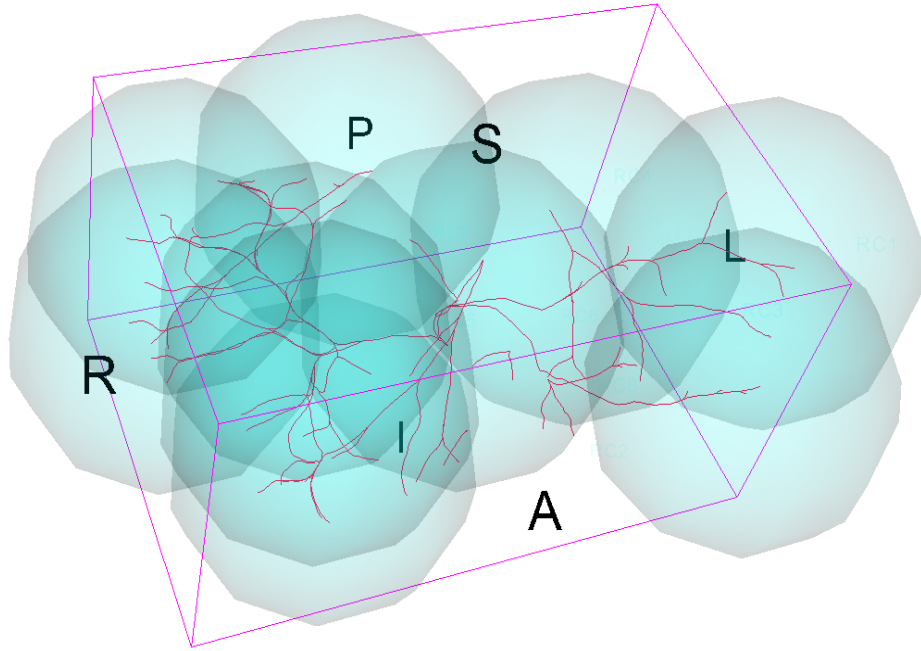


Figure 6.6: configuration of local regions

Based on the analysis of deformation patterns of the ROI, we partition the whole ROI into multiple regions as shown in Figure 6.6, each having different local transformation model  $T_i(x)$ . Since the real deformation of the ROI within the organ is smooth in the applications under consideration, a neuro-fuzzy system is employed to seamlessly integrate multiple local models into a unified deformable transformation model to ensure smooth transition across the different regions [89]. Our neuro-fuzzy system has the following  $N_R$  rules:

*Fuzzy rule 1: If point  $x$  is in region  $R_1$ , then  $\acute{x} = T_1(x)$*

*Fuzzy rule 2: If point  $x$  is in region  $R_2$ , then  $\acute{x} = T_2(x)$*

...

*Fuzzy rule  $N_R$ : If point  $x$  is in region  $R_{N_R}$ , then  $\acute{x} = T_{N_R}(x)$*

where  $x$  is a 3D point in the fixed image space,  $\acute{x}$  the corresponding transformed point,  $T_i(x)$  a local transformation model specifically tailored to Region  $i$ .

The overall deformable transformation within the entire ROI can be derived as [89] ,

$$\acute{x} = T_{NF}(x) = \frac{\sum_{i=1}^{N_R} M_i(x)T_i(x)}{\sum_{i=1}^{N_R} M_i(x)} \quad (6.11)$$

$$M_i(x) = \exp \left\{ - \left[ \frac{(x - c_{ix})^2}{2\sigma_x^2} + \frac{(y - c_{iy})^2}{2\sigma_y^2} + \frac{(z - c_{iz})^2}{2\sigma_z^2} \right]^{C_{GN}} \right\} \quad (6.12)$$

where  $M_i(x)$  is the membership function of a fuzzy set associated with region  $R_i$ . In this research, the generalized Gaussian membership function (see Figure 6.7) is chosen for each local region ( $C_{ix}, C_{iy}, C_{iz}$ ), are the region center  $\sigma_{ix}, \sigma_{iy}, \sigma_{iz}$ , and  $C_{GN}$  are used to control the effective range of local model  $T_i(x)$  , large  $C_{GN}$  will effectively limit the local model within the range of  $\sigma_{ix}, \sigma_{iy}, \sigma_{iz}$  .

Using Equation 6.9, we can rewrite the overall transformation 6.11 for the entire region of interest in the following form:

$$T_{NF}(x) = T_{NF}(x, p) = A_p^T(x)p + B_p(x) \quad (6.13)$$

where

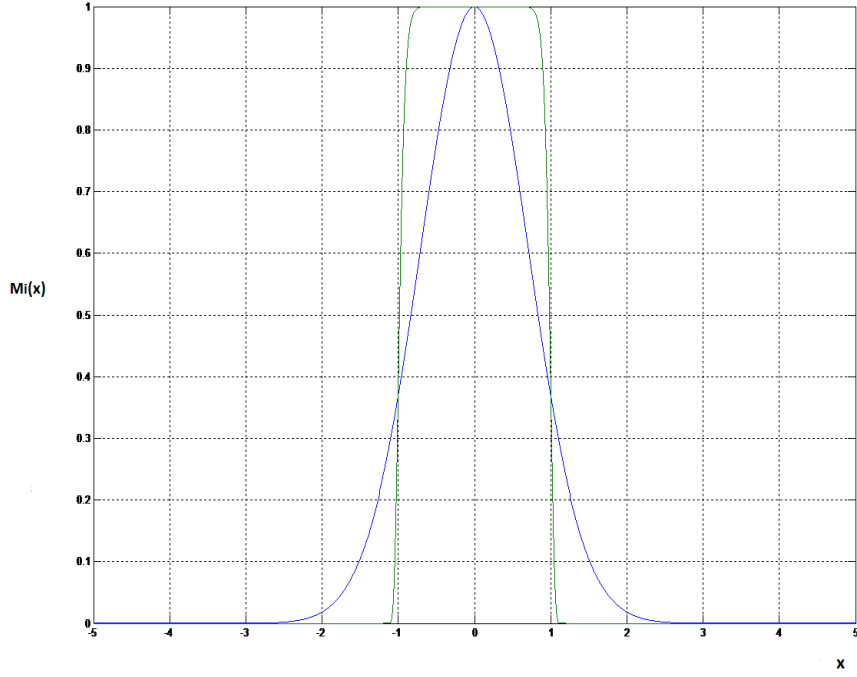


Figure 6.7: 1D Generalized Gaussian function

$$\begin{aligned}
 p &= [p_{T1A}^T \ p_{T2A}^T \ \cdots \ p_{TNRA}^T], \\
 A_p^T(x) &= \left[ M_{n1}(x)A_{p_{T1A}}^T \ M_{n2}(x)A_{p_{T2A}}^T \ \cdots \ M_{nNR}(x)A_{p_{TNR A}}^T \right], \\
 B_p(x) &= \sum_{i=1}^{N_R} M_{ni}(x)B_{pi}(x), \\
 M_{ni}(x) &= M_i(x) / \sum_{i=1}^{N_r} M_i(x)
 \end{aligned}$$

$p$  is adjustable parameters in the overall transformation model  $T_{NF}(x)$ , including all the parameters of local affine transformations. Note that the  $T_{NF}(x)$  is a nonlinear transformation with respect to spatial coordinates  $x$ , but is linear with respect to transformation parameters  $p$ . Combined with the constraints of 3D curves, point marks and strain energy below, this linearity of parameters  $p$  leads to fast analytical solution. Furthermore, we can easily to calculate the

derivative of  $T_{NF}(x)$  with respect to the parameters  $p$  as follows:

$$\frac{\partial T_{NF}(x)}{\partial p} = A_p^T(x)$$

## 6.6 Analytical solution to registration energy function

In this section, we briefly define each term in the registration energy function 6.4, and provide the formulas for their derivatives with respect to the transformation parameters  $p$ . The derivation is similar to our previous work [88].

**Strain Energy:** The strain energy term prevents the issues such as overfitting, and leads to physically consistent deformable match results. Based on elastic solid mechanics, strain energy is generated only by deformation of soft tissues, and can be calculated using the Saint-Venant model [69], as follows:

$$E_e = \int \int \int W(E) dx dy dz \quad (6.14)$$

where

$$\begin{aligned} W(E) &= 0.5\lambda[tr(E)]^2 + \mu.tr(E^2), \\ tr(E) &= e_{11} + e_{22} + e_{33}, \\ e_{ij} &\approx \frac{1}{2} \left[ \frac{\partial T_{NF A i}}{\partial x_j} + \frac{\partial T_{NF A j}}{\partial x_i} - 2\delta_{ij} \right] \end{aligned}$$

where  $W(E)$  is the strain energy density,  $E$  a strain tensor,  $E = (e_{ij})_{3 \times 3}$ , and  $(\lambda, \mu)$  tissue elastic parameters. Note that the strain energy is calculated using only affine part of the overall transformation  $T_{NF}(x)$ .

We can rewrite the strain energy as a quadratic function of the transforma-

tion parameters  $p$  in the following formula: From Appendix B, we have,

$$W(E) = C_0(x) + C_1^T(x)p + p^T C_2(x)p \quad (6.15)$$

Therefore,

$$\begin{aligned} E_e(p) &= C_{e0} + C_{e1}^T p + \frac{1}{2} p^T C_{e2} p, \\ C_{e0} &= \int \int \int C_0(x) dx dy dz, \\ C_{e1} &= \int \int \int C_1(x) dx dy dz, \\ C_{e2} &= \int \int \int C_2(x) dx dy dz, \end{aligned}$$

where constants ( $C_{e0}, C_{e1}, C_{e2}$ ) can be calculated offline in advance based on the pre-procedural image.

**Curve energy:** We have proposed an efficient novel technique to analytically calculate the closest point on a 3D curve to a given point, and the derivative of the distance between curves with respect to transformation parameters through a parametric representation of 3D curves [88]. We aim to minimize the distance between pairs of corresponding vessel centerlines, which is formulated as minimizing the following function:

$$E_c(p) = \sum_{i=1}^{N_c} \sum_{k=1}^{N_{Ci}} \frac{1}{2} \|T(X_{fik}) - C_{mi}(t)\|^2 \quad (6.16)$$

where  $N_c$  is the total number of vessel centerlines,  $N_{Ci}$  the number of discrete points on the  $i^{th}$  centerline from the fixed image,  $X_{fik}$ ,  $i = 1, 2, \dots, N_{Ci}$  is the  $k^{th}$  point on the  $i^{th}$  centerline from the fixed image,  $C_{mi}(t)$  the parametric representation of the  $i^{th}$  vessel centerline from the moving image. For simplicity we limit our discussion to finding the closest point on a 3D curve in the moving image for a transformed point of the fixed image.

Its derivative is as follows.

$$\begin{aligned}
L_{pc} &= \sum_{i=1}^{N_c} \sum_{k=1}^{N_{ci}} \left\{ A_p(X_{Tfik}) D_{cmik}^T A_p^T (X_{Tfik}) \right\}, \\
Y_{pc} &= \sum_{i=1}^{N_c} \sum_{k=1}^{N_{ci}} \left\{ A_p(X_{Tfik}) D_{cmik}^T X_{cmik} \right\}, \\
D_{cmik}^T &= I_{3 \times 3} - \left( \frac{\partial t}{\partial X_{Tfik}} \right) \left( \frac{\partial C_{mi}(t)}{\partial t} \right)^T
\end{aligned}$$

Note that  $\frac{\partial E_c(p)}{\partial p}$  is a linear function of parameters  $p$ , which implies that the shortest distance between curves  $E_c(p)$  is a quadratic function of transformation parameters  $p$ .

**Point mark energy:** Point marks are employed to anchor the deformation at some specific locations. We assume that there are  $N_m$  pairs of corresponding point marks (i.e. bifurcation points),  $(X_{fk}, X_{mk}), k = 1, 2, \dots, N_m$ . Then we minimize the distance between corresponding point marks by adding the following term to the registration energy function,

$$E_m(p) = \sum_{i=1}^{N_m} \frac{1}{2} \|T(X_{fk}) - X_{mk}\|^2 \quad (6.17)$$

Its derivative with respect to transformation parameters can be analytically calculated through the following formula,

$$\frac{\partial E_m(p)}{\partial p} = \sum_{i=1}^{N_m} A_p(X_{fk})(T(X_{fk}) - X_{mk}). \quad (6.18)$$

From the above derivation, all the three terms are quadratic functions of the transformation parameters  $p$ . Therefore, the global optimal transformation parameters can be calculated analytically by solving linear equations  $\frac{\partial j}{\partial p} = 0$ . This solution is globally optimal, and there are no local minima in this registration energy function.

## 6.7 Registration Accuracy Measures

In order to evaluate the quality of our proposed registration approach, we adopt the following two accuracy measures to assess the registration accuracy.

### 6.7.1 Landmark-based Target Registration Errors (TRE)

In this assessment, landmarks (targets) were defined as bifurcation points of blood vessels and were localized in both MR image spaces. The resulting registration transformation was applied to transform the landmarks in the fixed image space to the moving image space, TREs were then calculated in the same coordinate system. The TRE is defined as the root mean square (rms) of the distances between the landmarks in the moving MR image and the corresponding homologous landmarks in the fixed MR image after registration [37]. After vessel centerlines were extracted, bifurcation points were calculated as the intersections of the centerlines using custom software, bifurcation correction was then performed to obtain more consistent homologous bifurcation points across different MR images [90].

### 6.7.2 Average Vessel Centerline Distance (ACD)

Since major bifurcation points are easily identified in the central part of the liver, blood vessel centerlines cover a larger region of the liver and are employed to measure registration error, i.e. the average centerline distance between two corresponding centerlines after registration. In this research, the centerlines were extracted using Slicer VMTK centerline extraction modules [48], [44].

### 6.7.3 Average Vessel Centerline Distance of Independent Points (ACDIP)

When the ACD is computed, the discrete points  $x_{Fik}$ 's on the  $i^{th}$  centerline in the fixed image are used for registration. To calculate the ACDIP, we employ

a different set of discrete points  $x_{FIPik}$ 's resampled on the centerlines of the fixed images. These points are independent of  $x_{Fik}$ 's, and are not utilized for registration. Therefore the ACDIP is calculated as follows:

$$ACDIP = \frac{1}{N} = \sum_{i=1}^{N_c} \sum_{k=1}^{N_{ci}} \|T(X_{FIPik}) - C_{Mi}(t_{cik})\|$$

where  $X_{FIPik}$ 's are discrete points on centerline  $i$  in the fixed image,  $C_{Mi}(t_{cik})$  the closest point on the  $i^{th}$  centerline in the moving image from the transformed point  $T(x_{FIPik})$ , and  $T(x)$  the resulting registration transformation. This metric is used to assess the alignment accuracy of centerline parts which are not used for registration.

## 6.8 Experimental Results

In this section, we present registration results of liver MR images using our proposed deformable registration method. The images used in this research were acquired from human volunteers. High-quality dynamic MR images were acquired in the axial plane using a 1.5T GE scanner (GE Medical Systems, Milwaukee, WI). Image acquisition was performed using the LAVA gradient echo sequence with TR=3.79 ms, TE=1.72ms, a flip angle of 12 degrees, an image matrix size of 256 x 256, in-plane pixel size of 1.3 mm x 1.3 mm and slice thickness of 1.5 mm. Image sets were acquired with a breath-hold at different positioning. Note that, in image acquisition, TR (Repetition Time) represents the amount of time that exists between successive pulse sequences applied to the same slice. See also Repetition Time. While, TE (Echo Time) - represents the time in milliseconds between the application of the 90 ° pulse and the peak of the echo signal in Spin Echo and Inversion Recovery pulse sequences [73].

### 6.8.1 Visual Inspection: Overlay of Images/Vessels

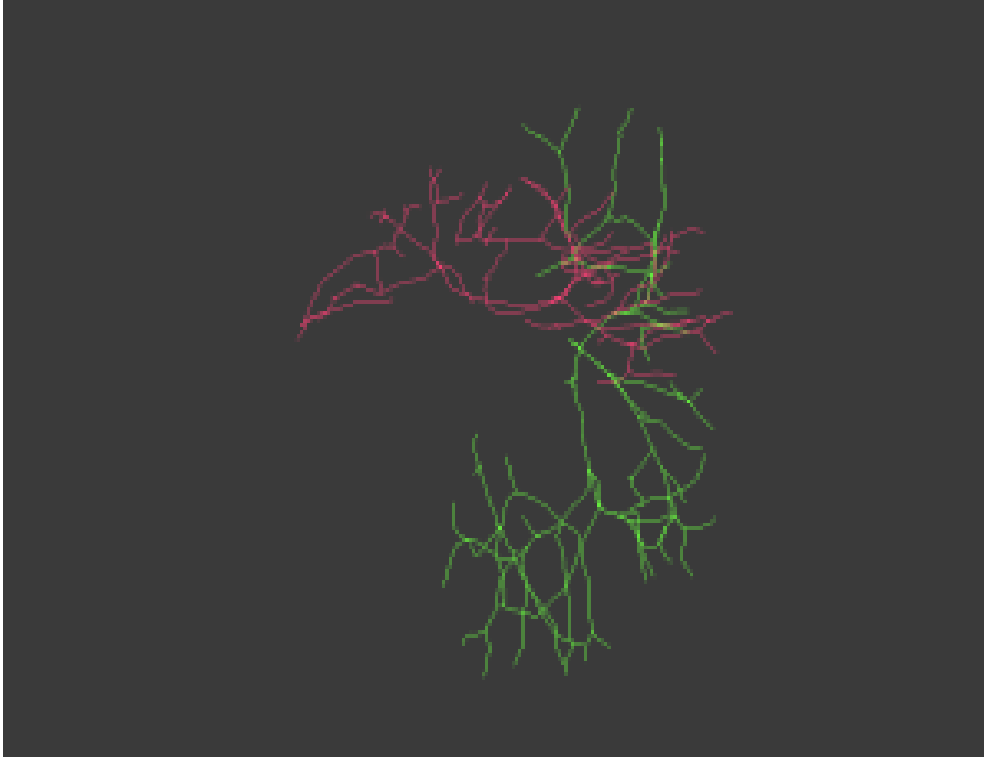


Figure 6.8: Centerlines before match. Red lines: lateral decubitus, green lines: supine position

Before deformable registration, Figure 6.8 shows soft tissue deformation involving large rotation between two sets of the centerlines at different patient positioning. The selected overlays of the centerlines after registration are shown in Figure 6.9 using 10 sub-models, which demonstrate that the centerlines are matched well after registration.

## 6.9 Registration Accuracy: TRE and ACD

To quantitatively evaluate the registration accuracy, we considered two accuracy metrics: target registration error (TRE) and average centerline distance (ACD). The resulting average TRE of 56 bifurcation points was 1.87 mm, and the average ACD of 109 vessel branches is 1.28 mm. These registration accuracy measures have demonstrated that the proposed deformable registration technique is able to accurately register two sets of deformable images involving

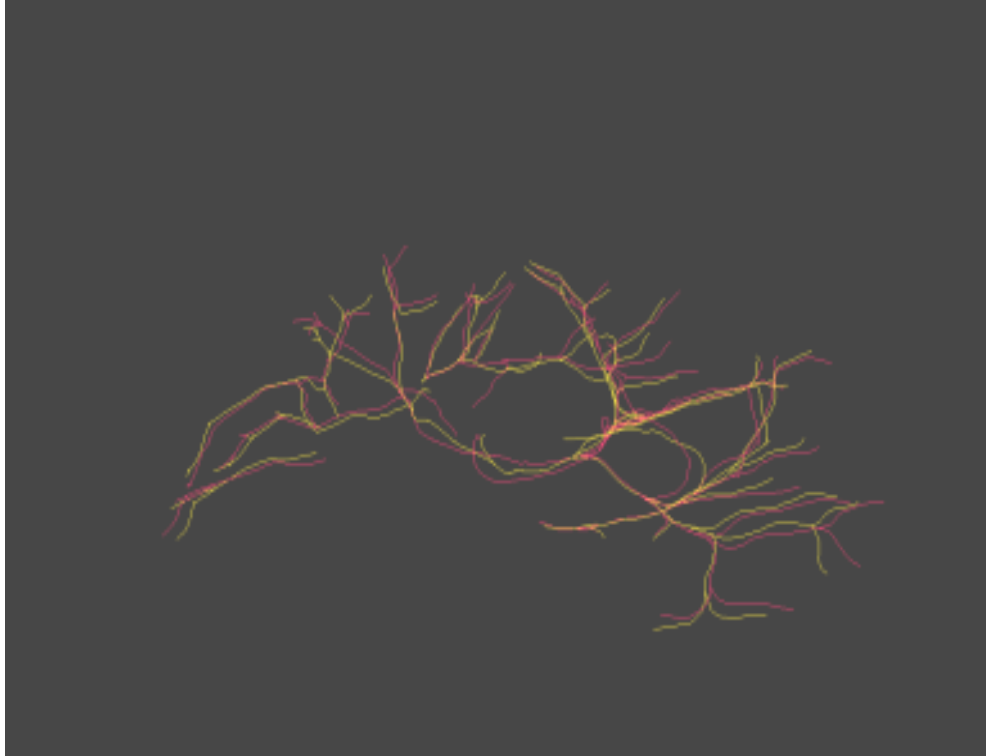


Figure 6.9: Overlay of centerlines after match. Red lines: left lateral decubitus, yellow lines: supine centerlines mapped to lateral decubitus

large rotations at different regions. The average registration time was about one second on a computer with Core 2 Quad 2.6 GHz Intel CPU and memory of 4 GB.

## **6.10 Comparison With the Conventional NFS Method Without Using Large Rotation Formulation**

In this section, we compare the proposed method designed for large rotation with the conventional NFS method. The results are shown in Table 6.8. From these results, we observe that the proposed method outperforms the conventional NFS method for all evaluation criteria. The results can be explained as follows: if the soft tissues undergo small deformation and large rotation, the assumption of using linear elastic theory becomes invalid. And since the conven-

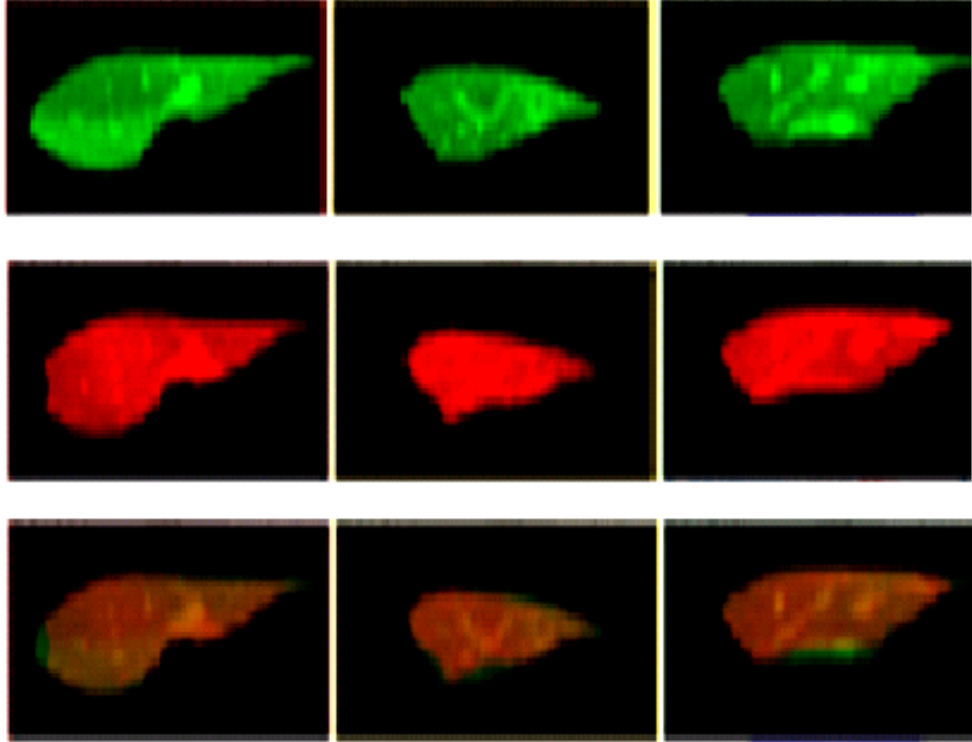


Figure 6.10: Overlay of images before and after registration. In each plot, first row: three orthogonal slices of 3D MR fixed image, 2nd row: three orthogonal slices of 3D MR moving image before or after registration, 3rd row: overlay of two images; left column: axial view, middle column: sagittal view, and right column: coronal view. Note that the overlay of bright green and bright red vessels is yellow, internal vessels are correctly matched after registration

tional NFS method is based on the linear elastic theory, the registration using the conventional NFS method naturally results in a relatively large mapping error. However, for the proposed method, since it first utilizes an additional local rigid motion to correct the large displacement between the two images, and the residual discrepancy can be accurately represented by the linear elastic theory, as a result, the registration can achieve an accurate alignment.

Table 6.8: Comparison of registration accuracy (UNIT: MM)

Method	TRE	ACD	ACDIP
		(mean $\pm$ SD)	(mean $\pm$ SD)
Proposed NFS	$1.87 \pm 0.87$	$1.28 \pm 0.78$	$1.25 \pm 0.76$
Conventional NFS	$5.32 \pm 2.25$	$4.71 \pm 2.61$	$4.66 \pm 2.57$

## 6.11 Summary

We have presented a new solution to the deformable registration of MR images of soft tissues with large motion. The proposed method can achieve a fast analytical global optimal solution. It is an extension of our previous work and tackles one type of deformable registration problems which are typically encountered in many procedures on internal organs and tissues in which the large displacement can be modeled as large motion and relatively small deformation in each region. A novel neuro-fuzzy transformation model has also been proposed to adapt the previous formulation to the registration problem with large motion in order to achieve a fast, analytical solution.

This analytical solution to the registration problem can be employed to rapidly match internal structures of organs. It can be also used to dynamically update guidance vessel models for vessel extraction in our joint registration and segmentation framework.

# Chapter 7

## Automatic Surface Reconstruction for Endoscopy-MR Image Fusion

Minimally invasive endoscope based abdominal procedures provide potential advantages over conventional open surgery such as reduced trauma, shorter hospital stay, and quick recovery. One major limitation of using this technique is the narrow view of the endoscope and the lack of proper 3D context of the surgical site. In this thesis, we propose a rapid and accurate method to align intra-operative stereo endoscopic images of the surgical site with pre-operative MR images. Gridline light pattern is projected on the surgical site to facilitate the registration. The purpose of this surface-based registration is to provide 3D context of the surgical site to the endoscopic view. Our experiment results show that our method outperforms the existing method in terms of correct matching rate 98% which is an indicator of the surface reconstruction accuracy.

In this thesis, we develop a new method for endoscopy-MR image fusion of the liver organ for minimally invasive endoscope based surgery. Image guidance is an essential tool in minimally invasive endoscope based abdominal procedures [52]. Effective image guidance can compensate the restricted perception during the operation, which is considered a major limitation in endoscopic procedures. Without image guidance, the surgeon cannot see through the surface of the operation site and may accidentally cause damages to the critical structures of the patient. A typical procedure in image guidance is to map pre-operative high quality MR images to intra-operative endoscopic video images or the patient thereby provide a good quality context to the real-time endoscopic images.

Thus, the surgeon will be able to visually access the operation site during the procedure. As a result, the damage to the critical organs or tissues will be substantially minimized.

Fusion of endoscopic video images with high quality MR images requires good matching of these two modalities. In this research, we adopt a surface based image fusion because the two modalities are different in acquisition and nature [60] [43]. In order to find the corresponding 3D surface model from endoscopic images, we utilize stereovision to snapshot the surgical site from two different angles and compute the 3D location by using triangulation [93]. Cameras are calibrated before triangulation is used [54] [83].

Although a liver phantom is used to validate the proposed technique, our method is not restricted to the liver surgery. The integrated image guidance can also be applied to other endoscopic procedures. This research is organized as follows. Section 7.1 introduces the experimental setup and the camera calibration of the stereo endoscope. Section 7.2 discusses automatic surface reconstruction, and Section 7.3 presents surface based registration and experimental results of image fusion. lastly, section 7.4 presents the conclusion and future work.

## **7.1 Experimental Setup and Camera Calibration**

Experimental setup is shown in Figure 7.1. In the experiments of this research, we use the following major components: a Visionsense VSII stereo endoscope, an Optoma PK301 Pocket Projector, a liver phantom, and a chessboard calibration pattern. Optoma PK301 Pocket Projector is a tiny size projector furthermore can be quickly mounted. The resolution of this projector is 848 by 480 pixels. The liver phantom was printed using a 3D printer based on the liver model that

was segmented from MR images of a human subject.

In this research, robust 3D surface reconstruction requires an accurate camera calibration of the stereo endoscope. The calibration process aims to find intrinsic parameters and correct the optical distortion inherent in the endoscope, and to compute extrinsic parameters to capture the spatial relationship between left and right cameras of the stereo endoscope. We have modified the Camera Calibration Toolbox for Matlab [12], and performed calibration of the stereo endoscope using a chessboard calibration pattern.



Figure 7.1: Experimental setup for stereo endoscope and liver phantom

## 7.2 Surface Reconstruction From Stereo Endoscopic Images

In this section, we propose a novel approach to reconstruct the surface of the surgical site from two stereo endoscopic images. The reconstruction procedure

is shown in Figure 7.2. First, a gridline pattern is projected on the surgical site and both left and right images are acquired at the same time. Second, the intersection points of the gridlines are automatically detected and matched in both images. Then we reconstruct the surface with the matched intersection points. Major steps will be described in detail in the following sections.

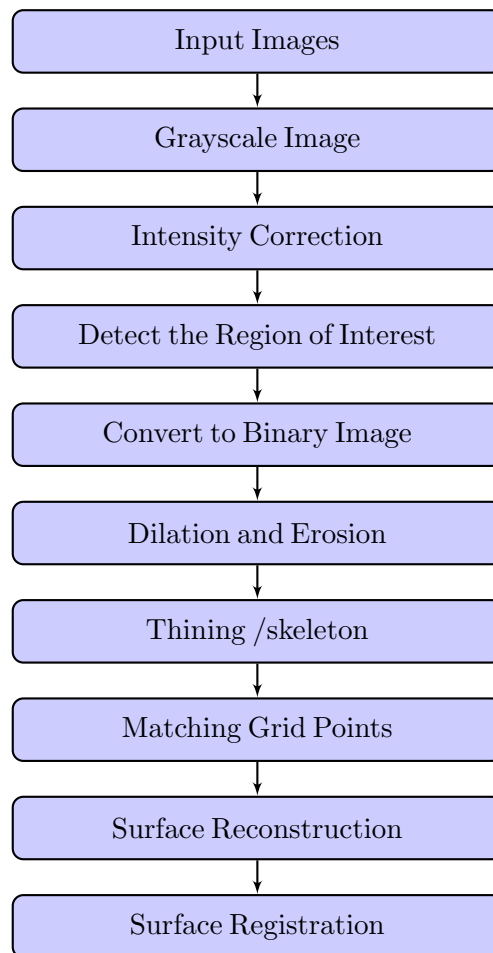


Figure 7.2: Flowchart for automatic fusion of intraoperative endoscopic images to pre-operative images

### 7.2.1 Conversion of Input Images to Grayscale Images

In order to detect the intersections of the grid lines pattern of an image, we use the image of binary format as the algorithm input. We first convert the color images acquired from the stereo endoscope to grayscale images (as shown in Figures 7.3 and 7.4). The gridlines of the light pattern in the images should be bright, such that the consequent processes use the bright pattern to recognize

their intersections. Hence, the grayscale image is inverted in color to meet this constraint. In this process, the dark areas become bright and vice versa. Next, multiple steps are employed to obtain good binary images.

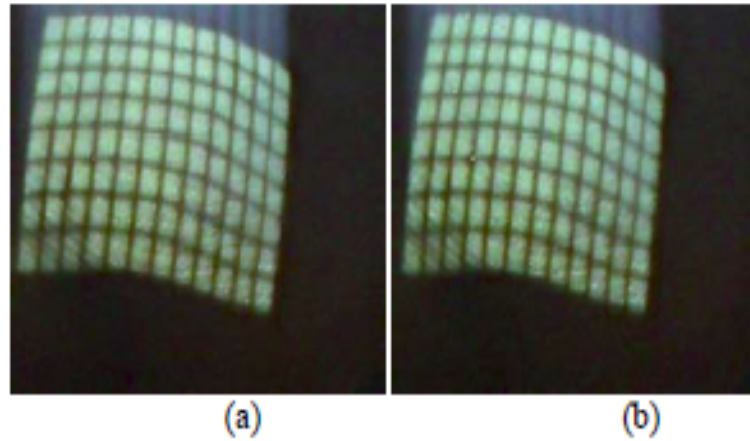


Figure 7.3: Input images of the stereo-endoscope:(a) An image from the left camera (b) An image from the right camera

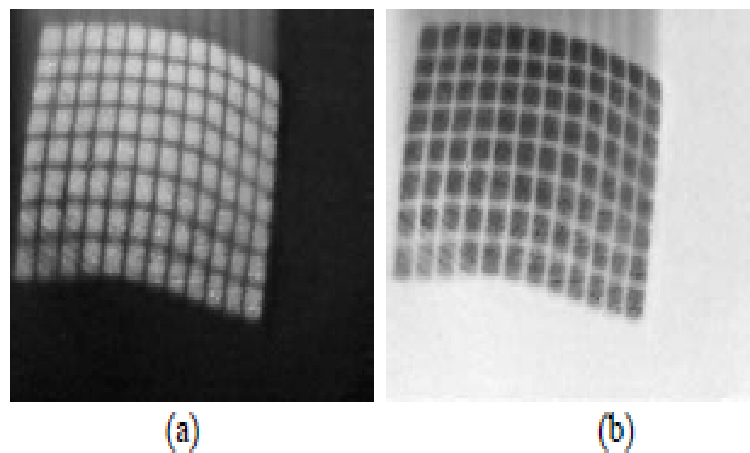


Figure 7.4: (a) A grayscale image (b) A negative image

### 7.2.2 Intensity Correction

Intensity refers to the amount of light each pixel has in an image [27]. For instance, in grayscale images, the intensity of the pixels ranges between 0 and 255. Where pixels with a value equal to 255 represents white color, pixels with an intensity value equal to zero are denoted with black color. The uniform distribution of pixels in an image helps to separate the background and the objects

of that image.

Due to the nature of endoscopy devices, the intensity of the acquired endoscopic images is not uniform, given that variation in illumination and ambient lights exist. As a consequence, conventional threshold methods cannot be directly used to achieve proper binary images which can successfully separate gridlines from the background. In this research, we present a new method to correct the intensity of the image. The aim of this intensity correction process is to improve the image quality leading to more accurate results. The improvement aims to equalize the contrast between gridlines and background over the whole image. The new corrected pixel value is calculated by:

$$I_{new} = 255 - ((I_{ave} - I_c)/2 + 127) \quad (7.1)$$

where  $I_c$  is the intensity value of the current pixel,  $I_{ave}$  is the average intensity of its neighbourhood pixels, and  $I_{new}$  is the new intensity value after correction. Figure 7.5 shows the center pixel in a neighbourhood of 3 x 3.

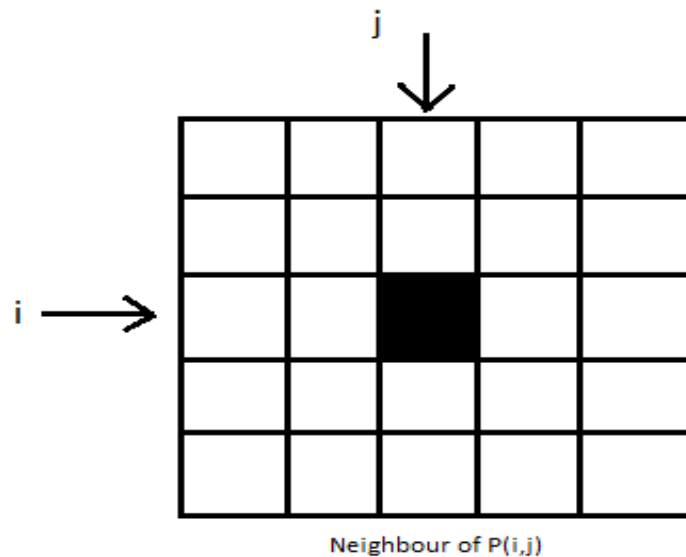


Figure 7.5: A center pixel within a neighbourhood

Figure 7.6 shows the image after intensity correction, in which the contrast between the gridlines and background is more uniform compared with the image before correction in Figure 7.4(b). Figure 7.7 shows binary images by thresholding, which will be used for intersection detection. With intensity correction, all gridlines are clearly shown in the binary image while without intensity correction, only part of the gridlines are shown in the cluttered binary image. The intensity correction also significantly improves the detection and matching accuracy with the success rate of 98% versus 57% without intensity correction (see Tables 7.9 and 7.10 ).

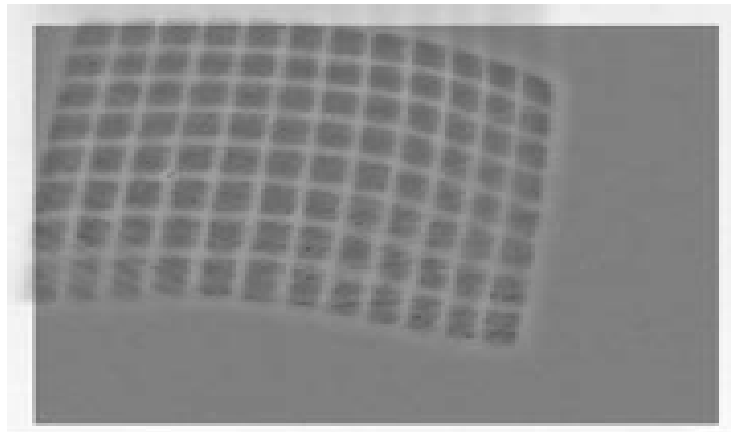


Figure 7.6: An intensity correction image

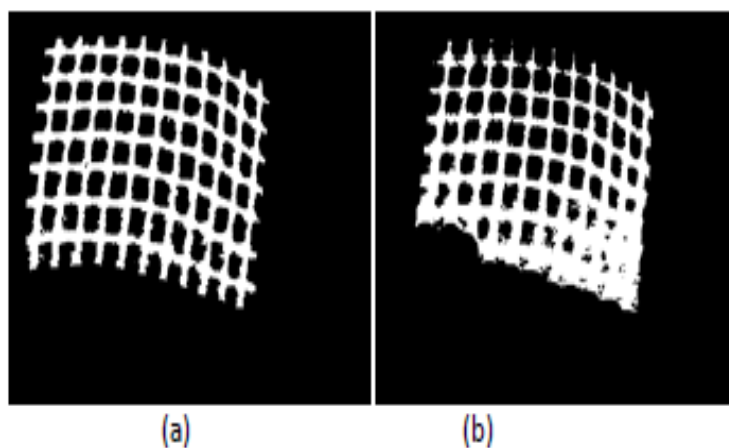


Figure 7.7: Binary image by thresholding (a) with intensity correction, (b) without intensity correction

### 7.2.3 Detection of Region of Interest

In this thesis, region of interest (ROI) is defined as the region which only covers the projected gridline light pattern in the endoscopic image. Automatic detection of ROI is critical for accurate detection and matching of intersection points in the gridline pattern. During the image preprocessing step, the area out of ROI should be cut out. ROI detection leads to automatic removal of unwanted areas. This step significantly improves the correctness of gridline intersection detection as well as the processing speed.

The ROI detection process aims to generate a mask of the grid lines pattern. Following intensity correction, we threshold the images in order to convert the corrected grayscale image into a binary image for further processing. Next, the dilation and the erosion operations are performed eventually, as the consequence of dilation and erosion processes, we obtain a binary mask image only covering the region of the projected gridline pattern. Then, we apply the mask image to the intensity corrected image to produce a cropped image within the desired ROI. The cropped image is then converted to a binary image by applying a threshold to it, which is used for feature detection. Figure 7.8(a) shows the detected ROI of the input image (ROI mask image), Figure 7.8(b) shows the cropped image within ROI.

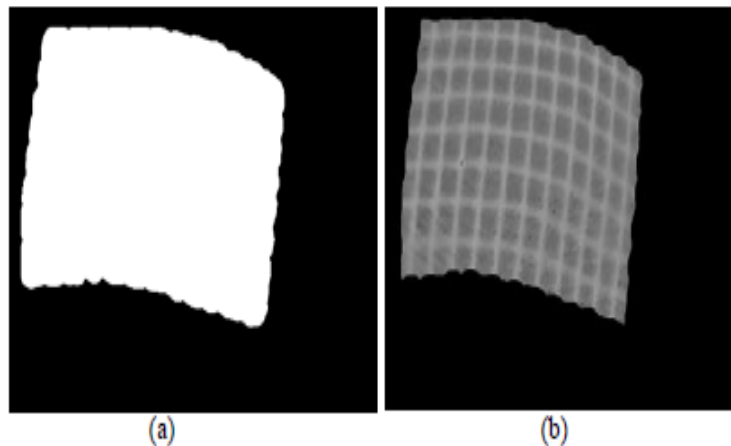


Figure 7.8: (a) Detected ROI mask image (b) Intensity correction image within ROI mask

## 7.2.4 Image Dilation and Erosion

Because of the conversion to a binary image, some white pixels in the binary image are far away from the gridlines. Hence, these types of pixels could cause false positive pixels in the thinning process. By using dilation, we can expand the gridlines to fill the gaps between them and the protrusions pixels. Dilation process followed by erosion process is used to return the structure to its original state by removing the added structure of the gridlines. As a result, we have smooth gridlines free of holes and protrusion pixels. Figure 7.9 shows the binary images before and after dilation and erosion process respectively.

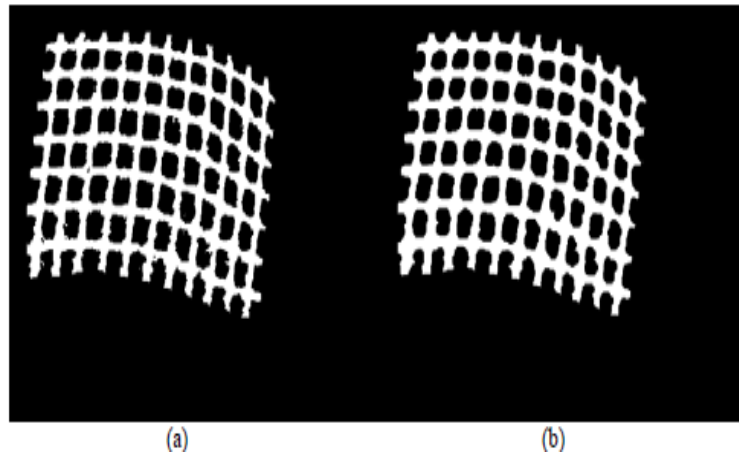


Figure 7.9: (a) The binary image before dilation (b) The same image after dilation process

## 7.2.5 Thinning and Intersection Detection

In order to detect the intersections of the gridline pattern we used a thinning process applied to the above processed binary image. The thinning process generates an image with one pixel width, i.e., it generates a skeleton image of the input binary image. Then we proceeded to detect the intersections of the image gridlines. This process accomplished by applying a hybrid approach for cross points detection called the Combined Cross-point Number (CCN) method [83]. The CCN method uses two techniques to detect intersections of gridlines: Simple Cross-point Number (SCN) and Modified Cross-point Number (MCN)

(MCN). The CCN algorithm is used to detect the intersection points of the gridlines. In simple cross-point number, the image is iterated with a small window of size 3 by 3 pixels [83], as a result we have eight pixels surrounding the tested pixel. To test if the center pixel of the 3 by 3 window is a cross-point pixel, we iterate this window on the image and get the cross point number (CPN) for the center pixel. The CPN is calculated by:

$$cpn_{scn} = 1/2 \sum_{i=1}^8 |P_n - P_{n+1}| \quad (7.2)$$

where  $cpn_{scn}$  is the pixel value of  $n$ th pixel of the 3 by 3 window, and ( $P_8 = P_1$ ). A point is considered a cross-point if its CPN is four. In modified cross-point number method, the image is iterated by a window of size 5 by 5 pixels surrounding the center pixel. The CPN is calculated by:

$$cpn_{mcn} = 1/2 \sum_{i=1}^{16} |P_n - P_{n+1}| \quad (7.3)$$

where ( $P_{17} = P_1$ ). The pixel is considered a cross point pixel if  $cpn_{mcn} \geq 4$ . In the combined cross-point number both simple cross-point number and modified cross point number methods are used. The simple cross point number is used in the inner 3x3 neighbors of the center pixel, while the modified cross point number is used in the outer 5x5 neighbors of the center pixel. Each pixel in the image has been tested against CPN using the modified cross point number method, in which it is considered a cross point if and only if it satisfies  $cpn_{scn} \geq 4$  and  $cpn_{mcn} \geq 4$ . Because of the low quality of the images we adjust the CPN of the combined CPN to be in the range of 3.0 and 4.0. Figure 7.10(a) shows the left skeleton image by thinning operation. Figure 7.10(b) shows the detected intersection points plotted on the left image. Figure 7.10(c) shows the detected intersection points and plotted on the right image. Notice that there are false positive points in both images, and as shown in Figure 7.11, these false points are eliminated by our method using the epipolar geometry matching con-

straint.

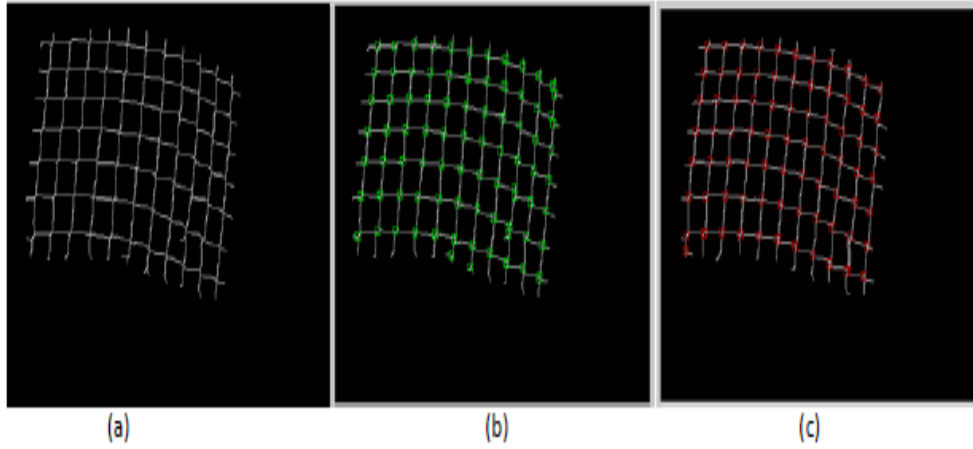


Figure 7.10: (a) An skeleton left image after thinning, (b) detected intersection points plotted on a left image, (c) detected intersection points plotted on a right image

### 7.2.6 Matching Grid Points

The main goal of this research is to construct a three-dimensional(3D) description of a scene from multiple two-dimensional images observed in the same scene. These 3D description will later be used to reconstruct the surface of the liver. Triangulation technique is the process of calculating the 3D points in the image, given the matching or the correspondence between the 2D points and the geometry of the stereo setting. In order to reconstruct the surface within the ROI using the triangulation technique, we need to find the corresponding intersection points in the left and right images. Since these grid points have similar features, these correspondence relationships cannot be effectively obtained using conventional feature matching methods such as Scale Invariant Feature Transform (SIFT) and Speeded Up Robust Features (SURF) based techniques. In this research, we adopt the method of epipolar constraint [60]. In epipolar constraint, a line  $U_1$  passes from the left image, points from the right image corresponding to that line must lie on the epipolar line (Figure 7.12). The epipolar line is the projection on the right image of 3D line going through the

left camera center and  $U_1$ .

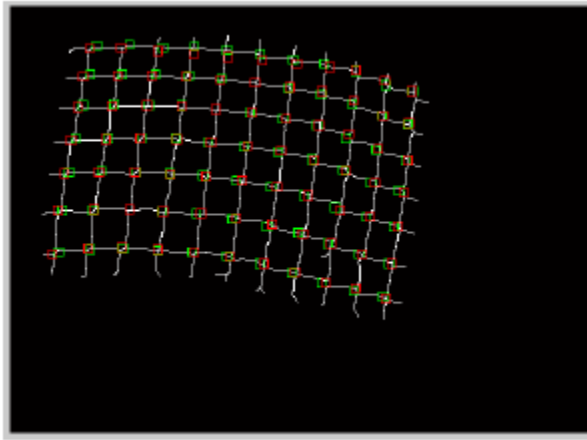


Figure 7.11: The correspondence points between the left and right images

In the proposed research, the intersection points are matched column-by-column from the left image to the right image to achieve good matching.

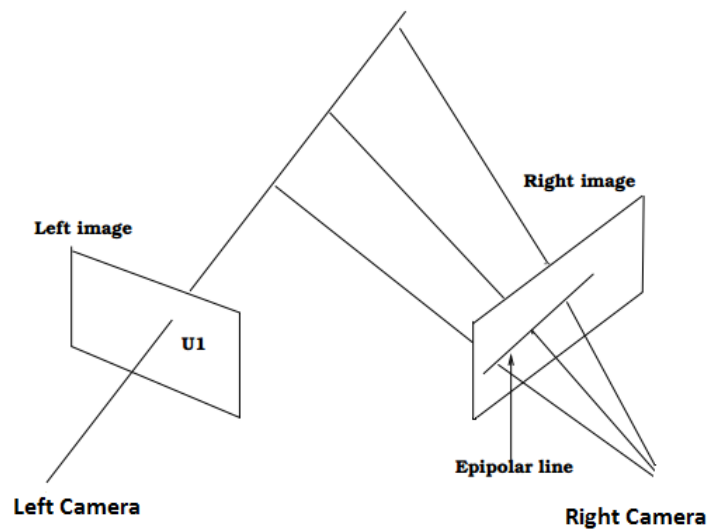


Figure 7.12: Epipolar constraints

We have validated the proposed approach using 19 pairs of images acquired at different position and orientation of the stereo endoscope. Figure 7.11 shows the matched grid points superimposed in one image. Table 7.10 shows the actual number of points in each image, the number of the points detected, the

number of correct points, the number of false positive points (FPP), and the number of false negative points (FNP). The average of sensitivity detection of the proposed method is 0.9822.

Image	Points	Detected Points	Correct Points	Sensitivity	FPP	FNP
Im1	77	73	73	0.9481	0	4
Im2	77	74	74	0.961	0	3
Im3	77	74	74	0.961	0	3
Im4	77	73	73	0.9481	0	4
Im5	77	76	76	0.987	0	1
Im6	77	78	77	1.0	1	0
Im7	77	77	76	0.987	1	1
Im8	77	76	76	0.987	0	1
Im9	77	76	76	0.987	0	1
Im10	77	76	76	0.987	0	1
Im11	77	76	76	0.987	0	1
Im12	77	76	76	0.987	0	1
Im13	77	77	77	1.0	0	0
Im14	77	76	76	0.987	0	1
Im15	77	77	77	1.0	0	0
Im16	77	76	76	0.987	0	1
Im17	77	76	76	0.987	0	1
Im18	77	76	76	0.987	0	1
Im19	77	76	76	0.987	0	1
Average				0.9822		

Table 7.9: Shows the actual number of points in each image, the number of the points detected, the number of correct points, the number of false positive points (FPP), and the number of false negative points (FNP).(with intensity correction)

## 7.2.7 Surface Reconstruction

In general, a video image generated from the endoscope is a 2D projection of the 3D scene. This process can be represented using the pinhole camera model [16]. To obtain the depth information from these 2D projected images, we need to calibrate the endoscopy cameras to get the calibration parameters. Camera calibration is a crucial step to extract the depth metric information from 2D images. The calibration process consists of extrinsic parameters to find the camera location and its ordination in the world, and intrinsic parameters that

Image	Points	Detected Points	Correct Points	Sensitivity	FPP	FNP
Im1	77	51	51	0.66	0	26
Im2	77	48	48	0.62	0	29
Im3	77	25	24	0.31	1	53
Im4	77	53	52	0.67	1	25
Im5	77	53	53	0.68	0	24
Im6	77	39	38	0.49	1	39
Im7	77	42	42	0.54	0	35
Im8	77	39	39	0.50	0	38
Im9	77	60	60	0.77	0	17
Im10	77	56	55	0.71	1	22
Im11	77	53	53	0.68	0	24
Im12	77	52	52	0.67	0	25
Im13	77	44	44	0.57	0	33
Im14	77	42	41	0.53	1	36
Im15	77	42	40	0.51	2	37
Im16	77	41	40	0.51	1	37
Im17	77	36	35	0.45	1	42
Im18	77	36	35	0.45	1	42
Im19	77	41	33	0.42	2	44
Average				0.5653		

Table 7.10: Shows the actual number of points in each image, the number of the points detected, the number of correct points, the number of false positive points (FPP), and the number of false negative points (FNP).(without intensity correction)

specify the relation between the pixel coordinates and the camera coordinates. After we obtain the camera calibration parameters, we reconstruct a 3D point  $x$  from left and right image projections by using stereo triangulation. A smooth surface can be reconstructed by fitting these reconstructed 3D grid points as shown in Figure 7.13. This figure demonstrates how the proposed method can achieve accurate surface reconstruction from the stereo endoscopic images.

In order to investigate the impact of the previous image processing procedures on the reconstructed surface, we have performed the following experiments. We use image intensity correction as an example to examine the effects in detail. We repeat the entire process of the surface reconstruction as shown in Figure 7.2, except that no intensity correction is performed. Figure 7.14 shows the reconstructed surface without intensity correction. In addition, Figure 7.17

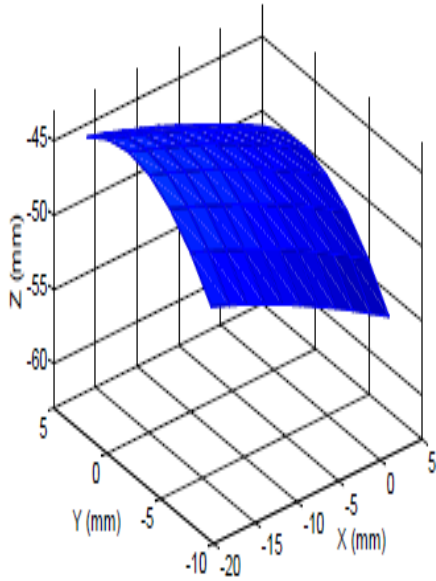


Figure 7.13: Reconstructed surface from stereo endoscopic images with intensity correction

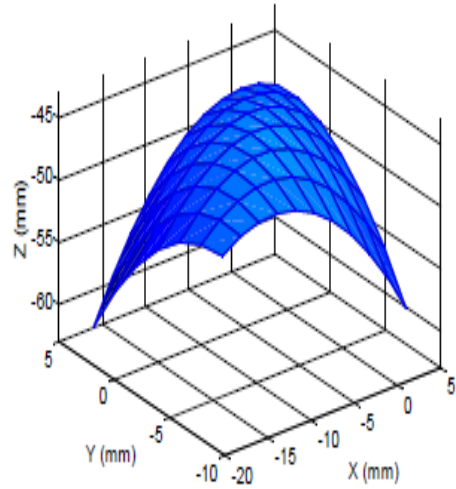


Figure 7.14: Reconstructed surface from stereo endoscopic images without intensity correction

shows the corresponding average registration error without intensity correction. The surface in Figure 7.17 has a convex shape which does not fit the surface correctly. Comparing Figures 7.13, 7.14, 7.16 and 7.17, we can clearly see the effect of intensity correction which has significantly improved the reconstruction accuracy. Applying intensity correction, the average surface reconstruction error reduces from 1.86 mm to 0.76 mm. Similarly, the proposed automatic detection method for ROI improve the reconstruction accuracy as well. In Table 7.11, we show how the average surface error are affected by previous image processing procedures.

Case	Mean(mm)	Standard Deviation (mm)
Proposed method	0.76	0.11
Without intensity correction	1.86	0.68
Without detection of ROI	1.24	0.73

Table 7.11: Average surface distance error (ASD) impacted by image processing procedures

## 7.3 Surface Based Registration

### 7.3.1 ICP Registration

The Iterative Closest Point (ICP) algorithm is widely employed to align two three-dimensional surfaces. The ICP algorithm proposed by Besl and McKay [66], which is an iterative two-step method. The first step is to establish point correspondences by finding the corresponding point closest to the second surface for each point in the first surface. The second step is to calculate the transformation (combination of translation and rotation) that iteratively modified to minimize the distance between the two registered surfaces or models. The transformation is based on these matched points, which produces incremental transformations whose composition is the registration results.

In this research, the ICP is employed to register the reconstructed surface from endoscopic images with the surface extracted from MR images. Figure 7.15 shows the overlay of 3D surfaces after surface registration.

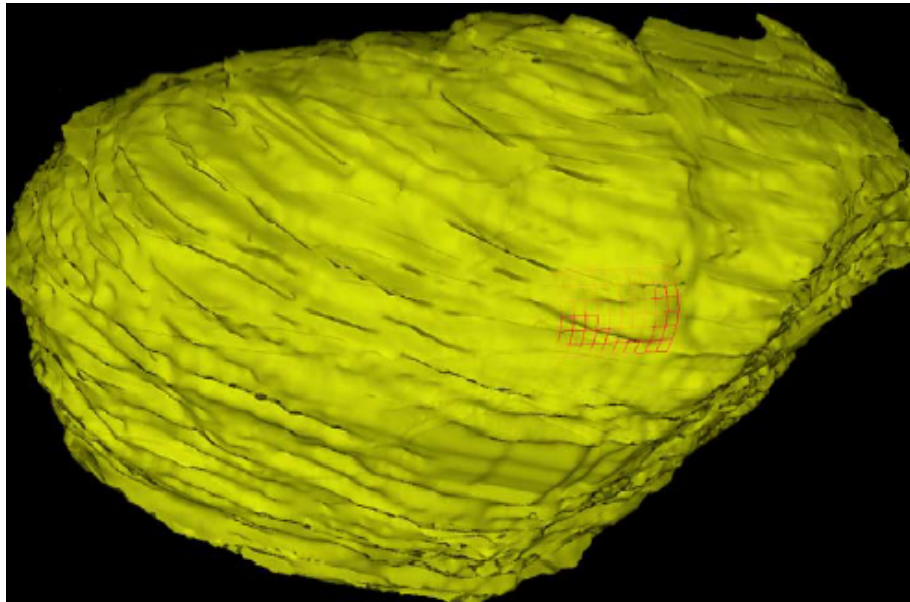


Figure 7.15: Overlay of 3D liver phantom surfaces after registration. Red mesh: reconstructed from endoscopic images, yellow surface: from MR images

### 7.3.2 Registration Accuracy

The projected gridline pattern used to test the proposed approach consists of seven rows and eleven columns, we have 77 intersection points to detect in each image. We used 19 pairs of left and right images acquired by the stereo endoscope at different poses for validation. After ICP surface registration, we calculated the average surface distance (ASD) between two corresponding surfaces as registration accuracy. The resulting ASD is  $0.76 \pm 0.11mm$  (see Figure 7.16). Figure 7.17 shows the corresponding registration accuracy without intensity correction.

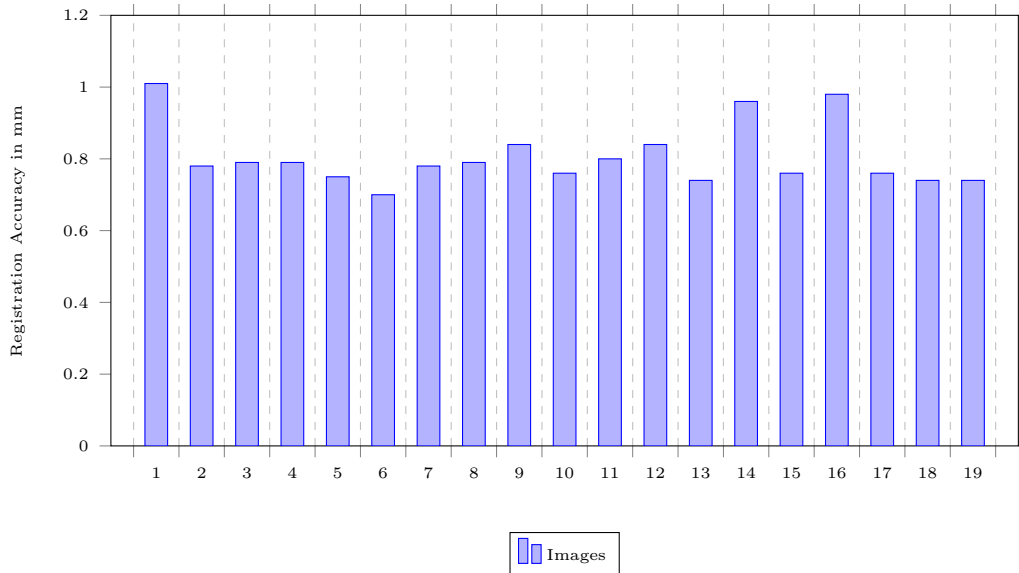


Figure 7.16: Surface registration accuracy using intensity correction

After surface based registration, we are able to fuse the reconstructed surface from stereo endoscopic images with pre-operative high quality MR images and the corresponding patient-specific models such as vessel centerlines as shown in Figure 7.19. This will enable surgeons to see through critical structures beyond the operational site surface.

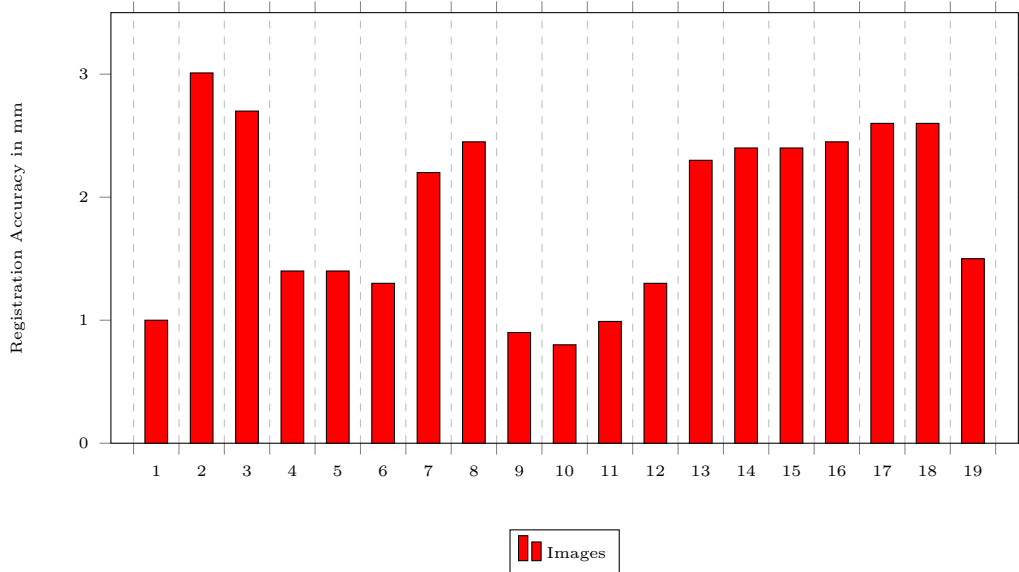


Figure 7.17: Surface registration accuracy without using intensity correction

## 7.4 Summary

In this research, we proposed a novel approach to match stereo endoscopic images and MR images. The proposed surface-based registration has proved to be an effective method for registering images of different imaging mechanisms. Moreover, the light patterns of the gridline facilitated the surface reconstruction of surgical sites with few surface features. In this research, we validated the proposed method with static objects, however, our method has the potential to be extended to procedures involving moving organs.

We have demonstrated the effectiveness of our technique in registration of the reconstructed surface with the surface extracted from MR images of a liver phantom. We have shown that various image processing techniques we used before the image registration have a significant impact on the resulting registration accuracy. We have achieved a surface registration accuracy of  $0.76 \pm 0.11mm$ . The proposed technique has the potential to be used in clinical practice to improve image guidance in endoscope based minimally invasive procedures. The fused image guidance may also be applied to the endoscopic procedures of other organs in the abdomen, chest cavity and pelvis such as the kidneys and the

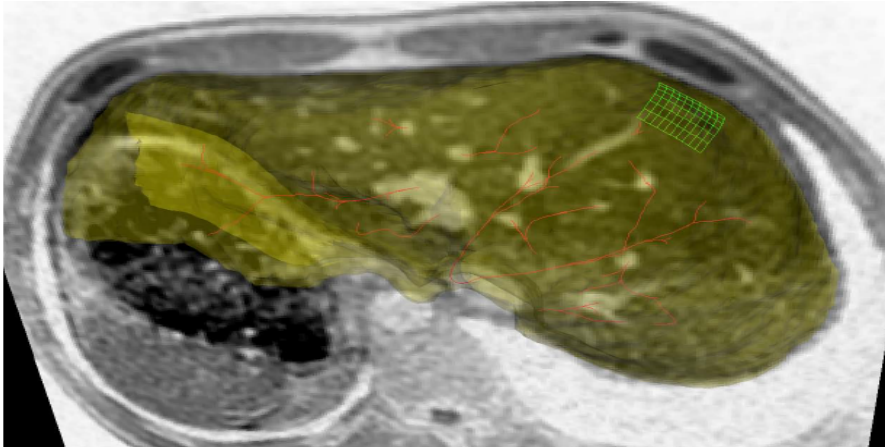


Figure 7.18: (a) Image fusion of patient models and reconstructed surface

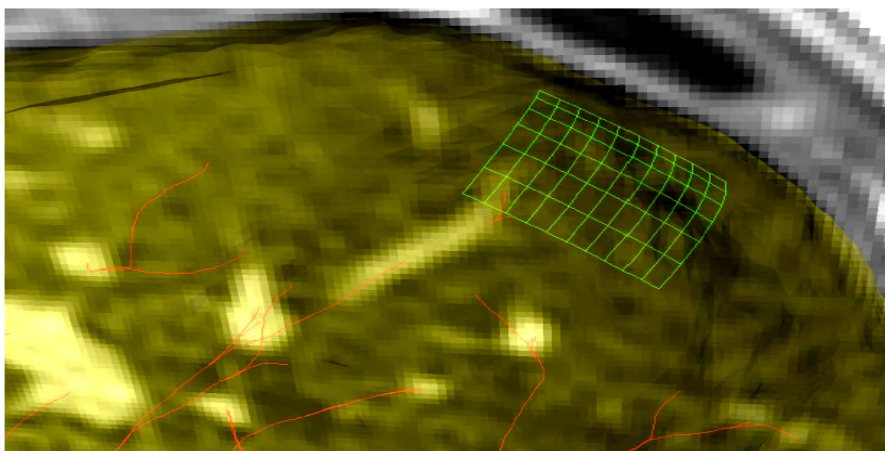


Figure 7.19: (b) Close-up around field of view of the endoscope

Figure 7.20: Fusion of patient models and reconstructed surface from the stereo endoscope. Green mesh is the reconstructed surface from two endoscopic images, red curves are the centerlines of vessels, segmented surface from MR images is shown in semi-transparent yellow, background is one MR slice with bright vessels

lungs.

Future work includes integration of our method into the clinical image guidance system and further validation by animal study and clinical study.

# Chapter 8

## Conclusion and Future Work

We have presented a coherent and consistent framework (Fig. 1.1) for image guidance procedure. In contrast with similar approaches in the literature, our methods presented in this thesis showed more robust and accurate results.

Three main topics were formulated in Chapter 1: image segmentation, deformable image registration, and registration of 3D surface reconstruction of stereo endoscopic images with MR images.

We performed preprocessing tasks on raw MR images to extract the blood vessels centerlines from these images. Next, bifurcation points were calculated as the intersections of the extracted centerlines. Vessel structures and bifurcation points provide input information for further operations such as image segmentation and image registration.

For image segmentation, we proposed an innovative approach to automating the initialization process of the liver segmentation of magnetic resonance images. The seed points, which are needed to initialize the segmentation process, are extracted and classified by using affine invariant moments and artificial neural network. Then, we proposed a new method to solve the leak problem in MR image segmentation using the level set technique.

For image registration, we proposed robust and fast approaches for MR image registration for deformable tissues. The proposed registration methods work

with soft homogenous and inhomogeneous tissue with small and large rotation and shift.

Lastly, we performed surface to surface registration of MR and endoscopic images. In this step, we project a gridline light pattern onto the surgical site and then use a stereo endoscope to acquire two stereo images. The major steps in the surface reconstruction process include 1) applying an automatic method of detecting region of interest, 2) applying an image intensity correction algorithm, and 3) applying a novel automatic method to match the intersection points of the gridline pattern.

Every step of the proposed framework has been tested and evaluated. Furthermore, the results and the methods presented in the thesis have been published or to be submitted in well-known conferences and publication sites. The aim of the proposed framework is to provide the surgeons as well as the physicians with a robust tool that can help in treatment and diagnoses procedures.

The proposed framework consists of image segmentation, image registration, and surface to surface registration. Those three topics form this thesis. Each method of these approaches has its challenges and contributions. Below, the challenges and the contributions will be formulated to each of the framework segments.

- **Segmentation of the Liver From Abdominal MR Image**

The review in chapter 3 showed that many researchers have attempted to obtain acceptable results for liver segmentation. The challenge of the segmentation process is due to the position of the liver in the abdominal. Since, the liver is surrounded by organs such as the heart, the stomach, and the kidneys. These organs have a similar intensity pattern as the liver that adds more challenges to the segmentation process. Also, the

quality of MR images acquired from different modalities affects by terms like motion artifacts, signal to noise ratio, low contrast and blurred edges.

A new solution is proposed to solve the leak problem in segmentation using the level set method of MR images for the same patient. The proposed method uses a second speed image acting as a surface blocker to prevent and pull back the propagation front when crossing the liver boundary. A prior knowledge about the liver has been used to generate the second speed image as well as to generate the surface patches to fill the segmented surface holes.

The proposed method has been validated by using Volumetric Overlap Error VOE with a golden set model. In VOE, the value is 1 for a perfect segmentation, and a value of 0 denotes to a completely failed one. The proposed method has VOE of 0.84.

- **Seeds Classification for Image Segmentation**

The region growing based image segmentation process starts by selecting seed points within the region of interest. Hence, the segmentation algorithm is sensitive to the initial seeds and the result can be influenced greatly by the accuracy of seed selection process. Manual seed selection can be time-consuming and requires an expert to complete the selection

In this thesis, we propose an innovative approach to automating the initialization process of the liver segmentation of magnetic resonance images. The seed points, which are needed to initialize the segmentation process proposed in this thesis, are extracted and classified by using affine invariant moments and artificial neural network.

We calculated eleven invariant moments for 56 different points within the region of interest. These points represent the bifurcation points of the vessels centerlines of the liver. In this thesis, we divide the shape of the liver into four regions; left hepatic vein, center hepatic vein, hepatic portal vein, and right hepatic vein. Then, the moments are classified by an artificial neural network to decide to which part of the liver each point belongs.

We have demonstrated the effectiveness of our technique using the classified seed points to segment liver from abdominal MR images. The proposed technique has an accuracy of 84.37% compared to manual seed point selection which has an accuracy of 80%. The results show that our method outperforms the manual method in terms of correct segmentation.

- **Vessel-Based Fast Deformable Registration with Minimal Strain Energy**

Image registration for internal organs and soft tissues is considered extremely challenging due to organ shifts and tissue deformation caused by patients movements such as respiration and repositioning.

In this thesis, we formulate the deformable image registration problem as a quadratic optimization problem that minimizes strain energy subject to the constraints of 3D curves of blood vessel centerlines and point marks. The proposed method does not require iteration and is local minimum free. By using 2nd order B-splines to model the blood vessels in the moving image and a new transformation model.

We have demonstrated the effectiveness of our deformable technique in

registering MR images of the liver. Validation results show that we can achieve a TRE of 1.29 *mm* and an average CDE of  $0.84 \pm 0.55$  *mm*.

- **Deformable Image Registration for Tissues with Large Displacement**

We increase the challenges to perform deformable registration of MR images of soft tissues with large motion.

In this thesis, we analyzed the deformation field of the liver by separating the deformation into rotation and pure deformation components, and concluded that in many clinical cases, the liver deformation contains large rotation and small deformation. This analysis justified the use of linear elastic theory/model in our image registration method. We also proposed a novel region-based neuro-fuzzy transformation model to seamlessly stitch together local affine models.

Validation results show that we can achieve a target registration error (TRE) of 2.31 mm and an average centerline distance error (ACD) of  $2.30 \pm 0.55$  mm.

- **Automatic Surface Reconstruction for Endoscopy-MR Image Fusion**

Minimally invasive endoscope based abdominal procedures provide potential advantages over conventional open surgery such as reduced trauma, shorter hospital stay, and quick recovery. One major limitation of using this technique is the narrow view of the endoscope and the lack of proper 3D context of the surgical site.

In this thesis, We project a gridline light pattern onto the surgical site and then use a stereo endoscope to acquire two stereo images. The major steps in the surface reconstruction process include 1) applying an automatic method of detecting region of interest, 2) applying an image intensity correction algorithm, and 3) applying a novel automatic method to match the intersection points of the gridline pattern.

We have validated our proposed technique on a liver phantom and compared our method with an existing method of similar scope. Our experiment results show that our method outperforms the existing method in terms of correct matching rate 98% which is an indicator of the surface reconstruction accuracy.

## 8.1 Future Research

The research presented in this dissertation provides a strong base for future research in image processing. The potential research topics that can build upon the research presented in this dissertation is addressed as follows:

- **Mapping Centerlines of Different MR Images:**

Blood vessels are often imaging targets in different imaging modalities such as magnetic resonance imaging (MRI), computed tomography (CT) and ultrasound as well. These vessel structures provide reliable references to localize treatment targets deep inside organs during treatment planning and treatment delivery, and robust features to anchor deformable tissues to align two images together in image registration. One of the preprocessing steps of the proposed image registration is to map the centerlines and the bifurcation points of two images manually. The average number of

segments of the liver centerlines is 110 segments. Hence, mapping these centerlines is considered time-consuming.

A possible future work in this part is to automate the mapping process of two MR images. This process can map centerlines from different images based on length and orientation. Also, we can eliminate unmatched, or merge centerlines.

- **Lungs Image Segmentation:**

For future work, we would like to extend the segmentation method proposed in this thesis to segment the lungs. In the proposed segmentation method, we used the vessels centerlines as prior knowledge to prevent the segmentation leak. In the same way, we can use the lungs airways in the region growing segmentation to do that task.

- **Points Classifications:**

The classification method we proposed in this thesis considers an excellent introduction to Neural Network and Machine Learning. The proposed method needs further improvement and enhancement by applying different techniques in Neural Network and Machine Learning. Possible future work could handle the issue of having more than one active pattern at the output, i.e.  $[0\ 0\ 1\ 1]$  or  $[0\ 1\ 0\ 1]$ . Another point for future work could be to minimize the number of middle layer neurons to improve the efficiency of the method.

# Appendices

# Appendix A

**Calculation of Curve Energy** The distance from the transformed point  $T(X_{fik})$  of the  $i^{th}$  fixed curve to the 3D moving curve  $C_{mi}(t)$  is calculated as follows:

$$\begin{aligned} E_{cmik}(p) &= \frac{1}{2} \|T(X_{fik}) - C_{mi}(t)\|^2 \\ &= \frac{1}{2} \left( X_{Tfik} - C_{mi}(t) \right)^T \left( X_{Tfik} - C_{mi}(t) \right), X_{Tfik} = T_{NF}(X_{fik}) \end{aligned} \quad (\text{A-1})$$

Substituting Eq. 5.4 into A-1, we rewrite the  $E_{cmik}$  as a fourth degree polynomial function of parameter  $t$ :

$$\begin{aligned} E_{cmik} &= (b_4 t^4 + b_3 t^3 + b_2 t^2 + b_1 t + b_0) \\ (b_4 + b_3 + b_2 + b_1 + b_0) &= f_{cik}(X_{Tfik}, C_{mijks}) \end{aligned} \quad (\text{A-2})$$

where  $(b_4 + b_3 + b_2 + b_1 + b_0)$  are constant coefficients given transformed point  $X_{Tfik}$  and moving curve  $C_{mi}(t)$ .

Given the parameters  $P_c$  of current transformation  $T(x)$  and discrete point  $X_{fik}$  on the fixed centerline, we first compute the transformed point  $X_{Tfik} = T(X_{fik})$ . Next, we find the corresponding closest point  $X_{cmik} = C_{mi}(t_{cmik})$  on vessel curve  $C_{mi}(t)$  such that the corresponding optimal parameter  $t_{cmik}$ ,

$$t_{cmik} = \text{arc min } E_{cmik} = \frac{1}{2} \|X_{Tfik} - C_{mi}\|^2 \quad (\text{A-3})$$

To minimize the distance  $E_{cmik}$  in A-2, we need to solve  $\frac{dE_{cmik}}{dt} = 0$ , i.e.

$$\begin{aligned}
f_d(X_{Tfik}, t) &= \frac{dE_{cik}}{dt} = 4b_4t^3 + 3b_3t^2 + 2b_2t + b_1 \\
&= a_3t^3 + a_2t^2 + a_1t + a_0 = 0
\end{aligned} \tag{A-4}$$

The optimal solution  $t_{cmik}$  is obtained by analytically solving the above cubic polynomial equation given  $X_{Tfik}$ .

As we know, there exists an analytical formula to calculate the roots of cubic polynomials. Note that if we choose a parametric representation of 3D curves with a cubic B-Spline, we need to solve a 5 – *th* degree polynomial equation  $\frac{dE_{cik}}{dt} = 0$ . Unfortunately, no analytical solution exists in this case. This is the reason why we select the 2<sup>nd</sup>-order of B-Spline to represent vessel centerlines so that we achieve good balance between smoothness and computational efficiency.

Because the optimal parameter corresponding to the shortest distance is a function of  $t_{cmik}$ , we apply the partial derivative operation with respect to  $X_{Tfik}$  on equation  $f_d(X_{Tfik}, t)$ ,

$$\frac{df_d(X_{Tfik}, t)}{dX_{Tfikj}} = \frac{\partial f_d}{\partial X_{Tfikj}} + \frac{\partial f_d}{\partial t} \cdot \frac{\partial t}{\partial X_{Tfikj}} = 0, \quad j = 1, 2, 3 \tag{A-5}$$

The corresponding partial derivatives of  $t$  with respect to the transformed discrete point  $X_{Tfik}$  are calculated as follows:

$$\left. \frac{\partial t}{\partial X_{Tfikj}} \right|_{t=t_{cmik}} = \frac{\partial t_{cmik}}{\partial X_{Tfikj}} = -\frac{\partial f_d}{\partial X_{Tfik}} \bigg/ \frac{\partial f_d}{\partial t}, \quad j = 1, 2, 3 \tag{A-6}$$

From A-4, we have

$$\frac{\partial f_d}{\partial t} = 3a_3t^2 + 2a_2t + a_1. \tag{A-7}$$

From A-1, we have

$$f_d(X_{Tfik}, t) \equiv \frac{\partial E_{cmik}}{\partial t} = -\left( \frac{\partial C_{mi}(t)}{\partial t} \right)^T \left( X_{Tfik} - C_{mi}(t) \right) \tag{A-8}$$

Therefore, we obtain

$$\frac{\partial f_d}{\partial X_{Tfik}} = -\frac{\partial C_{mi}(t)}{\partial t}, \quad j = 1, 2, 3 \quad (\text{A-9})$$

Now we derive an analytical formula to compute the derivative of  $E_{cik}$  with respect to transformation parameters  $p$ . From A-1, we have at the optimal parameter  $t_{cmik}$ ,

$$\begin{aligned} \frac{\partial E_{cik}}{\partial p} &= \left( \frac{\partial X_{Tfik}}{\partial p} - \frac{\partial X_{cmik}}{\partial p} \right)^T \left( X_{Tfik} - C_{mi}(t) \right) \\ &= \left( \frac{\partial X_{Tfik}}{\partial p} - \frac{\partial X_{cmik}}{\partial p} \right)^T \left( X_{Tfik} - X_{cmik}(t_{cmik}) \right) \end{aligned} \quad (\text{A-10})$$

Since  $t_{cmik}$  is a function of  $X_{Tfik}$  and  $X_{Tfik} = T(X_{fik})$ , we have

$$\frac{\partial X_{cmik}}{\partial p} = \frac{\partial C_{mi}(t)}{\partial p} = \left( \frac{\partial C_{mi}(t)}{\partial t} \right) \left( \frac{\partial t}{\partial X_{Tfik}} \right)^T \frac{\partial t}{\partial p} \quad (\text{A-11})$$

Combining A-10 and A-11, we have

$$\begin{aligned} \frac{\partial E_{cik}}{\partial p} &= \left( \frac{\partial X_{Tfik}}{\partial p} - \frac{\partial X_{cmik}}{\partial p} \right)^T \left( X_{Tfik} - X_{cmik}(t_{cmik}) \right) \\ &= \left( \frac{\partial T}{\partial p} - \left( \frac{\partial C_{mi}(t)}{\partial t} \right) \left( \frac{\partial t}{\partial X_{Tfik}} \right)^T \frac{\partial T}{\partial p} \right)^T \left( X_{Tfik} - X_{cmik}(t_{cmik}) \right) \\ &= \left( \frac{\partial T}{\partial p} \right)^T \left( I_{3 \times 3} - \left( \frac{\partial t}{\partial X_{Tfik}} \right) \left( \frac{\partial C_{mi}(t)}{\partial t} \right)^T \right) \left( X_{Tfik} - X_{cmik}(t_{cmik}) \right) \end{aligned} \quad (\text{A-12})$$

Using locally affine transformation model and denoting

$$D_{cmik}^T = I_{3 \times 3} - \left( \frac{\partial t}{\partial X_{Tfik}} \right) \left( \frac{\partial C_{mi}(t)}{\partial t} \right)^T$$

we have

$$\begin{aligned} \frac{\partial E_{cik}}{\partial p} &= \left\{ A_p(X_{fik}) D_{cmik}^T A_p^T(X_{fik}) p \right\} \\ &+ \left\{ A_p(X_{fik}) D_{cmik}^T (B_p(X_{fik}) - X_{cmik}) \right\} \end{aligned} \quad (\text{A-13})$$

Now we derive an analytical formula to compute the derivative of  $E_c(p)$  with respect to transformation parameters  $p$ . From Eq. 5.5, we have

$$\begin{aligned} \frac{\partial E_c(p)}{\partial p} &= \sum_{i=1}^{N_c} \sum_{k=1}^{N_{ci}} \frac{\partial E_{cik}}{\partial p} \\ &= \sum_{i=1}^{N_c} \sum_{k=1}^{N_{ci}} \left\{ A_p(X_{Tfik}) \quad D_{cmik}^T \quad A_p^T \quad (X_{Tfik}) \right\} p \\ &+ \sum_{i=1}^{N_c} \sum_{k=1}^{N_{ci}} \left\{ A_p(X_{fik}) \quad D_{cmik}^T \quad (B_p(x) - X_{cmik}) \right\} \end{aligned} \quad (\text{A-14})$$

# Appendix B

**Computation of Strain Energy** In this section, we derive the formula to calculate strain energy density  $W(E)$ . First we rewrite the following strain energy equation as follows:

$$E_e = \int \int \int W(E) dx dy dz$$

where

$$\begin{aligned} W(E) &= 0.5\lambda[tr(E)]^2 + \mu.tr(E^2), \\ tr(E) &= e_{11} + e_{22} + e_{33}, \\ W(E) &= \frac{\lambda}{2}(e_{11} + e_{22} + e_{33})^2 + \mu(e_{11}^2 + e_{22}^2 + e_{33}^2 + 2e_{12}^2 + 2e_{13}^2 + e_{23}^2) \quad \text{(B-1)} \\ e_{ij} &\approx \frac{1}{2} \left[ \frac{\partial T_{NFAi}}{\partial x_j} + \frac{\partial T_{NFAj}}{\partial x_i} - 2\delta_{ij} \right] \end{aligned}$$

In order to compute the element  $e_{ij}$  of the strain tensor  $E$ , we need to compute the derivative of transformation  $\frac{\partial T_{NFi}}{\partial x_j}$ .

We recall that, the overall neuro-fuzzy transformation model:

$$T_{NF}(x) = \sum_{r=1}^{N_R} M_{nr}(x) T_r(x) \quad \text{(B-2)}$$

The partial derivative of  $k^{th}$  component of  $T_{NF}(x)$  with respect to the  $i^{th}$  coordinate of point  $x$  is:

$$\frac{\partial T_{NFk}(x)}{\partial x_i} = \sum_{r=1}^{N_R} \left( \frac{\partial M_{nr}}{\partial x_i} T_{rk}(x) + M_{nr}(x) \frac{\partial T_{rk}(x)}{\partial x_i} \right) \quad \text{(B-3)}$$

Denoting  $D_{Mnri}(x) \equiv \frac{\partial M_{nr}}{\partial x_i}$ , we have

$$\frac{\partial T_{NFk}(x)}{\partial x_i} = \sum_{r=1}^{N_R} \left( D_{Mnri}(x) T_{rk}(x) + M_{nr}(x) a_{rki} \right) \quad (\text{B-4})$$

$$\frac{\partial T_{NFj}(x)}{\partial x_i} + \frac{\partial T_{NFi}(x)}{\partial x_j} = \sum_{r=1}^{N_R} \left( D_{Mnri}(x) T_{rk}(x) + M_{nr}(x) a_{rki} \right) \quad (\text{B-5})$$

$$\frac{\partial T_{NFj}(x)}{\partial x_i} + \frac{\partial T_{NFi}(x)}{\partial x_j} = \sum_{r=1}^{N_R} \left\{ \begin{array}{l} D_{Mnri}(x) T_{rj}(x) + M_{nr}(x) a_{rji} \\ + D_{Mnrj}(x) T_{ri}(x) + M_{nr}(x) a_{rij} \end{array} \right\}$$

Since  $T_{rk}(x)$  is a linear function with respect to transformation parameters  $p$ , we write the above equation in the following form:

$$\frac{\partial T_{NFj}(x)}{\partial x_i} + \frac{\partial T_{NFi}(x)}{\partial x_j} = A_{eij}(x)p + b_{eij} \equiv f_{eij} \quad (\text{B-6})$$

Therefore, we have

$$e_{ij} = \frac{1}{2} \left( f_{eij} - 2\delta_{ij} \right) \quad (\text{B-7})$$

Substituting B-7 to B-1, we obtain

$$W(E) = \left( 3\mu + \frac{9\lambda}{2} \right) - (2\mu + 3\lambda) \sum_{i=1}^3 f_{eii} + \left( \mu + \frac{\lambda}{2} \right) \sum_{i=1}^3 (f_{eii})^2 \quad (\text{B-8})$$

$$+ \frac{\lambda}{2} \left\{ (f_{e12})^2 + (f_{e13})^2 + (f_{e23})^2 \right\} \quad (\text{B-9})$$

$$+ \lambda \left\{ f_{e11} f_{e22} + f_{e11} f_{e33} + f_{e22} f_{e33} \right\} \quad (\text{B-10})$$

Note that  $f_{eij}$  is linear with respect to  $p$  from B-6,  $W(E)$  is a quadratic function of  $p$  and can be rewrite as follows:

$$\begin{aligned}
W(E) &= C_0 + \sum_{i=1}^{N_p} C_i p_i + \sum_{i=1}^{N_p} C_{ii} p_i^2 + \sum_{i=1}^{N_p} \sum_{j=i+1}^{N_p} C_{ij} p_i p_j \\
&= C_0(x) + C_1^T(x) p + p^T C_2(x) p
\end{aligned}$$

# List of my Publications

- [1] Abdalbari A., Ren J., and Green M. Seeds classification for image segmentation based on 3-D affine moment invariants. *Biomedical Engineering Letters/Under review*, 2016.
- [2] Huang X., Ren J., Abdalbari A., and Green A. Vessel-based fast deformable registration with minimal strain energy. *Biomedical Engineering Letters*, 6(1):47–55, 2016.
- [3] Abdalbari A. and Ren J. Accurate seed points classification using invariant moments and neural network. *Canadian Conference on Electrical and Computer Engineering*, pages 597–602, 2015.
- [4] Abdalbari A., Huang X., and Ren J. Segmentation of the liver from abdominal mr images: a level-set approach. *Proc. SPIE 9413, Medical Imaging 2015: Image Processing*, 9413:94133L1–94133L6, 2015.
- [5] Abdalbari A., Huang X., and Ren J. Automatic surface reconstruction for endoscopy-mr image fusion in image guided procedures. *IEEE Canadian Conference Of Electrical And Computer Engineering*, 26:716–723, 2013.
- [6] Abdalbari A., Huang X., and Ren J. Endoscopy-mr image fusion for image guided procedures. *Journal of Biomedical Imaging*, 2013(472971):1–10, 2013.

- [7] Huang X., Abdalbari A., and Ren J. 3D surface reconstruction of stereo endoscopic images for minimally invasive surgery. *Biomedical Engineering Letters*, 3(3):149–157, 2013.
- [8] Huang X., Abdalbari A., Zaheer S., Looi T., Ren J., and Drake J. Fast deformable Registration for Soft Organs with Large Motion in HIFU Treatment. *SPIE Medical Imaging*, 8671:J1 – J7, 2013.
- [9] Huang X., Abdalbari A., Zaheer S., Looi T., Ren J., and Drake J. 3D curve constrained deformable registration using a neuro-fuzzy transformation model. *Conf Proc IEEE Eng Med Biol Soc*, pages 5294–5297, 2012.
- [10] Huang X., Zaheer S., Abdalbari A., Looi T., Ren J., and Drake J. Extraction of liver vessel centerlines under guidance of patient-specific models. *Conf. Proc. IEEE Eng. Med. Biol Soc*, 2012(23):47–50, 2012.

# Bibliography

- [1] Abdalbari A., Huang X., and Ren J. Segmentation of the liver from abdominal mr images: a level-set approach. *Proc. SPIE 9413, Medical Imaging 2015: Image Processing*, 9413(3):L1–L6, 2015.
- [2] Beck A. and Aurich V. Hepatuxa semiautomatic liver segmentation system. *In MICCAI 2007 Workshop: 3D Segmentation in the Clinic-A Grand Challenge*, pages 225–233, 2007.
- [3] Falcao A., Jayaram K., Udupa K., and Miyazawa F. An ultra-fast user-steered image segmentation paradigm: Live-wire-on-the-fly. *Medical Imaging, IEEE Transactions on*, 19(1):55–62, 2000.
- [4] Fedorov A., Beichel R., Kalpathy-Cramer J., Finet J., Fillion-Robin J.-C., Pujol S., Bauer C., Jennings D., Fennessy F., Sonka M., Buatti J., Aylward S.R., Miller J.V., Pieper S., and Kikinis R. 3D slicer as an image computing platform for the quantitative imaging network. *Magn Reson Imaging*, 30(9):23–41, 2012.
- [5] Groch A., Seitel A., Hempel S., Speidel S., Engelbrecht R., Penne J., Hller K., Rhl S., Yung K., Bodenstedt S., Pflaum F., Santos T., Mersmann S., Meinzer H., Hornegger J., and Maier-Hein L. 3D surface reconstruction for laparo-scopic computer-assisted interventions:comparison of state-of-the-art methods. *Medical Imaging: Visualization, Image-Guided Procedures, and Modeling, Proc. SPIE*, 13(7964):1–15, 2011.

- [6] Mamistvalov A. N-dimensional moment invariants and conceptual mathematical theory of recognition of n- dimensional data sets. *IEEE. Trans. Pattern Anal*, 20:819–831, 1998.
- [7] Sethian J. A. Level set methods and fast marching methods: evolving interfaces in computational geometry, fluid mechanics, computer vision, and materials science. *Cambridge university press*, 3, 1999.
- [8] Sotiras A., Davatzikos C., and Paragios N. Deformable medical image registration: a survey. *IEEE Trans Syst Man Cybern*, 32(7):1153–1190, 2013.
- [9] Dhawan A.P. *Medical Image Analysis*, volume 31. John Wiley & Sons, New Jersey, second edition, 2011.
- [10] Ridge B., Ugur E., and Ude A. Comparison of action-grounded and non-action-grounded 3-d shape features for object affordance classification. *Advanced Robotics (ICAR), 2015 International Conference on, Istanbul*, pages 635–641, 2015.
- [11] Zitova B. and Flusser J. Image registration methods: a survey. *Image Vis Comput*, 21(11):977–1000, 2003.
- [12] J.Y. Bouguet. Matlab camera calibration toolbox. *http : //www.bibsonomy.org/bibtex/29295ae3c54c0d07cec38002071ef034a/barabas*, 2010.
- [13] Juang C. and Chang C. Human body posture classification by a neural fuzzy network and home care system application. *IEEE Trans. On Systems, Man, And CyberneticsPart A: Systems And Humans*, 37(6):984–994, 2007.
- [14] Ryszard C. Image feature extraction techniques and their applications for cbir and biometrics systems. *International Journal of Biology and Biomedical Engineering*, 1(1):6–16, 2007.

- [15] Xu C. and Prince J. L. Gradient vector flow: a new external force for snakes. *In Computer Vision and Pattern Recognition, 1997. Proceedings., 1997 IEEE Computer Society Conference*, pages 66–71, 1997.
- [16] Dey D., Gobbi G., Slomka P., Surry K., and Peters T. Automatic fusion of freehand endoscopic brain images to three-dimensional surfaces: creating stereoscopic panoramas. *IEEE Transactions on Medical Imaging*, 21(1):23–30, 2002.
- [17] Hill D., Batchelor G., Holden M., and Hawkes J. Medical image registration. *Physics in medicine and biology*, 46(3):R1–45, 2001.
- [18] Selle D., Preim B., Schenk A., and Peitgen H. Analysis of vasculature for liver surgical planning. *IEEE Trans Med Imaging*, 21(11):1344–1357, 2002.
- [19] Osorio E., Hoogeman M., Romero A., Wielopolski P., Zolnay A., and Heijmen B. Accurate CTMR vessel-guided nonrigid registration of largely deformed livers. *Med Phys*, 39(5):2463–2477, 2012.
- [20] Bower A. F. Applied mechanics of solids. *CRC Press*, 2009.
- [21] Jolesz F. MRI-guided focused ultrasound surgery. *Annual review of medicine*, 60:417–430, 2009.
- [22] Bookstein FL. Principal warps: thin-plate splines and the decomposition of deformations. *IEEE T Pattern Anal Machine Intell*, 11(6):567–585, 1989.
- [23] Gobbi G., Comeau R., and Peters T. Ultrasound/mri overlay with image warping for neurosurgery. *Proc. MICCAI 2000*, pages 106–114, 2000.
- [24] Hu G. and Stockman G. 3-d surface solution using structured light and constraint propagation. *IEEE Transactions on Pattern Analysis and Machine Intelligence*, 11(4):390–402, 1989.

- [25] Kumar G. and Bhatia P. A detailed review of feature extraction in image processing systems. *In Advanced Computing & Communication Technologies (ACCT), 2014 Fourth International Conference*, 9415:5–12, 2014.
- [26] Golub H. Gene and L. Van F. Charles. Matrix computations. *Johns Hopkins University Press*, 2nd ed, 1989.
- [27] Rafael C. Gonzalez and Richard E. Woods. *Digital Image Processing*. Pearson Printice Hall, Upper Saddle River, New Jersey, USA, third edition, 2008.
- [28] Gunner and John A. Probability and random processes for electrical and computer engineers. *New York: Cambridge University Press.*, 2006.
- [29] Kawasaki H., Furukawa R. and Sagawa R., and Y Yagi. Dynamic scene shape reconstruction using a single structured light pattern. *In Computer Vision and Pattern Recognition*, pages 1–8, 2008.
- [30] LO C. H. 3-D moment forms: Their construction and application to object identification and positioning. *Pattern Analysis and Machine Intelligence, IEEE Transactions on*, 11(10):1053–1064, 1989.
- [31] William H. and Blahd Jr. Normal breathing rates for children. [http :  
//www.webmd.com/children/normal-breathing-rates-for-children](http://www.webmd.com/children/normal-breathing-rates-for-children), 2014.
- [32] Joseph P. Hornak. *The Basics of MRI*. Interactive Learning Software, New York, first edition, 2008.
- [33] Gheta I., Hfer S., Heizmann M., and Beyerer J. A novel region-based approach for the fusion of combined stereo and spectral series in: Image processing. *Machine Vision Applications III (Proceedings Volume) Proceedings of SPIE*, 7538:17–21, 2010.

- [34] Nyström I., Malmberg F., Vidholm E., and Bengtsson E. Segmentation and visualization of 3D medical images through haptic rendering. *Proceedings of the 10th International Conference on Pattern Recognition and Information Processing*, pages 43–48, 2009.
- [35] Reinertsen I., Descoteaux M., Siddiqi K., and Collins DL. Validation of vessel-based registration for correction of brain shift. *Medical image analysis*, 11(4):374–388, 2007.
- [36] Crespo J. and Aguiar P. Revisiting complex moments for 2D shape representation and image normalization. *IEEE Transactions on Image Processing*, 20(10):2896–2911, 2011.
- [37] Fitzpatrick J., West J., and Maurer C. Predicting error in rigid-body point-based registration. *IEEE Trans Med Imaging*, 17(5):694–702, 1998.
- [38] Flusser J., Boldys J., and Zitova B. Moment forms invariant to rotation and blur in arbitrary number of dimensions. *Pattern Analysis and Machine Intelligence, IEEE Transactions*, 25(2):234–245, 2003.
- [39] Jaintz J. and Viergever M. A survey of medical image registration. *Medical Imag Analysis*, 2(1):1–36, 1998.
- [40] Mangin J., Poupon F., Rivire D., Cachia A., Collins D. L., Evans A. C., and Rgis J. 3D moment invariant based morphometry. *In Medical Image Computing and Computer-Assisted Intervention-MICCAI*, pages 505–512, 2003.
- [41] Meinguet J. Multivariate interpolation at arbitrary points made simple. *Zeitschrift fr angewandte Mathematik und Physik ZAMP*, 30(2):292–304, 1979.
- [42] Snchez J., Martnez E., and Arquero A. Improving parameters selection of a seeded region growing method for multiband image segmentation. *Ieee Latin America Transactions*, 13(3):843–849, 2015.

- [43] Prince J.L. and Links J.M. *Medical Imaging Signals and Systems*. Pearson Printice Hall, Upper Saddle River, New Jersey, USA, third edition, 2006.
- [44] Hans J. Johnson, M. McCormick, L. Ibáñez, and The Insight Software Consortium. *The ITK Software Guide*. Kitware, Inc., third edition, 2013. *In press*.
- [45] Brock K. K. Imaging and image-guided radiation therapy in liver cancer. *In Seminars in radiation oncology*, 21(4):247–255, 2011.
- [46] Hu M. K. Visual pattern recognition by moment invariants. *IRE Trans. Inf. Theory*, 8(2):179–187, 1962.
- [47] Murphy K., van Ginneken B., Reinhardt J.M., Kabus S., Ding K., Deng X., Cao K., Du K., Paragios N., Navab N., Gorbunova V., Sporring J., de Bruijne M., Han X., Heinrich M.P., De Nigris D., Collins D.L., Arbel T., Peroni M., Li R., Sharp G.C., Schmidt-Richberg A., Ehrhardt J., Werner R., Smeets D., Loeckx D., Song G., Tustison N., Avants B., Gee J.C., Staring M., Klein S., Stoel B.C., Urschler M., Werlberger M., Vandemeulebroucke J., Rit S., Sarrut D., and Pluim J.P. Evaluation of registration methods on thoracic ct: the empire10 challenge. *IEEE Trans Med Imaging*, 30(11):1901–1920, 2011.
- [48] Antiga L., Piccinelli M., Botti L., Ene-Iordache B., Remuzzi A., and Steinman D. An image-based modeling framework for patient-specific computational hemodynamics. *Medical and Biological Engineering and Computing*, 46(11):1097–1112, 2008.
- [49] Clements L., Chapman W., Dawant B., Galloway R., and Miga M. Robust surface registration using salient anatomical features for image-guided liver surgery: Algorithm and validation. *Medical Physics*, 35(6):2528–2540, 2008.

- [50] Maier-Hein L., Schmidt M., Franz A., Santos D., Seite A., Jhne B., Fitzpatrick J., and Meinzer H. Accounting for anisotropic noise in fine registration of time-of-flight range data with high-resolution surface data. *In Medical Image Computing and Computer-Assisted Intervention MICCAI*, pages 251–258, 2010.
- [51] Jonna Lilly. Robotics in the operating room. [http : //www.progressiveengineer.com/PEWebBackissues2005](http://www.progressiveengineer.com/PEWebBackissues2005), 2016.
- [52] Baumhauer M., Feuerstein M., Meinzer H., and Rassweiler J. Navigation in endoscopic soft tissue surgery: perspectives and limitations. *J. Endourol.*, 22(4):751–766, 2008.
- [53] Davis M., Khotanzad A., Flamig D., and Harms S. A physics-based coordinate transformation for 3-d image matching. *IEEE T Med Imaging*, 16(3):317–328, 1997.
- [54] Feuerstein M., Mussack T., Heining S., and Navab N. Intraoperative laparoscope augmentation for port placement and resection planning in minimally invasive liver resection. *IEEE Transactions on Medical Imaging*, 27(3):355–369, 2008.
- [55] Hayashibe M., Suzuki N., and Nakamura Y. Laser-scan endoscope system for intraoperative geometry acquisition and surgical robot safety management. *Medical Image Analysis*, 10(4):509–519, 2006.
- [56] Hindennach M., Zidowitz S., Schenk A., Bourquain H., and Peitgen H. Computer assistance for fast extraction and analysis of intrahepatic vasculature from contrast-enhanced ct-volume data for preoperative planning in liver surgery. *International Congress and Exhibition: Computer Assisted Radiology and Surgery*, 2:451–452, 2007.
- [57] Holden M. A review of geometric transformations for nonrigid body registration. *IEEE Trans Med Imaging*, 27(1):111–28, 2008.

- [58] Jabarouti M. and Soltanian-Zadeh H. Automatic segmentation of brain structures using geometric moment invariants and artificial neural networks. *Information Processing in Medical Imaging*, pages 326–337, 2009.
- [59] Scheuering M. Fusion of medical video images and tomographic volumes. *PhD thesis, University Erlangen-Nuernberg, Germany*, 2003.
- [60] Sonka M., Hlavac V., and Boyle R. Image processing analysis and machine vision 3rd edn. *Nelson Engineering*, 2008.
- [61] VasquezOsorio M., Hoogeman M., MendezRomero A., Wielopolski P., Zolnay A., and Heijmen B.J. Accurate CTMR vessel-guided nonrigid registration of largely deformed livers. *Med. Phys. Medical Physics*, 39(5):63–77, 2012.
- [62] Benoudjit N., Ferroudji K., Bahaz M., and Bouakaz A. In vitro microemboli classification using neural network models and rf signals. *Ultrasonics*, 51(3):247–252, 2011.
- [63] Shusharina N. and Sharp G. Analytic regularization for landmark-based image registration. *Physics in medicine and biology*, 57(6):1477–1498, 2012.
- [64] Werghi N. and Xiao Y. Recognition of human body posture from a cloud of 3D points using wavelet transform coefficient. *n Automatic Face and Gesture Recognition, 2002. Proceedings. Fifth IEEE International Conference*, pages 70–75, 2002.
- [65] Commowick O., Arsigny V., Isambert A., Costa J., Dhermain F., Bidault F., Bondiau P.Y., Ayache N., and Malandain G. An efficient locally affine framework for the smooth registration of anatomical structures. *Medical Image analysis*, 12(4), 2008.
- [66] Besl P. and McKay N. A method for registration of 3-d shapes. *IEEE Trans. on Pattern Analysis and Machine Intelligence*, 14(2):239–254, 1992.

- [67] Campadelli P., Caseraghi E., and Esposito A. Liver segmentation from computed tomography scans: A survey and a new algorithm. *Artificial intelligence in medicine*, 45(2-3):185–196, 2009.
- [68] Pluim J. P., Maintz J. A., and Viergever M. A. Mutual-information based registration of medical images: a survey. *IEEE T Med Imaging*, 22(8):986–1004, 2003.
- [69] Ciarlet P.G. Mathematical elasticity. *North Holland*, 1, 1988.
- [70] M. Proesmans, L.J. van Gool, and A.J. Oosterlinck. Active acquisition of 3d shape for moving objects,” in proceedings of international conference on image processing. *Proceedings of International Conference on Image Processing*, 3:647–650, 1996.
- [71] Dass R. and Devi S. Image segmentation techniques. *International Journal of Electronics and Communication Technology*, 3(1):66–70, 2012.
- [72] Malladi R., Sethian J., and Vemuri B. Shape modeling with front propagation:a level set approach. *EEE Trans. Pattern Anal. Mach.Intell.*, 17(2):158174, 1995.
- [73] Smith-Bindman R., Miglioretti D. L., E. Johnson, Lee C., Feigelson H. S., Flynn M., and Solberg L. I. Use of diagnostic imaging studies and associated radiation exposure for patients enrolled in large integrated health care systems. *Jama*, 307(22):2400–2409, 2012.
- [74] Aylward S. Initialization, noise, singularities, and scale in height ridge traversal for tubular object centerline extraction. *IEEE Transactions on Medical Imaging*, 21(2):61–75, 2002.
- [75] Cerutti S., Baselli G., Bianchi A.M., Caiani E., Contini D., Cubeddu R., Dercole F., Di Rienzo L., Liberati D., Mainardi L., Ravazzani P., Rinaldi

- S., Signorini M.G., and Torricelli A. , biomedical signal and image processing. *IEEE Canadian Conference Of Electrical And Computer Engineering*, 2(3):41–54, 2011.
- [76] Pan S. and Dawant B. M. Automatic 3D segmentation of the liver from abdominal CT images: a level-set approach. *SPIE Medical Imaging*, page 128133, 2001.
- [77] Ryu S.J., Lee M. J., and Lee H. K. Detection of copy-rotate-move forgery using zernike moments. *In Information Hiding. Springer Berlin Heidelberg*, pages 51–65, 2010.
- [78] Heimann T., Ginneken B., Styner M. A., Arzhaeva Y., Aurich V., Bauer C., A. Beck, Becker C., Beichel R., Bekes G., Bello F., Binnig G., Bischof H., Bornik A., Cashman P. M. M., Chi Y., Cordova A., Dawant B. M., Fidrich M., Furst J. D., Furukawa D., Grenacher L., Hornegger J., Kainmuller D., Kitney R. I., Kobatake H., Lamecker H., Lange T., Lee J., Lennon B., Li R., Li S., Meinzer H. P., Nemeth G., Raicu D. S., A. M. Rau, Van Rikxoort E. M., Rousson M., L. Rusko, Saddi K. A., Schmidt G., Seghers D., Shimizu A., Slagmolen P., Sorantin E., Soza G., Susomboon R., Waite J. M., Wimmer A., and Wolf I. Comparison and evaluation of methods for liver segmentation from ct datasets. *IEEE Transactions on Medical Imaging*, 28(8):1251–1265, 2009.
- [79] Heimann T., Thorn M., Kunert T., and Meinzer P. New methods for leak detection and contour correction in seeded region growing segmentation. *In 20th ISPRS Congress, Istanbul, XXXV:317–322*, 2004.
- [80] Lange T., Papenberg N., Heldmann S., Modersitzki J., Fischer B., Lamecker H., and Schlag P. 3D ultrasound-ct registration of the liver using combined landmark-intensity information. *International journal of computer assisted radiology and surgery*, 4(1):79–88, 2009.

- [81] Lange T., Eulenstein S., Hunerbein M., and Schlag P. Vessel-based non-rigid registration of MR/CT and 3D ultrasound for navigation in liver surgery. *Computer Aided Surgery*, 8(5):228–240, 2003.
- [82] Songqiao T., Zhengdong H., Bingquan Z., Yangping P., and Weirui K. Partial retrieval of cad models based on the gradient flows in lie group. *Journal of Pattern Recognition*, 45(4):1721–1738, 2012.
- [83] Bevilacqua V., Cambo S., Cariello L., and Mastronardi G. A combined method to detect retinal fundus features. *In Proceedings of IEEE European Conference on Emergent Aspects in Clinical Data Analysis*, pages 1–6, 2005.
- [84] Barrett W. and Mortensen E. Fast, accurate and reproducible live-wire boundary extraction. *Visualization in Biomedical Computing*, 1131:183–192, 2006.
- [85] Pluim W., Maintz J., and Viergever M. Mutual information based registration of medical images: a survey. *Computer Vision, Graphics and Image Processing*, 22(8):986–1004, 2003.
- [86] Wikipedia. Endoscopy. 2014.
- [87] Huang X., Abdalbari A., , and Ren J. Fast deformable Registration for Soft Organs with Large Motion in HIFU Treatment. *SPIE Medical Imaging*, 8671:86711J–1 – 86711J–7, 2013.
- [88] Huang X, Abdalbari A., Zaheer S., Looi T., Ren J., and Drake J. 3D curve constrained deformable registration using a neuro-fuzzy transformation model. *Conf Proc IEEE Eng Med Biol Soc*, pages 5294–5297, 2012.
- [89] Huang X., Ho D., Ren J., and Capretz L. A soft computing framework for software effort estimation. *Soft Computing*, 10(2):170–177, 2006.

- [90] Huang X., Ren J., Abdalbari A., and Green M. Vessel-based fast deformable registration with minimal strain energy. *Biomedical Engineering Letters*, 6(1):47–55, 2016.
- [91] Huang X, Ren J, Guiraudon D, Boughner D, and Peters TM. Rapid dynamic image registration of the beating heart for diagnosis and surgical navigation. *IEEE T Med Imaging*, 28(11):1802–1814, 2009.
- [92] Huang X., Babyn PS., Looi T., and Kim P. A novel hybrid model for deformable image registration in abdominal procedures. *In SPIE Medical Imaging*, pages 79640K–79640K, 2011.
- [93] Maurice X., Albitar C., Doignon C., and Mathelin M. A structured light-based laparoscope with real-time organs’ surface reconstruction for minimally invasive surgery. *Annual International Conference of the IEEE Engineering in Medicine and Biology Society (EMBC)*, pages 5769–5772, 2012.
- [94] Derpanis K.G. Zhu M., Yang Y., Brahmabhatt S., Zhang M., Phillips C., Lecce M., and Daniilidis K. Single image 3D object detection and pose estimation for grasping. *IEEE International Conference on Robotics and Automation (ICRA)*, pages 3936–3943, 2014.